Development of a New Technique to Study the Kinetics of Hydroxyl Radical Uptake on Micron-Sized Organic Aerosols

by

Lucas Jonathan Neil

A thesis
presented to the University of Waterloo
in fulfillment of the
thesis requirement for the degree of
Doctor of Philosophy
in
Earth Sciences

Waterloo, Ontario, Canada, 2010

AUTHOR'S DECLARATION

I hereby declare that I am the sole author of this thesis. This is a true copy of the thesis, including any required final revisions, as accepted by my examiners.

I understand that my thesis may be made electronically available to the public.

Abstract

The importance of the hydroxyl radical (OH) to tropospheric chemistry is well known. The radicals' ability to react with most atmospheric trace gases allows it to act as the main removal mechanism for these gases. Due to the highly reactive nature of OH, the oxidizing capacity of the atmosphere is often defined simply by its concentration. Owing to its significant role, knowledge of all OH chemistry, homogeneous and heterogeneous, is important to understanding the chemistry of the troposphere. In order to accurately predict future levels of OH and other trace gases, a thorough understanding of all processes and variables involved in the emission and sequestering of these compounds is essential.

The gas-phase chemistry of OH is well known and has been extensively characterized. The one process that scientists are still trying to fully understand is its involvement in heterogeneous chemistry. Some studies have suggested that the inclusion of OH heterogeneous chemistry is important to fully model tropospheric chemistry, while other studies have suggested that it can be neglected entirely. It is therefore important to study and understand the conditions in which heterogeneous chemistry is significant. In order to do this accurately, scientists must first understand the process and magnitude of the uptake of OH onto atmospherically relevant surfaces.

The main objective of this work was the development of a new analytical tool for the study of heterogeneous hydroxyl radical reactions. To this end, experiments were conducted to determine the most efficient approach to couple a low pressure aerosol flow tube (LP-AFT) to a chemical ionisation mass spectrometer (CIMS). The use of CIMS allowed for the accurate detection and quantification of hydroxyl radicals. Through iterative experimentation the system was designed and became operational. Experimental work focused on laboratory studies of reaction kinetics, with data reported in this work representing the reactions of OH with model atmospheric aerosols.

The uptake of OH on organic aerosols was examined using the newly developed LP-AFT-CIMS system at standard temperature. Liquid oleic acid particles were used to mimic atmospherically relevant particles. The uptake coefficient, γ, on oleic acid particles was determined to be 0.49 ± 0.08 for a log-normally distributed aerosol at ~400nm. This value is in very good agreement with currently published data. However, the overall error of this method (~16%) is observed to be lower than other currently available methods, which have errors ranging from 20 – 30%. It is postulated that the mass accommodation coefficient, α, for OH radicals on organic surfaces approaches this

value under standard atmospheric conditions. It's also suggested that under the correct conditions the heterogeneous loss of OH could contribute to the overall budget of the OH radical. Further atmospheric implications of this reaction are discussed.

Acknowledgements

This thesis arose out of five years of hard work at the University of Waterloo. Throughout those five years the nature of this thesis has evolved due to my interaction and collaboration with a large number of people, many of whom I will try to thank in the next couple of pages. I would like to thank Dr. Sloan, firstly, for advising me on my fourth year research project as an undergrad. It was my experiences in his lab at that time that persuaded me to pursue graduate studies. Secondly, I would like to thank Dr. Sloan for providing me with the opportunity to work on this project, and for his continued support, insight, and advice. My experiences in his lab over the past eight years have helped to shape me as a scientist. His patience and encouragement over that time provided the backdrop for my progress and development, and for this I am forever appreciative. I would also like to thank the members of my Ph.D. committee – Dr. Hind Al-Abadleh, Dr. Thomas Edwards, and Dr. Shaun Frape – for all of their questions and comments, and for making committee meetings and seminars relaxed and surprisingly bearable. I would also like to thank Dr. Jeffery Brook for the time he dedicated while as a member of my thesis committee. In addition, I would like to acknowledge the Canadian Foundation for Climate and Atmospheric Sciences for their role in the funding of this project.

I would like to extend special thanks to Dr. Asan Bacak, who was my mentor and co-worker for the final three years of my research. His experience and expertise with mass spectrometry was of immeasurable help. He made it possible to even consider the possibility that I would obtain experimental results and, perhaps, one day graduate. Special thanks must also go to Dr. Thomas Kuhn for all of his help in the laboratory, and for numerous invaluable discussions. His work with CFD modeling of my system helped to define and shape the experimental system.

I am also grateful for the friendship and support of the members of the Sloan lab group, both past and present. Firstly, a very large and special “Thank You” goes to Joan Currie for all her work

with CFD simulations. Her work was invaluable to this thesis and its influence can be found throughout. Special mention must be given to Rodion Remorov, Alex Zasetsky, and our lab technician Alex Chornyy for their scientific expertise. A special thanks goes to all the graduate students I worked with during my five years at UW. This of course includes Michael Earle, Rocsana Pancescu, Hongyan Dang, Jerry Hu, and Zena Rebello. It's always helpful to have a sympathetic ear to which you can moan and complain. Of course none of my research would have been possible without the help of the staff of the Science Machine Shop. Thanks to Harmen Vander Heide for all his brainstorming sessions and his ability to not get mad at me every time I brought another "rush" job to him. Particular thanks to Mike Lang and Peter Kessel for their professional and speedy work, and to Hiruy Haile for all his help in the Student Machine Shop. Thanks to Jacek Szubra and the staff of the Electronics Group of Science Technical Services for all their hard work and help with the project.

My friends and family deserve a huge amount of credit for keeping me positive in the face of adversity and for making my time outside of the lab both fulfilling and entertaining. Thanks to my father for his willingness to lend an ear to any problem I was having at work and for proof-reading this thesis. Thanks to my mother for, well, being my mother. Thanks to my friends for helping me get through rough times and for reminding me that sometimes you just have to have some fun.

Lastly, I have to thank my wife, Mary, who put up with a total of seven years of graduate school. Through two years in Ann Arbor and five years in Waterloo, Mary has stood by me, encouraged me and put up with me. Without her patience, understanding and love I would not have made it this far. She is my love, she is my life, and she will always be my beautiful angel.

Dedication

Without the love and support of my wife and family, I would never have made it this far. This thesis is as much their accomplishment as it is mine. I could never thank you all enough, so I will simply say: Thank You.

Table of Contents

List of Figures

List of Tables

Chapter 1
Introduction

1.1 Evolution of the Atmosphere

Radioactive dating of meteorites and lunar samples provide ample evidence that the solar system is approximately 4.5 billion years old.[1] The evolution of the earth's atmosphere can be divided into four stages, which span this time period. Prior to 4.5 billion years ago the Earth was still hot. The Earth's gravitational field was weak and the initial atmosphere, consisting primarily of hydrogen and helium[2], was lost to space. Approximately 4.5 billion years ago, the out-gassing of volatile gases began to form a thin atmosphere, as a result of volcanic activity and meteorite impact. This atmosphere had a similar content to current volcanic eruptions, consisting of carbon dioxide (CO_2), water vapour (H_2O), sulphur dioxide (SO_2) and nitrogen gas (N_2). This CO_2-rich atmosphere, containing no free oxygen, was more dense and warmer than the current atmosphere, even though the solar irradiance was less than the modern day.[3]

Around 4 billion years ago, the Earth began to cool. This cooling facilitated the condensation of water, causing the formation of clouds, rain and eventually the oceans. This resulted in a reduction of atmospheric H_2O and CO_2 and a N_2-rich atmosphere. Between 3.5 – 2.5 billion years ago, an atmosphere similar in composition to that of the "modern day" atmosphere was formed. Existence of life forms lead to photosynthesis and the subsequent removal of CO_2 and the release of molecular oxygen (O_2). As a result, O_2 became the atmosphere's second most abundant gas. Consequently, the interaction of ultra violet (UV) light and oxygen molecules initiated the development of an ozone (O_3) layer that provided protection from UV radiation and allowed life to flourish.

1.2 Composition of the Earth's Atmosphere

The atmosphere we breathe is a relatively stable mixture of several hundred types of gases of different origins. This gaseous envelope that surrounds the planet is held to the surface of the planet by gravitational attraction. Compared to the diameter of the earth, the atmosphere can be likened to the skin on an apple. This relatively thin layer of gas is what allows life to exist on the surface of this planet.

The majority of atmospheric research focuses on the gaseous envelope that extends 30 km above the Earth's surface, where more than 99% of the mass of the atmosphere is found.[1] At altitudes above 80 km, the composition of the atmosphere varies with height. Below 80 km, the atmosphere is comprised mainly of N_2 (~78.08 %), O_2 (~20.95 %) and argon (Ar) (~0.93 %). The composition of these gases constitutes 99.96% of the atmospheric mass below 80 km. It is the presence of trace gases, however, that give the atmosphere its reactivity. Examples of these trace gases are water H_2O < 0.25%, CO_2 ~ 0.036% (360 ppmv), methane (CH_4) ~ 0.00015% (1.5 ppmv), and O_3 ~ 0.00001% (100 ppbv), where ppmv = parts per million by volume and ppbv = parts per billion by volume.

1.3 Tropospheric Hydroxyl Radical Chemistry

The key to understanding tropospheric chemistry lies in understanding the reactions of the hydroxyl radical (OH). Despite being one of the most reactive molecules in the atmosphere, OH is not reactive towards molecular oxygen. Consequently, OH survives to react with most atmospheric trace species. As a result, the key function of OH is to act as a removal mechanism for trace gases in the troposphere. Table 1.1 shows the estimated global emissions of some trace gases and the approximate percentage of each that is destroyed by reaction with OH.[4]

Table 1.1: Estimate of tropospheric emissions of trace gases and removal by OH.[4]

Trace Gas	Global Emission Rate (Tg/yr)	Removal by OH (%)	Removal by OH (Tg/yr)
CO	2800	85	2380
CH_4	530	90	477
C_2H_6	20	90	18
Isoprene	570	90	513
Terpenes	140	50	70
NO_2	150	50	75
SO_2	300	30	90
$(CH_3)_2S$	30	90	27

The oxidative capacity of the atmosphere is typically defined as the concentrations of O_3 and OH. However, due to the highly reactive nature of OH, it is sometimes simply defined as the concentration of OH. Without an efficient oxidation process, levels of many emitted gases could rise to such high levels that they would radically change the chemical nature of the atmosphere and biosphere. A change in the chemical composition of the atmosphere would also have a drastic impact on climate through the greenhouse effect. Due to its significant role, knowledge of all OH chemistry, homogeneous and heterogeneous, is important to understanding the chemistry of the troposphere.

1.3.1 Daytime Photochemistry

In the sunlit background troposphere, radical production is primarily driven by the short-wavelength photolysis of ozone, and reaction of the electronically excited oxygen atom, $O(^1D)$, with water vapour:

$$O_3 + h\nu \rightarrow O(^1D) + O_2 \qquad \text{R1.1}$$

$$O(^1D) + H_2O \rightarrow OH\cdot + OH\cdot \qquad \text{R1.2}$$

As much as 10% of the $O(^1D)$ produced via R1.1 reacts with H_2O to generate OH.[1;5] Since two molecules of OH are produced in R1.2, at room temperature and a relative humidity (RH) of 50%, an overall yield of 0.2 molecules of OH is produced per O_3 molecule photolyzed.[5]

OH subsequently reacts (primarily) with hydrocarbons[3] such as methane (CH_4) and with carbon monoxide (CO), forming organic (RO_2) and hydroperoxyl (HO_2) radicals, respectively:

$$OH\cdot + CH_4\ (+O_2) \rightarrow CH_3O_2\cdot + H_2O \qquad \text{R1.3}$$

$$OH\cdot + CO\ (+O_2) \rightarrow HO_2\cdot + CO_2 \qquad \text{R1.4}$$

The fate of the peroxy radicals depends upon the level of NO_x (NO_x = NO (nitric oxide) + NO_2 (nitrogen dioxide)). Low NO_x levels (unpolluted environments) facilitate self- and cross-reactions, leading to the formation of peroxides, alcohols and aldehydes. These conditions ultimately lead to the destruction of ozone through reactions R1.1 – R1.6.

$$HO_2\cdot + RO_2\cdot \rightarrow HO_2R + O_2 \qquad \text{(where } R = H \text{ or } CH_3\text{-alkyl chain)} \qquad \text{R1.5}$$

$$CH_3O_2\cdot + CH_3O_2\cdot \rightarrow CH_3OH + HCHO + O_2 \qquad \text{R1.6}$$

Under polluted conditions, peroxy radicals react primarily with NO generating NO_2 and subsequently increasing local levels of ozone.[5] Under these conditions, self- or cross-reactions are negligible and reactions R1.7 – R1.10 dominate.

$$CH_3O_2\cdot + NO\ (+O_2) \rightarrow HCHO + NO_2 + HO_2 \qquad \text{R1.7}$$

$$HO_2\cdot + NO \rightarrow OH\cdot + NO_2 \qquad \text{R1.8}$$

$$NO_2 + h\nu \rightarrow NO + O \qquad \text{R1.9}$$

$$O + O_2 + M \rightarrow O_3 + M \qquad \text{R1.10}$$

Under polluted conditions NO can react with OH to produce nitrous acid (HONO).

$$OH\cdot + NO\ (+M) \rightarrow HONO\ (+M) \qquad \text{R1.11}$$

HONO can act as a night-time sink for OH since the primary removal process for HONO is photolysis. The photodissociation lifetime of HONO ranges from 10 minutes at high sun to 1 hour for early morning sun.[5] If HONO accumulates overnight (maximum values of ~10ppbv[5]), its photodissociation can be a significant early morning source of OH radicals before other sources become dominant (R1.1 – R1.2 & R1.8).

$$HONO + h\nu \rightarrow OH\cdot + NO \qquad \text{R1.12}$$

Seinfeld and Pandis (1998)[5] estimated the importance of each OH source using typical concentrations of gas phase precursors. Under noontime conditions at 298 K, assuming $[O_3]$ = $1.2\text{x}10^{12}$ molecules cm^{-3} (50 ppbv); $[HO_2]$ = 10^8 molecules cm^{-3} (0.004 ppbv); [NO] = $9.8\text{x}10^{11}$ molecules cm^{-3} (40 ppbv); [HONO] = $2.5\text{x}10^{10}$ molecules cm^{-3} (1 ppbv), the following OH generation rates are obtained:

(i) $O_3 + h\nu \rightarrow$ 0.22 ppb min^{-1}

(ii) $HONO + h\nu \rightarrow$ 0.097 ppb min^{-1}

(iii) $HO_2\cdot + NO \rightarrow$ 2.36 ppb min^{-1}

1.3.2 Night-time Chemistry

Since most OH sources are photolytic in nature, OH is a major oxidant primarily during daylight hours. At night it reacts with several molecules to form reservoir species. As previously mentioned, OH can react with NO to form HONO (R1.11), which will only release OH upon photolysis. OH can also react with NO_2 to form nitric acid (HNO_3).

$$OH\cdot + NO_2\ (+M) \rightarrow HNO_3\ (+M)$$ R1.13

Nitric acid is a fairly stable molecule, whose main removal mechanisms are wet or dry deposition and photolysis. Deposition results in the removal of OH from the atmosphere, while photolysis causes the release of OH and NO_2, effectively the reverse of R1.13.

With no sources available, reactions R1.3 – R1.13 produce very low night-time concentrations of OH. Night-time concentrations are estimated to be around, or below, $2x10^5$ molecules cm^{-3}.[5] Consequently, OH is a very minor oxidant during the night, allowing night-time chemistry to be dominated by the nitrate radical (NO_3).[5]

1.3.3 Alkane/OH Chemistry

Alkanes can react with OH in the same manner as methane, via hydrogen abstraction.

$$RH + OH\cdot \rightarrow R\cdot + H_2O$$ R1.14

OH radicals tend to abstract the most weakly bound hydrogen atom in the molecule. Hydroxyl attack on tertiary (-CH-) hydrogen atoms is generally faster than that on secondary ($-CH_2-$) hydrogen atoms and is slowest for primary ($-CH_3$) hydrogen atoms.[5] This reaction order reflects the stability of the resulting alkyl radical with stabilization of the radical resulting from the electron donating abilities of the attached alkyl groups. The overall rate coefficient reflects the number of available hydrogen atoms and the strengths of the C-H bonds.

As with the methyl radical, the alkyl radical reacts rapidly with O_2 under atmospheric conditions to produce an alkyl peroxy radical:

$$R\cdot + O_2\ (+M) \rightarrow RO_2\cdot\ (+M)$$ R1.15

Reaction R1.15 occurs with a room temperature rate constant of $\geq 10^{-12}$ cm^3 $molecule^{-1}$ s^{-1} at atmospheric pressure.[5;6] The rate of reaction R1.15 is at least an order of magnitude higher than

most *RH+OH* reactions and therefore can be considered to occur immediately upon the formation of the alkyl radical.

The alkyl peroxy radical can undergo reactions similar to those shown in R1.5 – R1.7. However, due to the possible branching nature of higher order alkanes, the products produced by the analogous reactions R1.16 – R1.18 are much more complex.

$$RO_2\cdot + NO \rightarrow RO\cdot + NO_2 \qquad \text{R1.16}$$

$$RO_2\cdot + HO_2\cdot \rightarrow ROOH + O_2 \qquad \text{R1.17}$$

$$R_1R_2CHO_2\cdot + R_1R_2CHO_2\cdot \rightarrow 2R_1R_2CHO\cdot + O_2 \qquad \text{R1.18a}$$

$$\rightarrow R_1R_2CHOH + R_1R_2CO + O_2 \qquad \text{R1.18b}$$

$$\rightarrow R_1R_2CHOOCHR_1R_2 + O_2 \qquad \text{R1.18c}$$

Pathway R1.18b is not accessible for tertiary RO_2 radicals, and pathway R1.18c is expected to be of negligible importance.[5] Under urban conditions, and in anthropogenically influenced continental regions, reaction with NO is the dominant reaction route for alkyl peroxy radicals.

Under tropospheric conditions, alkoxy radicals can react via unimolecular decomposition, unimolecular isomerisation, or reaction with O_2. Carbon chains fewer than five carbon atoms are too short to undergo isomerisation. The competitive processes for these compounds, therefore, are unimolecular decomposition and reaction with O_2. The alkoxy radical-O_2 reaction entails abstraction of a hydrogen atom by O_2, producing an HO_2 radical and a carbonyl species.

$$RO\cdot + O_2 \rightarrow R'CHO + HO_2\cdot \qquad \text{R1.19}$$

Due to the absence of a readily available hydrogen atom, tertiary alkoxy radicals are not expected to react with O_2.

Unimolecular decomposition of the alkoxy radical produces an alkyl radical and a carbonyl species,

$$RCH_2O\cdot \rightarrow R\cdot + HCHO$$ R1.20

$$RR_1CHO\cdot \rightarrow R\cdot + R_1CHO$$ R1.21

$$RR_1R_2CO\cdot \rightarrow R\cdot + R_1C(O)R_2$$ R1.22

Generally, reaction with O_2 is the preferred reaction pathway for primary alkoxy radicals that have C-atom chains of two or fewer C atoms in length attached to the carbonyl group.

Alkoxy radical isomerisation occurs for molecules with carbon chain lengths typically greater than five. The mechanism for isomerisation is a hydrogen shift from an alkyl side-chain to the alkoxy-O atom. An idealized reaction is written below:

$$RC(O\cdot)CH_2CH_2CH_2R \rightarrow RC(OH)CH_2CH_2C\cdot(HR)$$ R1.23

1.3.4 Alkene/OH Chemistry

Alkenes constitute approximately 10% of non-methane hydrocarbons (NMHC) in the Los Angeles air basin[5] and other US cities[7] and are major constituents of gasoline fuel and motor vehicle exhaust. Olefinic double bonds are also highly characteristic of biogenic volatile organic compounds (BVOCs) emitted by vegetation.[5] The annual emission rates for these BVOCs are an order of magnitude larger than rates for anthropogenic NMHCs.[8] Due to the presence of the double bond, these molecules are susceptible to attack by O_3 and NO_3, in addition to reaction with OH radicals. In fact, reactions of alkenes with ozone are competitive with the daytime oxidation by OH radicals.[5]

Alkenes can react with OH by hydrogen abstraction and undergo similar chemistry as alkanes, as outlined in Section 1.3.3. However, due to the higher reactivity of the double bond, addition to the double bond is the more likely reaction route, with hydrogen abstraction from alkyl groups (-CH_2-) typically accounting for <5% of the reaction with OH.[5] The importance of abstraction increases with increasing chain length. About 15% of the 1-heptene reaction with OH

is expected to proceed via hydrogen abstraction from secondary CH_2 groups.[5] The typical alkene/OH addition reaction proceeds via the following mechanism resulting in the formation of a β-hydroxyalkyl radical that subsequently reacts with oxygen to produce a β-hydroxyalkyl peroxy radical:

$$R_2CCR_2 + OH\cdot \rightarrow HOR_2CCR_2\cdot \qquad \text{R1.24}$$

$$HOR_2CCR_2\cdot + O_2 \rightarrow HOR_2CCR_2O_2\cdot \qquad \text{R1.25}$$

As with the alkyl peroxy radical, the β-hydroxyalkyl peroxy radical reacts with NO with the most probability resulting in NO_2 and an β-hydroxyalkoxy radical,

$$HOR_2CCR_2O_2\cdot + NO \rightarrow NO_2 + HOR_2CCR_2O\cdot \qquad \text{R1.26}$$

The β-hydroxyalkoxy radical can then either decompose, producing a ketone or aldehyde and a hydroxyalkyl radical, or react with O_2

$$HOR_2CCR_2O\cdot \rightarrow R_2CO + \cdot CR_2OH \qquad \text{R1.27}$$

$$HOR_2CCR_2O\cdot + O_2 \rightarrow HOR_2CCRO + RO_2\cdot \qquad \text{R1.28}$$

The branching ratios of reactions R1.27 and R1.28 are approximately 0.7 and 0.3, respectively.[5] However, the ratio increases in favour of R1.27 if the second carbon is di- or tri-substituted with alkyl groups. Essentially, for alkenes ($\geq C_3$) the decomposition pathway dominates and reaction with O_2 is negligible.[5;6] Finally, the hydroxyalkyl radical produced in R1.27 can immediately react with readily available oxygen to produce a ketone or aldehyde and a hydroperoxyl radical,

$$\cdot CR_2OH + O_2 \rightarrow R_2CO + HO_2\cdot \qquad \text{R1.29}$$

By combining reactions R1.24 to R1.29, and assuming that HO_2 reacts exclusively with NO, it can be seen that the overall result of hydroxyl attack on an alkene is conversion of two molecules of NO to NO_2 and regeneration of a hydroxyl radical. A summary of daytime tropospheric chemistry is shown in Figure 1.1.[1]

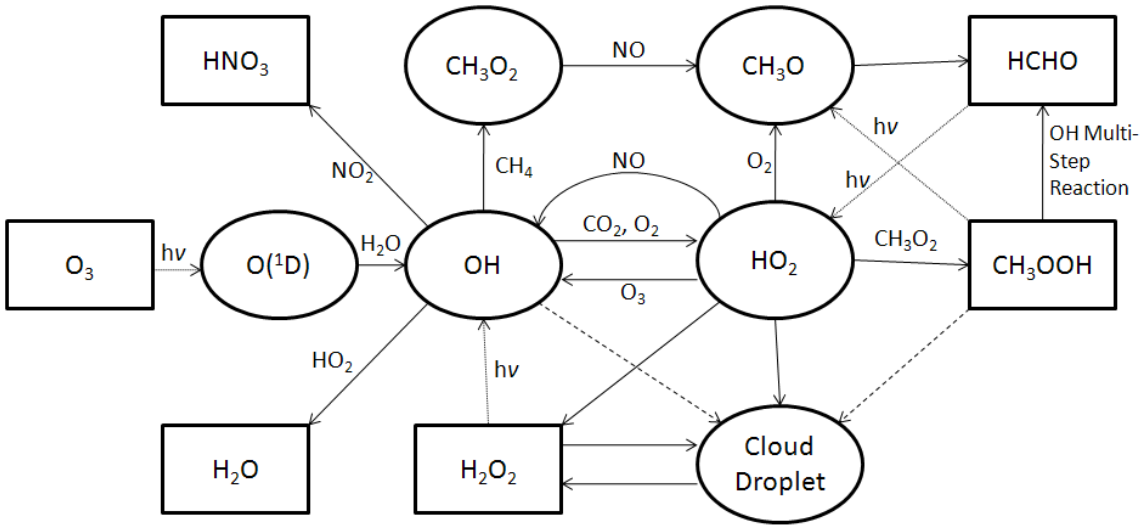

Figure 1.1: Schematic of tropospheric daytime chemistry.

1.4 Tropospheric OH Concentrations

Due to the catalytic nature of many of the reactions with trace gases, a concentration on the order of 10^6 molecules cm^{-3} is sustained during daylight hours. Modeling tropospheric chemistry suggests a seasonally, diurnally and globally averaged OH concentration of from $2x10^5$ to 10^6 molecules cm^{-3}.[5] On a more local scale, OH concentrations change rapidly on a wide variety of space and timescales. Ultraviolet radiation fluxes and water vapour concentrations are highest in the tropics, and during summer months in both the Northern and Southern Hemisphere, resulting in peak concentrations in the tropics during the summer. In addition, OH levels are predicted to be about 20% higher in the Southern Hemisphere as a result of the large amounts of CO produced by human activity in the Northern Hemisphere. However, the large production of ozone in the Northern Hemisphere industrialized areas helps to offset the destruction by co-emitted CO. This results in a Northern Hemisphere maximum at mid-latitudes in the summer. Hydroxyl radical levels are also about five times higher over the continents than over the oceans due to the low

levels of ozone precursors above the oceans. Continental OH daytime concentrations are estimated to peak around $7.5x10^6$ molecules cm^{-3}, while levels over the remote Pacific Ocean are estimated around $1.5x10^6$ molecules cm^{-3}. Prinn et al. (1992)[9] derived a global 24-hour average OH radical concentration of $(8.1 \pm 0.9)x10^5$ molecules cm^{-3}, equivalent to a 12 hour daytime average of $1.6x10^6$ molecules cm^{-3}.

1.5 Tropospheric Aerosols

An aerosol is defined as a suspension of liquid or solid particles in a gas.[6] The particles found in tropospheric aerosols consist of a wide range of elemental and molecular compounds. The chemical components comprising the most significant fractions of the total aerosol mass are sulphate, ammonium, nitrate, sea salt, mineral dust, black (elemental) carbon, and various organics.[10] These components can be formed directly from natural or anthropogenic sources (primary aerosols), or by gas-to-particle conversion in the atmosphere (secondary aerosols).[10;11] Particle diameters are typically between 0.01 and 100 µm. Particles with diameters greater than 2.5 µm are identified as coarse particles, and those with diameters < 2.5 µm are called fine particles. The fine particle mode predominates the total number and mass of aerosols.[6;11] This fine particle mode can be further classified into two groups: 1) accumulation mode, with diameters between ~0.08 and 2 µm, and 2) Aitken mode, with diameters between 0.01 and 0.08 µm. Recently, the term ultrafine particle has been used to classify particles with diameters less than 0.01 µm, and particles in this size range are often referred to as the nucleation mode.[12] Figure 1.2 shows a sample number density distribution taken from Dal Maso et al (2005).[13] This distribution highlights the accumulation, Aitken, and nucleation modes.

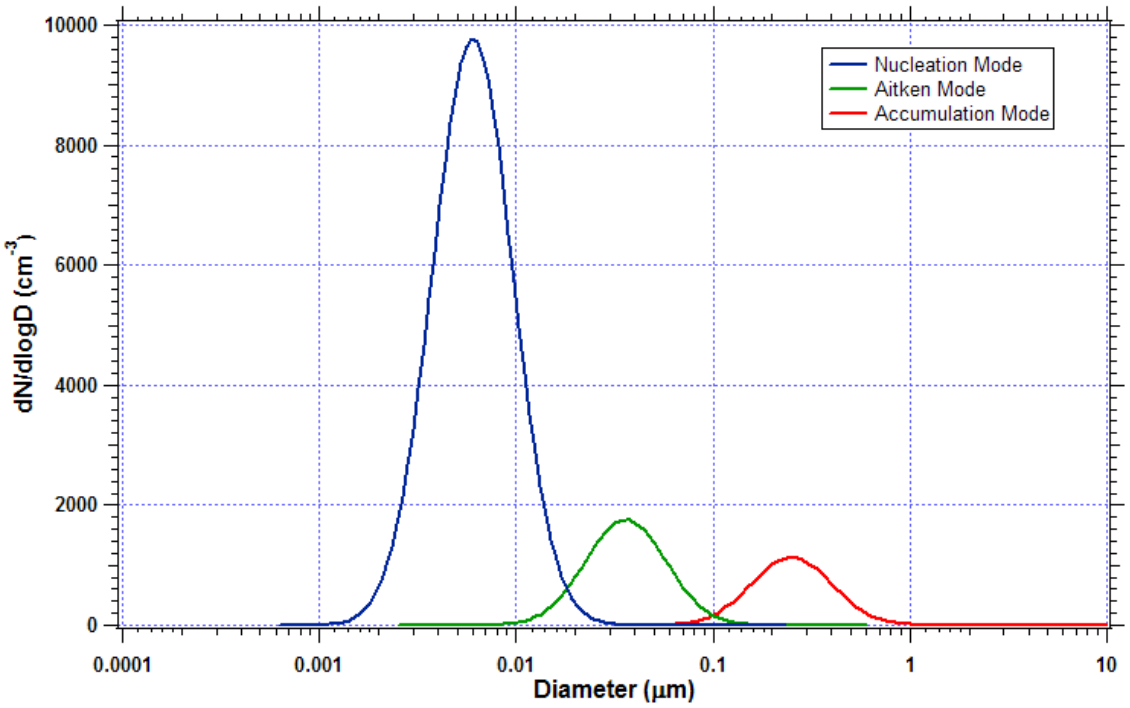

Figure 1.2: Sample size distribution from Dal Maso et al. (2005).[13]

Particles in the coarse size range are typically produced by mechanical processes such as grinding, wind, or erosion. Particles in the accumulation mode typically arise from gas-to-particle conversion of low-volatility vapours or from coagulation of smaller particles in the Aitken range with either themselves or with larger particles in the accumulation mode. Particles in the Aitken mode arise predominantly from gas-to-particle conversion. Particle number concentrations vary depending on the presence of local sources and transport of regional air masses to and from sources (i.e. dilution). Table 1.2 lists some characteristic number concentrations for various regions of the troposphere.[6]

Table 1.2: Typical Tropospheric Aerosol Number Concentrations.[6]

Type	Number Concentration (cm^{-3})
Marine	100 - 400
Remote Continental	~10^4
Urban	>10^5
Nonurban Continental	~10^3
Polar	15 - 150
Free Troposphere	~30
Biomass Burning	~10^4

1.5.1 Tropospheric Organic Aerosols

While inorganics, particularly sulphates and nitrates, tend to be ubiquitous components of tropospheric particles, in many cases, a large portion of the mass is associated with organic compounds. For example, Mazurek et al. (1997)[14] analyzed particles collected in the Grand Canyon area of the United States and found that the concentration of organics was about equal to that of sulphate. Fine particulate matter in rural and urbanized atmospheres has been shown to include semi-volatile organic aerosols[15], while marine aerosols have also been discovered with organic coatings.[16;17] Organic aerosols emitted directly to the atmosphere are referred to as Primary Organic Aerosols (POA). These aerosols can result from biomass and wood burning[18], leaf abrasion[15], ocean spray[17], and fuel and natural gas combustion.[19] Organic aerosols can also form via the condensation of low vapour pressure products that result from the reaction of gas-phase species. The aerosols formed via the condensation of low vapour pressure molecules are referred to as Secondary Organic Aerosols (SOA). Analysis indicates that biomass burning and biogenic SOA are the largest sources of organic aerosols globally, but suggests that anthropogenic sources could be as much as 50% in northern midlatitudes.[20]

The composition of organics found in aerosols is quite complex, containing alkanes, alkenes, aromatics, fatty acids, alcohols and organic acids & bases. It is often quite difficult to accurately determine the precise composition of a given aerosol sample. However, it has been

hypothesized that certain sources of organic aerosols contain particular functional groups. For example, n-alkanes in the C_{15} to C_{35} range are typical of nonurban aerosols. Furthermore, there is often a preference for compounds with odd number of carbon atoms. This is termed the Carbon Preference Index (CPI)[21], which, for alkanes, is the sum of odd carbon number alkanes over the sum of even carbon number alkanes. Therefore, a CPI > 1 for n-alkanes will often be indicative of a biogenic source. Also produced by biogenic sources are n-alkanoic acids and n-alkanols with a predominance of even carbon numbers. In this case, the CPI is defined as the ratio of even numbered carbon compounds to odd numbered carbon compounds.

Some monounsaturated fatty acids, such as $C_{16:1}$ and $C_{18:1}$ (the first number indicates the number of carbon atoms and the second number denotes the number of double bonds), are also produced biogenically. More specifically, palmitic acid (n-C_{16}) is the most abundant saturated acid, while palmitoleic acid (n-$C_{16:1}$) and oleic acid (n-$C_{18:1}$) are the most abundant unsaturated acids.[15-17;22] However, because they are expected to react fairly rapidly with tropospheric gases such as O_3, OH, and NO_3, their concentrations are highly variable. In particular, oxidation of the larger and cyclic alkenes, aromatic hydrocarbons and the larger alkanes and cycloalkanes is expected to lead to condensed-phase multifunctional organic products.[23;24] For example, field measurements indicate that C_3 to C_9 dicarboxylic acids are a predominant component of SOA.[18;25] Similar groupings can be made for anthropogenic sources of aerosols as well. Table 1.3 lists the organic groupings for typical tropospheric aerosols.[6]

Table 1.3: Common organic functional groups[6]

Source	Groupings
automobiles & heavy-duty diesel trucks	n-alkanes, n-alkanoic acids, aromatic aldehydes and acids, polycyclic aromatic hydrocarbons (PAH), oxidized PAH derivatives, steranes, pentacyclic triterpanes, and azanapthalenes
abrasion of leaf surfaces	n-alkanes, n-alkanoic and n-alkenoic acids, n-alkanols, n-alkanals, and terpenoids
natural gas combustion	n-alkanes, n-alkanoic acids, PAH, oxidized PAH derivatives, and azaarenes
wood smoke	diterpenoid acids, retene, dehydroabietic acid

The presence of long-chain organics having one or more polar functional groups in the condensed phase suggest that these may act as surfactants in aqueous atmospheric aerosols, forming an organic coating over the surface of the aerosol. A number of studies have shown that saturated and unsaturated long-chain carboxylic acids (i.e. C_{16}, C_{18}) are commonly found in sea-salt aerosols as well as on the sea surface.[16;17;26;27] Ambient aerosol particles may exhibit the following properties due to the presence of organic films: 1) reduced rate of evaporation of water, 2) inhibited transport from the gas-phase into the droplet of stable molecules and highly reactive free radicals, and 3) reduced efficiency with which particles are scavenged by larger cloud and rain droplets.[28] These properties can modify the influence particles can have on the chemistry of the atmosphere and global climate change.

1.6 Aerosols and Climate Change

Radiative forcing describes the ability of aerosols to redistribute energy in the earth's atmosphere. This forcing can increase (positive forcing) or decrease (negative forcing) the amount of radiation reaching the earth's surface. While the radiative forcing due to aerosols can have a significant impact on climate,[29] the uncertainty associated with this effect is still quite large.[30] The composition and size of the aerosol particles determines the magnitude and direction of the radiative forcing. The influence of particles on the earth's radiative balance, and therefore its climate, is separated into direct and indirect effects.

The direct effect describes the capacity of atmospheric aerosols to scatter and absorb incident solar radiation and absorb surface-emitted thermal radiation.[6;10;29] Light scattering by aerosols depends on the particle diameter, *d*, and the wavelength of light, λ. When *d* and λ are of similar magnitude scattering is at its most efficient. As shown above (Figure 1.2), the majority of aerosols fall within the size range of 0.001 – 1.0 μm in diameter, which corresponds to the wavelengths of greatest intensity in the solar spectrum (~0.35 – 1.0 μm).[5] Therefore, this radiation is strongly scattered in the atmosphere, reducing the amount of solar radiation reaching the Earth's surface (negative forcing).[29] Atmospheric aerosols, primarily as elemental carbon, can absorb solar radiation, further resulting in negative forcing.[5;31] Sulphate and elemental carbonaceous aerosols can also cause a positive forcing by absorbing outgoing terrestrial thermal radiation.[5] Positive radiative forcing is about an order of magnitude smaller than the negative forcing; producing an overall forcing that is negative.[6]

The indirect aerosol effect describes the way in which aerosols perturb the Earth's radiative balance through their influence on cloud formation and lifetime.[6;10;29] The first indirect effect, the "Twomey effect", theorizes that if the total water content of a parcel of air is held constant, then increasing the concentration of condensation nuclei results in a decrease in the size of cloud droplets, thereby enhancing the scattering of incoming solar radiation.[32] The formation of smaller cloud particles will hinder precipitation, since smaller particles are less likely to be affected by gravitational forces.[6] This dampening of precipitation results in longer cloud lifetimes and is referred to as the second indirect effect. As cloud lifetimes increase, the fractional cloud cover increases, resulting in an enhancement of the negative forcing due to the scattering of short-wave radiation by cloud droplets.[31] The overall forcing due to aerosols (the sum of all direct and indirect effects) is estimated to be negative, with a value in the range of -1 to -2 W m^{-2}.[10;30]

1.7 Aerosol Chemistry

The organic content of aerosols is expected to react with oxidants (e.g. OH, O_3, NO_3) to form oxygenated volatile organic compounds (OVOCs) in a similar manner as gas-phase molecules, as outlined above.[33] These OVOCs can directly affect the aerosol's ability to take up water and grow (CCN activity) by changing the surface tension and bulk hygroscopicity of the particle.[34] Rubel & Gentry (1985)[35] found that the mass accommodation coefficient for water decreased from $8x10^{-3}$ to $4x10^{-4}$ as the coverage of hexadecanol increased. The footprint of OVOCs on an aerosol surface will grow as the molecule becomes more oxidized. This increase in molecule functionality can lead to a decreased ability to hinder mass transfer across the interface due to a now more loosely packed surface coating. The degree of compression of the film will dictate the magnitude of its effects on uptake and evaporation from the particle. For example, a compressed film is expected to be less permeable. Daumer et al. (1992)[36] showed that straight-chained organic molecules coating sulphuric acid aerosol particles slowed the rate of neutralization by ammonia. However, the presence of branched molecules did not slow the rate of neutralization. They concluded that the difference in neutralization rates was a result of a more permeable film created by the branched organic molecules. The increase in functionality of the surface molecules can also lead to an increase in hydrophilicity, hindering the transport of water away from the particle surface. Shulman et al. (1997)[37] demonstrated that the presence of difunctional oxygenated organics on the surface of aqueous particles lowered the evaporation rate of water from the particles.

The influence of aerosols on the chemistry of the lower atmosphere depends on both the aerosol composition and make-up of the surrounding atmosphere. For example, Emmerson et al. (2007)[38], measuring radical concentrations downwind of London, England, showed that the heterogeneous chemistry of aerosols can be a minor factor in the budget of HO_2 chemistry.

However, they found that the measured OH concentrations were accurately modeled using only gas-phase chemistry. Similarly, Sadanaga et al. (2004)[39] concluded that OH uptake on aerosol surfaces could not account for their observed disagreement between measured and calculated OH reactivity in a suburban area of Tokyo, Japan, concluding that it was of very minor importance. Other studies have also suggested that under polluted conditions heterogeneous chemistry is not needed to fully explain the reactivity of OH.[40]

Di Carlo et al. (2004)[41], on the other hand, measured OH reactivity in an unpolluted forested region and found that their calculated reactivity from OH observations was underestimated by a model that included only gas-phase chemistry. Their conclusion was that they were simply not including enough gas-phase chemistry in their model and that the missing reactivity could be explained by the inclusion of higher levels of VOC emissions. While measuring BVOC fluxes at the same site, Ortega et al. (2007)[42] suggested that the inability of Di Carlo et al. to correctly model OH concentrations may imply the presence of important heterogeneous chemistry and that the inclusion of more reactive gas-phase chemistry had no physical basis since their measured levels of BVOCs did not match that required by the Di Carlo et al. measurements to account for the missing reactivity. Other field studies have also suggested the importance of a missing sink for OH chemistry, typically in unpolluted air and/or with the possibility for the presence of large amounts of organic aerosols.[43-47] Other field studies, in similar environments, find that while their models may over predict OH concentrations or under predict reactivity, the discrepancy is usually within the error of the model, typically ~15-25%.[48-50] These studies, therefore, concluded that their models agreed with their measured results. However, the inclusion of heterogeneous chemistry in these models could improve the agreement between field measurements and model predictions. Therefore, there is a clear need to determine

if, and under what conditions, heterogeneous chemistry could play a role in the budget of the hydroxyl radical.

Heterogeneous chemistry can also be an important sink for organic molecules of high molecular weight and/or low volatility. For these compounds, the gas-phase chemistry can be a very minor pathway due to the low concentrations of the organics. It has been shown that the rate of heterogeneous reactions of atmospheric oxidants with semi-volatile organic compounds (SVOCs) can exceed the gas-phase reaction for the same compound.[51]

The ability to physically and/or chemically distinguish different fractions of organic aerosols is critical to constraining source estimates. The understanding of the heterogeneous chemistry of aerosols can also help in determining sources of aerosols. As listed in Table 1.3, certain molecular markers are used as tracers of sources of aerosols. For example, steranes and triterpanoid hopanes are important markers for motor vehicle emissions.[52] A critical assumption underlying the use of molecular markers in source apportionment models is that these species are chemically stable.[52] Field measurements, however, indicate that hopanes and steranes may be oxidized in regional air masses.[53] Therefore, a better understanding of the influence of oxidation on particle composition will allow for more accurate modeling and determination of aerosol sources for the purposes of policy-making decisions.

1.8 Anthropogenic Concerns

Ever since the Industrial Revolution, humans have added vast quantities of chemicals, gaseous and particulate, into the Earth's atmosphere. Many of these compounds act to change the composition of the atmosphere directly or indirectly. These changes in composition can have detrimental or compensating effects on the Earth's climate, human health, plant life, and many other aspects of the biosphere.[54;55] It is believed that tropospheric ozone concentrations have increased by a factor of five or six in the Northern Hemisphere over the last 100 years.[56;57]

Nitrogen deposition has risen due to the emission of substantial amounts of nitrogen oxides (NO_x) that are emitted each year.[58-60] Carbon dioxide levels have increased by approximately 50 ppmv in the last 50 years alone.[5] Aerosol loading is estimated to have increased 50 to 300% over remote regions of most continents.[61]

A major concern of scientists is the ability to forecast future levels of these gases and particulates so as to predict their impact on climate and the biosphere. To accurately predict the levels of atmospheric compounds in the future, a thorough understanding of all processes and variables involved in the emission and sequestering of these compounds is essential. For example, decreasing stratospheric ozone concentrations can increase the flux of <310 nm radiation reaching the troposphere. Combining this with increases in tropospheric levels of ozone could result in an increased production of tropospheric OH by the increased production of $O(^1D)$.[62]

One variable that is poorly understood is the role of aerosols in affecting the chemistry of the atmosphere. As demonstrated above, aerosols affect the Earth's radiation balance, cloud properties, the hydrological cycle, human health, and in particular the chemistry of the atmosphere. However, some of the mechanisms and feedbacks of this influence are still poorly understood. It is therefore imperative to study the chemistry of aerosols to increase our knowledge and understanding of their influence on the atmosphere.

1.9 Summary

The hydroxyl radical has a short lifetime (<1s in mid-latitude continental boundary layer[38]) and so its concentration is not directly affected by transport. Rather, the budget of OH is controlled by local variations in O_3, H_2O, VOCs, CO, NO_x, and sunlight. A single OH radical can initiate the degradation of many molecules of trace gases leading to not only their eventual removal from the atmosphere but also the formation of tropospheric ozone. Knowledge of atmospheric hydroxyl

radical levels, and the chemical processes that govern its abundance, is central to explaining current atmospheric trace gas distributions and predicting their likely future evolution. Despite the potential significance of the role of aerosols in the budget of atmospheric oxidants, only a relatively small number of experimental studies have measured the reactive uptake of OH with organic surfaces[33;63;64] and aerosols.[65-71] It is therefore of interest to learn how these oxidants, in particular OH, react with the organic aerosol surface.

The objective of the research presented in this thesis is to develop a new method for the investigation of the heterogeneous interaction between OH and organic aerosols. The theoretical and mathematical framework for this interaction is outlined in Chapter 2. Also included in Chapter 2 is a brief discussion of current methods used in studying heterogeneous chemistry and how they influenced the experiments developed in this thesis. Chapter 3 details the technique developed and refined during the course this research. This technique (as a whole) is new and no measurement at this level of detail has ever been used to study heterogeneous kinetics. Chapter 4 focuses on the study of the kinetics of the reaction between pure oleic acid aerosols and OH. The results of this research are used to make inferences about the importance of the reaction between OH and the aerosol surface, as well as the significance of the reaction in the study of tropospheric chemistry.

Chapter 2
Uptake Theory and Experimental Techniques

2.1 Uptake Theory

Interactions between gas-phase molecules and an aerosol, or a surface, can be described as follows: First, the molecule must diffuse to the surface. The molecule then collides with and thermally accommodates onto the surface. The adsorbed molecule may desorb or enter into the bulk material, or possibly even react on the surface. Surface reactions can involve either the surface material or another adsorbed species. After entering the bulk, a fraction of the molecules may evaporate back to the gas-phase due to the limited solubility of a species in a liquid, governed by Henry's Law. Chemical reactions in the bulk can also occur, which provide a sink for the molecule and reduce the effect of saturation. In this case, uptake is determined by the rate of reaction in the bulk. In thin films, or large aerosols, bulk-phase diffusion may need to be considered in order to transport molecules to reaction sites (i.e. surface). All of these processes are summarized schematically in Figure 2.1.[72]

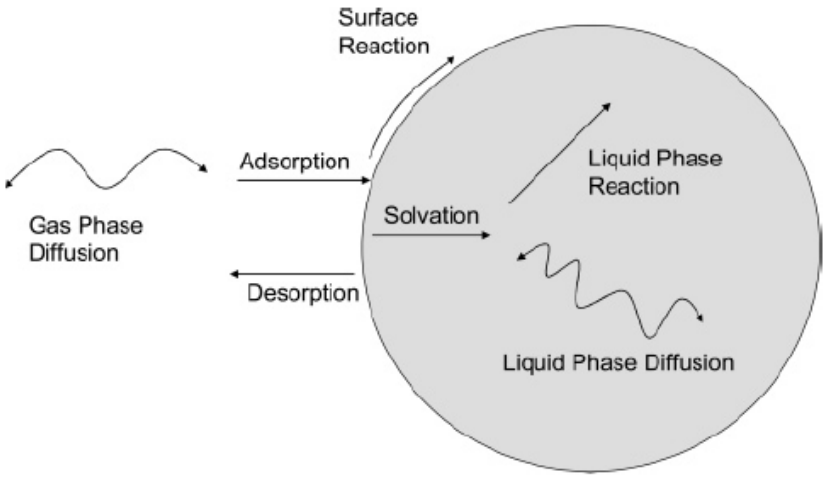

Figure 2.1: Schematic of transport processes at air-surface interface.

2.2 Mathematical Model

All of the processes described above can be summarized by analogy with Ohm's law, initially developed by Schwartz et al. (1986).[73] This model uses the idea of electrical resistance to summarize each process in the uptake and accommodation of the gas-phase molecule, where each term is the inverse of an uptake coefficient. Referring to Figure 2.2, it becomes clear how each process can react in series or in parallel with the various other processes.[74]

Term	Definition
Γ_{diff}	conductance due to gas-phase diffusion
S	adsorption coefficient
α	mass accommodation coefficient
Γ_s	conductance due to surface reactions
Γ_{rxn}	conductance due to bulk-phase reactions
Γ_{sol}	conductance due to bulk solubility

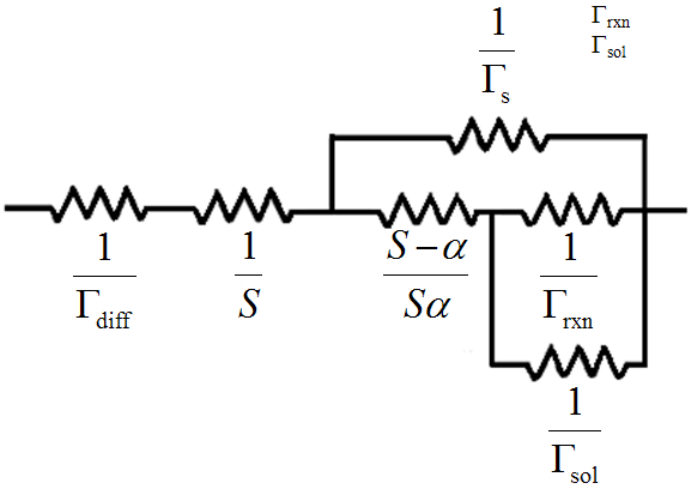

Figure 2.2: Electrical circuit analogue for gas-phase uptake processes.

This whole process can be described by an uptake coefficient, γ, which is defined as the probability that a collision of a molecule with the particle's surface leads to its net uptake into the condensed phase.

$$\gamma = \frac{number\ of\ molecules\ lost}{number\ of\ molecules\ colliding\ with\ the\ surface} \qquad \text{Eq2.1}$$

Using the resistance model in Figure 2.2 a formal mathematic definition of the uptake coefficient can be defined as follows

$$\frac{1}{\gamma} = \frac{1}{\Gamma_{diff}} + \frac{1}{S} + \frac{1}{\Gamma_s + \frac{1}{\frac{S-\alpha}{S\alpha} + \frac{1}{\Gamma_{rxn} + \Gamma_{sol}}}} \qquad \text{Eq2.2}$$

where Γ_{diff} is a measure of the conductance by gas phase diffusion, Γ_s is a measure of the conductance due to surface reaction, α is the mass accommodation coefficient, S is the adsorption coefficient, Γ_{sol} is a measure of the conductance due to the solubility and Γ_{rxn} is a measure of the conductance by bulk-phase chemical reactions within the particle. α is defined as the ratio of the number of molecules entering the liquid phase to the number of molecules colliding with the surface, and S is defined as the fraction of collisions with the surface that result in accommodation on the surface. General solutions to the uptake equation are not commonly available; however, solutions can be found under various restricted conditions. This will be discussed in a later section.

The individual processes shall be treated in terms of the rate of transfer of gas across a surface of unit area per second. However, this rate is typically expressed, as in Eq2.1, relative to the number of gas-surface collisions per second. The rate of collision (molecule m^{-2} s^{-1}) is given by kinetic molecular theory as[6]

$$Number\ of\ Collisions = \frac{N_g u_{av}}{4} = N_g \sqrt{\frac{RT}{2\pi M}} \qquad \text{Eq2.3}$$

where N_g is the gas concentration (molecules m^{-3}), u_g is the average gas-phase molecular speed (m s^{-1}), R is the gas constant (J K^{-1} mol^{-1}), T is the temperature (K) and M is the molecular weight (kg) of the gas. It is these normalized rates that define the conductance (Γ), or resistance ($1/\Gamma$), for each process.

2.2.1 Gas-Phase Diffusion

An empirical formulation of isothermal diffusive transport has been developed to accurately describe gas-phase diffusion to the aerosol surface[75]

$$\frac{1}{\Gamma_{\text{diff}}} = \frac{0.75 + 0.283Kn}{Kn(1 + Kn)} \qquad \text{Eq2.4}$$

where *Kn* is the Knudsen number. The Knudsen number is defined as the ratio of the molecular mean free path length (λ) to a representative physical length scale (*a*), in this case the radius of the particle. Mathematically, $Kn = \lambda/a$ and is a dimensionless number. The mean free path is expressed as $\lambda = 3D_g/u_{av}$ (m) where D_g is the gas-phase diffusion coefficient ($m^2\ s^{-1}$) of the trace species. The average molecular speed, u_{av} ($m\ s^{-1}$), is defined as $u_{av} \cong 145.5\sqrt{(T/M)}$, where *T* is the temperature (K) and *M* is the molar mass (kg). The Knudsen number is useful for determining whether statistical mechanics or the continuum mechanics formulation of fluid dynamics should be used to describe the system of interest. A Knudsen number greater than one indicates that the mean free path of a molecule is comparable to the length scale of the system and collisions between molecules occur infrequently. Therefore, the continuum assumption of fluid mechanics is no longer a good approximation.[76] In these situations statistical methods must be used in order to fully describe fluid mechanics. The formulation for Eq2.4 takes into account the resistance of gas-phase diffusion to uptake of the molecule into the surface. This equation also accounts for the gradient in gas-phase concentration due to the flux of gas into the particle.

Considering Eq2.4, it is evident that as the Knudsen number increases (i.e. $Kn >> 1$), $1/\Gamma_{\text{diff}}$ gets smaller and contributes less to the overall uptake equation ($1/\gamma$). The physical interpretation is that since *Kn* is proportional to the gas-phase diffusion coefficient (D_g), *Kn* gets larger as a result of an increase in the diffusion coefficient. As the diffusion coefficient increases diffusion to the particle surface becomes faster, and therefore does not limit uptake of the

molecule. In the atmosphere, gas-phase diffusion does not usually limit uptake onto sub-micron particles.[72]

Fuchs and Sutugin (1990)[75] also show that for small Knudsen numbers, implying slow gas phase diffusion, the rate of diffusion (molecules s^{-1}) of the gas to the particle surface of radius *a* is

$$Rate\ of\ Diffusion = 4\pi D_g a N_g \qquad \text{Eq2.5}$$

Normalizing this to the surface area of the particle yields the rate of diffusion (molecules m^{-2} s^{-1}) as

$$Rate\ of\ Diffusion = \frac{4\pi D_g a N_g}{4\pi a^2} = \frac{2 D_g N_g}{d} \qquad \text{Eq2.6}$$

where $d = 2a$ is the particle diameter. Normalizing to the rate of collisions yields

$$\Gamma_{\text{diff}} = \frac{8 D_g}{u_{av} d} \qquad \text{Eq2.7}$$

2.2.2 Mass Accommodation

The mass accommodation coefficient, α, can be used to describe the interfacial resistance to mass transport. The mass accommodation coefficient can be defined as:

$$\alpha = \frac{number\ of\ molecules\ entering\ liquid\ phase}{number\ of\ molecular\ collisions\ with\ surface} \qquad \text{Eq2.8}$$

This means that in the absence of chemical reactions, α determines the maximum possible flux of trace species into the liquid. The mass accommodation coefficient can be expressed as[74]

$$\frac{1}{\alpha} = \frac{1}{S} + \frac{k_{des}}{S k_{sol}} \qquad \text{Eq2.9}$$

where, k_{sol} and k_{des} are the rate coefficients of solvation and desorption from the surface, respectively. The ratio of the two rate coefficients is the true measure of interfacial kinetic

resistance. It is noted that since $1/\alpha$ already describes the interfacial resistance, Eq2.9 is not normalized to the rate of collisions.

2.2.3 Solubility and Diffusion in the Liquid Phase

After a molecule accommodates to the particle surface it can either react on the particle surface or solvate into solution. The solubility term can be described using Fick's Law. Consider a volume bounded on opposite sides by Plane *x* and Plane *x*+*dx*. From Fick's Second Law, the rate of change of concentration (c) with time (t) in the bulk, assuming no reactions occur, is given as

$$\frac{dc}{dt} = D_l \frac{d^2c}{dx^2} \qquad \text{Eq2.10}$$

where D_l is the liquid phase diffusion coefficient ($m^2\ s^{-1}$), and (d^2c/dx^2) is the rate of change of the concentration gradient at *x*. The rate of transfer (molecules $m^{-2}\ s^{-1}$) of the species across Plane *x*, at $x = 0$, is given by Fick's First Law

$$Rate = -D_l \left(\frac{dc}{dx}\right)_{x=0} \qquad \text{Eq2.11}$$

At time = 0, the concentration of the species of interest in the bulk can be defined as $c_{l,bulk}$, which is also the concentration in the bulk at $x = \infty$ at $t > 0$. If the concentration at the surface of the particle is defined as $c_{l,interface}$ then under these conditions Eq2.10 can be solved to obtain the rate of transfer per unit surface area after exposure time *t*.[77]

$$Rate = \left(c_{l,interface} - c_{l,bulk}\right)\sqrt{\frac{D_l}{\pi t}} \qquad \text{Eq2.12}$$

When considering a freshly emitted particle, $c_{l,bulk}$ will equal zero. Therefore, the rate equation simplifies to

$$Rate = \left(c_{l,interface}\right)\sqrt{\frac{D_l}{\pi t}} \qquad \text{Eq2.13}$$

If the species of interest is in Henry's Law equilibrium, $H = c/P_X$, with the surrounding environment, then the concentration at the interface of the particle is related to the gas-phase concentration, N_g (molecules m^{-3}), by $c_{l,interface} = N_g HRT$. This further simplifies the rate equation to

$$Rate = N_g HRT\sqrt{\frac{D_l}{\pi t}} \qquad \text{Eq2.14}$$

Normalizing this to the rate of gas-surface collisions yields

$$\Gamma_{sol} = \frac{4HRT}{u_{av}}\sqrt{\frac{D_l}{\pi t}} \qquad \text{Eq2.15}$$

2.2.4 Reaction within a Particle

The reaction of two species, Y and X, within the bulk involves the accommodation of X followed by reaction with Y. This mechanism implies that the rate of reaction depends both on the solubility and the rate of diffusion of X within the particle. Modifying Fick's Second Law to include a first-order reaction, with rate coefficient k (s^{-1}), yields the rate of change of concentration with time

$$\frac{dc}{dt} = D_l\frac{d^2c}{dx^2} - kc \qquad \text{Eq2.16}$$

This equation can be solved in the same manner as Eq2.10, using the same boundary conditions.[77] Under these conditions, the rate of transfer is given as

$$Rate = \left(c_{l,interface}\right)\sqrt{D_l k} \qquad \text{Eq2.17}$$

Normalizing this to the rate of gas-surface collisions yields

$$\Gamma_{rxn} = \frac{4HRT}{u_{av}}\sqrt{D_l k} \qquad \text{Eq2.18}$$

It should be noted that this expression applies to irreversible reactions or cases where the solubility of the reaction product is very large.

A more general expression for Γ_{rxn} is given by[78]

$$\Gamma_{rxn} = \frac{4HRT}{u_{av}}\sqrt{D_l k}\{coth(a/l) - (l/a)\} \qquad \text{Eq2.19}$$

The term *l* is defined as the reacto-diffusive length and describes the effective depth of liquid in which reaction occurs. It is defined as $l = (D_l/k)^{1/2}$, and *a* is again defined as the radius of the particle, or depth of the bulk liquid. The value of *l* reflects the steady-state concentration gradient in reactant *X* below the surface of the particle, accounting for competition between reaction with *Y* and diffusion of *X* into the particle. A small value of *l* relative to the depth of the surface (or radius of the particle) indicates reaction close to the surface and the size-dependent term {coth(*a*/*l*)-(*l*/*a*)} approaches unity. A large value of *l* relative to the depth of the surface indicates that reaction occurs throughout the entire bulk phase and the size-dependent term approaches *a*/(3*l*).

2.2.5 Surface Reaction

Hanson and Ravishankara (1994)[79] derived an expression for uptake due to surface reaction, Γ_s, by breaking down the net flux from the gas-phase to the liquid into a flux due to loss at the surface and a flux due to loss within the liquid.

$$J_{uptake} = J_{surf} + J_{liquid} \qquad \text{Eq2.20}$$

$$\gamma\frac{u_{av}}{4}c_g = c_s k_s + D_l\left|\frac{\delta c}{\delta z}\right|_{surf} \qquad \text{Eq2.21}$$

The uptake term includes the net uptake coefficient, γ, and the gas-kinetic flux, $(u_{av}/4)c_g$. Here c_g is the gas-phase number density at the surface (molecules m^{-3}) and u_{av} is the mean molecular speed (m s^{-1}). The surface loss term involves the concentration at the interface, c_s (molecules m^{-2}), multiplied by the pseudo-first-order loss rate coefficient, k_s (s^{-1}), at the surface. The last term is the diffuso-reactive flux into the bulk liquid due to the concentration gradient within the liquid evaluated at the surface (D_l is the liquid-phase diffusion coefficient for the molecule of interest). Solving Eq2.21 for γ and simplifying the resulting equation yields a term for uptake due to surface reaction:

$$\Gamma_s = \frac{4k_s b'}{u_{av}} \qquad \text{Eq2.22}$$

Hanson (1997)[80] noted that b' is related to the mass-transfer rate coefficients describing adsorption, k_{ads}, and desorption, k_{des}, from the surface.

$$b' = k_{ads}/k_{des} \qquad \text{Eq2.23}$$

Therefore, we can simplify this equation with a substitution for b'

$$\Gamma_s = \frac{4k_s k_{ads}}{u_{av} k_{des}} \qquad \text{Eq2.24}$$

2.3 General Solutions

As previously mentioned, general solutions to the uptake equation are not commonly available. However, by analyzing the overall uptake equation, solutions can be found under various restricted conditions. These restricted conditions often describe the conditions of various experimental methods used to measure the uptake coefficient. It is important to remember when simplifying Eq2.2 that if a process is believed to not occur (e.g. no reactions possible) then the resistance, $1/\Gamma$, to that process is infinitely large. Consequently, the conductance, Γ, to that process is extremely small.

2.3.1 Adsorption Coefficient

Reactions of the trace species with molecules present in the aerosols (either the bulk-phase or trace constituents) provide a sink for the trace species. This results in limiting saturation (i.e. re-evaporation of accommodated gas molecules) and consequently enhancing uptake. Therefore, k_{des} is very small and Eq2.9 can be re-written as

$$\frac{1}{\alpha} = \frac{1}{S} \qquad \text{Eq2.25}$$

Substituting Eq2.25 into Eq2.2 yields an uptake equation that involves only mass accommodation at the surface, bulk-phase reactions and solubility, and surface reactions.

$$\frac{1}{\gamma_{meas}} = \frac{1}{\Gamma_{\text{diff}}} + \frac{1}{\alpha} + \frac{1}{\Gamma_{\text{s}} + \Gamma_{\text{rxn}} + \Gamma_{\text{sol}}} \qquad \text{Eq2.26}$$

2.3.2 Fast gas transport and/or fast reactions

In this case, fast gas transport results in a high conductance, Γ_{diff}, of the molecule to the particle surface. Fast reactions, combined with high solubility, imply that all processes in the bulk of the particle, Γ_{s}, Γ_{rxn}, and Γ_{sol}, have a large conductance. Therefore, uptake is limited only by mass accommodation and the measured uptake coefficient is the effective mass accommodation coefficient, $1/\gamma_{meas} = 1/\alpha$. Low solubility and fast reactions imply that $\Gamma_{\text{s}} \approx \Gamma_{\text{rxn}} >> \Gamma_{\text{sol}}$, and with Γ_{diff} very large the net uptake is simplified to

$$\frac{1}{\gamma_{meas}} = \frac{1}{\alpha} + \frac{1}{\Gamma_{\text{s}} + \Gamma_{\text{rxn}}} \qquad \text{Eq2.27}$$

2.3.3 High Solubility, no reaction

In this case, the rate of mass transfer due to diffusion and solubility in the bulk is large. Therefore, the measured uptake coefficient is, effectively, the mass accommodation coefficient, corrected for the rate of gas-phase diffusion.

$$\frac{1}{\gamma_{meas}} = \frac{1}{\Gamma_{\text{diff}}} + \frac{1}{S} + \frac{S-\alpha}{S\alpha} \qquad \text{Eq2.28}$$

If the last two terms are combined in Eq2.28, they reduce to $1/\alpha$, yielding the simpler equation

$$\frac{1}{\gamma_{meas}} = \frac{1}{\Gamma_{\text{diff}}} + \frac{1}{\alpha} \qquad \text{Eq2.29}$$

2.3.4 Limited Solubility, no reaction

Like the previous case, the measured uptake coefficient is largely dependent on gas-phase diffusion and mass accommodation. However, now the uptake must be corrected for the trace species low solubility, and $1/\gamma_{meas}$ is

$$\frac{1}{\gamma_{meas}} = \frac{1}{\Gamma_{\text{diff}}} + \frac{1}{S} + \frac{1}{\frac{1}{\frac{S-\alpha}{S\alpha} + \frac{1}{\Gamma_{\text{sol}}}}} \qquad \text{Eq2.30}$$

However, if solubility is high enough then desorption of the accommodating species is slow. Therefore, k_{des} is really small and $\alpha \sim S$, resulting in a measured uptake coefficient of

$$\frac{1}{\gamma_{meas}} = \frac{1}{\Gamma_{\text{diff}}} + \frac{1}{\alpha} + \frac{1}{\Gamma_{\text{sol}}} \qquad \text{Eq2.31}$$

2.3.5 Gas transport and mass accommodation fast

In this case, γ_{meas} is determined by the solubility and reactivity of the trace species, as given by

$$\frac{1}{\gamma_{meas}} = \frac{1}{\Gamma_{\text{s}} + \Gamma_{\text{rxn}} + \Gamma_{\text{sol}}} \qquad \text{Eq2.32}$$

This case can be further simplified if the trace species only reacts with other trace species in the bulk, i.e. $\Gamma_s = 0$. Then the measured uptake depends only on the bulk reactivity and solubility of the trace species.

$$\frac{1}{\gamma_{meas}} = \frac{1}{\Gamma_{\text{rxn}} + \Gamma_{\text{sol}}} \qquad \text{Eq2.33}$$

Table 2.1: Summary of simplified uptake scenarios.

Simplification	Uptake Coefficient
Fast gas transport, high solubility, and/or fast reactions	$\frac{1}{\gamma_{meas}} = \frac{1}{\alpha}$
Fast gas transport, low solubility, and fast reaction	$\frac{1}{\gamma_{meas}} = \frac{1}{\alpha} + \frac{1}{\Gamma_{\text{s}} + \Gamma_{\text{rxn}}}$
High solubility, no reaction	$\frac{1}{\gamma_{meas}} = \frac{1}{\Gamma_{\text{diff}}} + \frac{1}{\alpha}$
Limited solubility, no reaction	$\frac{1}{\gamma_{meas}} = \frac{1}{\Gamma_{\text{diff}}} + \frac{1}{\alpha} + \frac{1}{\Gamma_{\text{sol}}}$
Gas transport and mass accommodation fast	$\frac{1}{\gamma_{meas}} = \frac{1}{\Gamma_{\text{rxn}} + \Gamma_{\text{sol}}}$

2.4 Experimental Model

The process of interest with the experiments outlined in this thesis is the interaction of the gas-phase reactive species and the particle. The key is to generate experimental conditions that simplify the uptake equation to allow for the accurate calculation of uptake at the particle surface. The equations above then allow for a more detailed explanation of the uptake process describing solubility and reactivity on a molecular level.

For example, if an environment can be created such that diffusion to the aerosol surface is fast, then the uptake corresponding with diffusion (Γ_{diff}) is large, and hence $1/\Gamma_{\text{diff}}$ is small and can be neglected. This results in uptake being limited only by mass accommodation, solvation and reactions.

$$\frac{1}{\gamma} = \frac{1}{S} + \frac{1}{\Gamma_{\text{s}} + \frac{1}{\frac{S-\alpha}{S\alpha} + \frac{1}{\Gamma_{\text{rxn}} + \Gamma_{\text{sol}}}}} \qquad \text{Eq2.34}$$

As previously mentioned, when reactions in the bulk and on the surface are present then the value of the mass accommodation coefficient approaches the adsorption coefficient, $\alpha \sim S$. Replacing α for S into Eq2.34 yields an uptake equation that involves only mass accommodation at the surface, bulk-phase and surface reactions, and solvation.

$$\frac{1}{\gamma} = \frac{1}{\alpha} + \frac{1}{\Gamma_s + \Gamma_{rxn} + \Gamma_{sol}} \qquad \text{Eq2.35}$$

The thermal or adsorption accommodation coefficient, S, is typically close to unity for gas-liquid collisions occurring at or near room temperature thermal speeds.[81] As a result, the mass accommodation coefficient is close to unity and $1/\alpha$ cannot be ignored in Eq2.35. Furthermore, it is not necessarily known beforehand which processes will dominate, reactions or solvation. Replacing the equations for Γ_s, Γ_{rxn}, and Γ_{sol} into Eq2.35 yields an uptake equation for the experimental conditions in Eq2.36

$$\frac{1}{\gamma_{meas}} = \frac{1}{\alpha} + \frac{u_{av}}{4}\left[\frac{k_s k_{ads}}{k_{des}} + HRT\sqrt{D_l}\left(\sqrt{k} + \sqrt{\frac{1}{\pi t}}\right)\right]^{-1} \qquad \text{Eq2.36}$$

Remorov and George (2006)[82]showed that $k = k_s/\beta$, or $\beta k = k_s$, where β is merely the ratio of surface excess to bulk concentration and tells us the relevance of surface reactions to bulk-phase reactions, k is the pseudo-first order bulk-phase rate coefficient (s^{-1}), and k_s is the surface rate coefficient (s^{-1}). Therefore, we can simplify this equation further by replacing k_s with βk.

$$\frac{1}{\gamma_{meas}} = \frac{1}{\alpha} + \frac{u_{av}}{4}\left[\frac{\beta k k_{ads}}{k_{des}} + HRT\sqrt{D_l}\left(\sqrt{k} + \sqrt{\frac{1}{\pi t}}\right)\right]^{-1} \qquad \text{Eq2.37}$$

However, since the diffusion limiting term, Γ_{diff}, is rarely zero, a small correction is usually made to account for this diffusion, such that

$$\frac{1}{\gamma_{net}} = \frac{1}{\gamma_{meas}} - \frac{1}{\Gamma_{\text{diff}}} \qquad \text{Eq2.38}$$

Therefore, from Eq2.37, if k_{ads}, k_{des} and D_l are known, or can be estimated, the pseudo-first order rate coefficient, k, for reaction in the bulk can be calculated. This in turn allows for the calculation of the surface reaction rate coefficient, k_s, if β is known or estimated. Conversely, if a value of k is already known, then the ratio of the adsorption/desorption rate coefficients can be calculated. This implies that if the experimental method is designed correctly, not only can the bulk uptake by the aerosol be described by γ_{net}, but the entire process can also be described at the molecular level.

2.5 Uptake Experimental Techniques

A wide variety of experimental methods exist for the measurement and determination of uptake coefficients, many of which are commonly found throughout the literature.[33;63;65;68;70;83-89] Each method has its own advantages and disadvantages. Some of the more commonly used methods will be discussed below with explanations and reasons for the procedures chosen for the experiments outlined in this thesis. A list of all the methods and their advantages and disadvantages are summarized in Table 2.2.

2.5.1 Knudsen Cells

Much of the early work regarding heterogeneous chemistry was performed using Knudsen cells.[83;85;86;90-95] The reactive species of interest is introduced into a chamber kept at low pressure, typically < 10 mTorr. Once in the chamber, the reactant is exposed to a surface of interest (e.g. soot[85;94;95], salt particles[83], metal oxide particles[86;92;93]). The concentration of the reactant is measured by sampling from an orifice at the opposite end of the chamber of the inlet and detected, typically, by mass spectrometry. The reactive species is monitored in the presence and absence of the surface, and over a relatively long time period, on the order of minutes.

The net uptake coefficient is calculated from the known areas of the surface (A_s) and the sampling orifice (A_h), as well as the concentration before (N_o) and after exposure (N_r) to the surface.

$$\gamma_{meas} = \frac{A_h}{A_s} \cdot \frac{N_o - N_r}{N_r} \qquad \text{Eq2.39}$$

Since Eq2.39 is dependent on the ratio of gas molecules before and after reaction, measurement of the absolute concentrations of the reactive species is not necessary but rather just relative values. Since the experiments are operated at low pressures, diffusion to the surface of interest is thought to occur quickly and γ_{meas} need not be corrected for gas-phase diffusion.

With Knudsen cell experiments, care must be taken to avoid "saturation" of the reactive surface. For uptake of reactive species, such as OH, a surface could be completely reacted in 10 ms if every collision leads to reaction for typical operating conditions in Knudsen cell experiments. However, this does provide the possibility of measuring the change in uptake as the composition of the surface changes over time.

Another challenge with Knudsen cell experiments is that the measured uptake may not represent the true uptake by the surface if re-evaporation into the gas-phase occurs over the long time scales of the experiments. This implies that as $t \rightarrow 0$ (i.e. initial exposure of the surface), the measured uptake is effectively the mass accommodation coefficient. One additional difficulty with the use of Knudsen cells to determine uptake on aerosols is the influence of the Kelvin Effect, which describes the increase in vapour pressure for a substance over a curved surface relative to a flat surface.[6] This increase in vapour pressure can limit the solubility of reactive gases for small particles with diameters less than a few hundred nanometres.[96-98] As shown above, the rate of a heterogeneous reaction in a liquid aerosol is a function of the reactant's

solubility. Therefore, flat surfaces are a poor proxy for the chemistry of small sub-micrometre sized particles.

2.5.2 Flow Tubes

Flow tubes are often employed for the study of gas-phase chemistry;[99;100] however, for the past decade they have commonly been used to study heterogeneous chemistry.[33;63;78;79] The flow tube walls are coated with the condensed phase of interest, while the reactive gas-phase molecule is added through a moveable injector. As the injector moves further from the detector, the time for reaction increases and the loss of the reactive species increases. This allows for the determination of a pseudo-first-order rate coefficient, k_s (s^{-1}), for the removal of the gas by the substrate of interest. The measured uptake coefficient, γ_{meas}, is given by

$$\gamma_{meas} = \frac{2rk_s}{u_{av}} \qquad \text{Eq2.40}$$

where r is the radius of the flow tube (m) and u_{av} is the mean thermal speed of the molecules (m s^{-1}). The greater surface area provided by a flow tube avoids the saturation effects found with Knudsen cells. However, the concern of relating γ_{meas} to aerosol particles, regarding the Kelvin Effect, still remains.

It is often difficult to uniformly coat the walls of the flow tube with the condensed phase, particularly for liquids. Rotating flow tubes (sometimes called coated-wall tubes) have been used for liquid-phase substrates to ensure an even coating over the entire flow tube surface. Often, however, the liquid is held in a rectangular container on the bottom of the flow tube. The principle of the experiment remains same in this case; however corrections must be made because only a portion of the surface area is reactive. The same approach can be used to study the heterogeneous reactions of solids.

To remove some of the uncertainty associated with coated-wall flow tubes, aerosols can be used in place of coating the flow tube wall. In these experiments the gas or the aerosols can be introduced via a moveable injector. This method, however, requires additional instrumentation to accurately acquire the size distribution and number density of the aerosol. From the size distribution, the available surface area for reaction can be determined. The surface area, or more accurately termed the surface area density, *S*, typically given in units of $\mu m^2/cm^3$, is used in place of the surface area of the flow tube. In this case, the net uptake coefficient is given by

$$\gamma_{meas} = \frac{4k_s}{Su_{av}} \qquad \text{Eq2.41}$$

Flow tube studies often require high oxidant levels to measure heterogeneous kinetics on short time scales. The short time scales (ranging from a few milliseconds to seconds) and high oxidant concentrations could be problematic for diffusion-limited reactions since particles may not be well mixed during such short reaction times.[101] Furthermore, secondary chemical reactions can take place within the particle itself[65;68;102] and depending on the oxidant concentrations can become competitive with the heterogeneous reaction rate.[70] This could lead to situations in which the reaction time and the oxidant concentration are not linearly related quantities. This may cause uncertainties in extrapolating the results of flow tube experiments to the real atmosphere where particles are exposed to much lower levels of oxidants for long timescales.

One way to overcome the high levels of oxidants typically employed in flow tube experiments is to use a relative rate approach.[88;103] In these experiments, a small amount of a tracer gas-phase molecule, X_{tracer}, is introduced along with the aerosols. The tracer species is often a molecule whose chemistry is very well known with the reactant of interest. In the case of OH chemistry, hexane[69;103] and hexanal[65] have been used. In these experiments, the heterogeneous rate coefficient, $k_{aerosol}$, is determined by

$$ln\frac{[X_{tracer}]_o}{[X_{tracer}]_t} = \frac{k_{tracer}}{k_{aerosol}} \cdot ln\frac{[X_{aerosol}]_o}{[X_{aerosol}]_t} \quad \text{Eq2.42}$$

where the concentration of the aerosol species is often determined by monitoring the intensity of a known mass peak by using an aerosol mass spectrometer.[65] This technique eliminates the need to determine the radical concentration or the reaction time. Consequently, radical concentrations can be closer to atmospheric values (e.g. ~10^9 molecules cm^{-3}).[65] However, the error associated with the gas-phase kinetics can often increase the error associated with the determined uptake coefficient. Furthermore, with relative rate kinetics the determined uptake coefficient can often be higher than one since the reactive species of interest (i.e. OH) is not directly measured.[65;67]

2.5.3 Aerosol Chambers

Aerosol chambers have recently been applied to studying aerosol kinetics and mechanisms.[68;102;104;105] The main advantages to these experiments are that they allow the use of longer reaction times (e.g. hours to days) and atmospherically relevant concentrations of radicals (e.g. ~10^6 molecules cm^{-3}).[104] These experiments typically use a relative rate approach in determining uptake coefficients and reaction rate coefficients. As a result they often have relatively large uncertainties and physically unrealistic uptake coefficients (e.g. > 1). These experiments do, however, allow researchers to monitor the change in aerosol composition over more atmospherically relevant timescales.[105] Aerosol chambers have also been used to monitor the change in composition under varying atmospheric conditions (e.g. variable relative humidity[102], varying NO_x conditions, atmospheric pressure, etc).

Table 2.2: Techniques employed in the determination of uptake coefficients.

Method	Advantages	Disadvantages
Knudsen Cell	- monitor change in uptake over time - directly measure reactive species of interest - relative ease of measurements - no correction for gas-phase diffusion	- saturation of surface by reactive species - re-evaporation into the gas-phase obscures true uptake - flat surfaces can be poor representative for curved surface of small particles
Coated Wall Flow Tube	- use of injector allows for easy change of time for reaction - directly measure reactive species of interest - easy measurement of fast reactions (e.g. radical chemistry) - no saturation of reactive surface	- difficult to ensure uniform coating - high level of oxidant required - short time scales - flat surfaces can be poor representative for curved surface of small particles - correction for diffusion required
Aerosol Flow Tube	- use of injector allows for easy change of time for reaction - directly measure reactive species of interest - easy measurement of fast reactions (e.g. radical chemistry) - can generate realistic size distributions - more accurate measurement of aerosol uptake coefficient	- additional instrumentation required to determine size distribution - high level of oxidant required - short time scales - minor correction for diffusion required - particles & gases may not be well mixed on short time-scales
Aerosol Chamber	- monitor change in uptake over time - monitor change in aerosol composition over time - atmospherically relevant gas-phase conditions - can generate realistic size distributions	- indirect measurement of radical species - increased error in measured uptake coefficient - uptake coefficients greater than 1.0
Relative Rate Approach	- no need to directly measure reactive species - more atmospherically relevant levels of radical species	- indirect measurement of radical species - measurement of aerosol species required - increased error in uptake coefficient - possibility for undetected processes - uptake coefficients greater than 1.0

2.6 Hydroxyl/Organic Kinetic Studies

As shown in Table 2.3, until recently most heterogeneous chemistry involving oxidation with OH has been performed almost exclusively in coated-wall flow tube reactors.[33;63;106;107] These experiments make use of high radical concentrations ($10^8 - 10^{10}$ molecules cm^{-3}) and short exposure times (milliseconds to seconds) to oxidize films or aerosols. The greatest challenge with flow tube studies is extrapolating the short-term, high-intensity oxidation observed during experimentation to the long-term, low-intensity oxidation more representative of the atmosphere. One significant advantage to flow tube studies, however, is that hydroxyl radicals can be measured directly allowing for a more accurate calculation of heterogeneous kinetics. One of the largest disadvantages to coated-wall flow tube studies is the diffusion limitation of the gas-phase reactive species to the reactive surface of interest. Since the gas-phase species are often introduced in the centre of the flow tube, the reaction of interest does not truly begin until this molecule diffuses to the wall of the flow tube. Therefore a correction is required to account for this diffusional process. If the experimental results are not properly corrected then only a lower limit to the uptake coefficient can be determined.[108]

Chamber studies provide an alternative method to flow tube techniques.[67;71;102;104] While chamber studies can provide the long-term, low-intensity oxidation more representative of the atmosphere, measurement of OH is typically done indirectly via monitoring the decay of two gas-phase tracer species. The limitation to this relative rate approach is that the tracer species must have well known kinetics with OH and not react with any other species. However, secondary chemistry, particularly with OH, can result in relatively large errors in the measured uptake coefficient, or uptake coefficients greater than unity.[65;67;71] Lambe et al. (2009)[71] found uptake coefficients as large as nine for some components of motor oil aerosols and as large as 40 for

diesel aerosols. Flow tube studies can also be performed using relative rate approaches, however, these studies also often result in unrealistic uptake coefficients, $\gamma > 1$.[65]

Since the production and detection of hydroxyl radicals can be quite difficult, a new approach being used to measure the uptake coefficient is to monitor the loss of the particle species. This is done using an aerosol mass spectrometer (AMS) and monitoring the loss of the parent ion peak of the particle material, or another peak with similar decay kinetics. For example, George et al. (2007)[66] measured the uptake of OH on bis(2-ethylhexyl) sebacate ($C_{26}H_{50}O_4$, BES) particles using an aerosol flow tube technique. To determine an uptake coefficient, they monitored the decay of the m/z 297 fragment as a proxy for the loss of particle-phase BES. This approach resulted in an uptake coefficient with a significant amount of error, $\gamma = 1.3 \pm 0.4$, suggesting a potential γ value larger than unity. The problem with this method is that it doesn't take into account any secondary chemistry that may occur with BES after it has reacted with OH. This can be significant if the secondary condensed-phase chemistry is an important loss mechanism for condensed-phase species. Any additional chemistry that removes BES from the particle would be interpreted as reaction with OH and can skew the determined uptake coefficient to larger values. Therefore, studies that measure the loss of the particle species could be reporting erroneously large uptake coefficients.

Given the potential importance of these reactions it is vital that they are understood. In order for these reactions to be well understood they need to be properly and accurately studied. It was therefore determined that the increased accuracy of an aerosol flow tube system made it the most reliable approach for the study of hydroxyl radical uptake on micron-sized aerosols. The details of the flow tube technique will be outlined in the following chapter.

Table 2.3: Summary of OH Heterogeneous Studies with Atmospherically Relevant Surfaces.

Authors	Surface	Technique	Surface Type	γ
Lambe et al. (2009)[71]	motor oil	smog chamber, relative rate approach	aerosol	3.5 ± 0.7
	diesel fuel/motor oil		aerosol	13 – 40
Che et al. (2009)[70]	squalene	continuous flow stirred tank reactor	aerosol	0.51 ± 0.1
Smith et al. (2009)[69]	squalene	aerosol flow tube	aerosol	0.3 ± 0.07
Bagot et al. (2008)[64]	squalene	vacuum chamber	liquid surface	0.49 ± 0.04
McNeill et al. (2008)[68]	palmitic acid	aerosol flow tube	pure aerosol	0.8 - 1
			aqueous aerosols	0.05 ± 0.01
			crystalline NaCl	0.3 +0.1/-0.05
George et al. (2007)[66]	bis(2-ethylhexyl) sebacate	aerosol flow tube	aerosol	1.3 ± 0.4
Lambe et al. (2007)[67]	n-hexacosane	smog chamber, relative rate approach	aerosol	1.04 ± 0.21
Hearn & Smith (2006)[65]	methyl oleate	flow tube, relative rate approach	aerosol	1.12 ± 0.36
	bis(2-ethylhexyl) sebacate		aerosol	2
Laskin et al. (2006)[109]	sodium chloride	flow tube	aqueous aerosols	>0.1
Molina et al. (2004)[33]	octadecyltrichlorosilane	coated-wall flow tube	film	>0.2
	paraffin wax		film	>0.2
	pyrene wax		film	>0.2
Bertram et al. (2001)[63]	paraffin wax	coated-wall flow tube	solid surface	0.34
	stearic-palmitic acid		solid surface	0.32
	soot		solid surface	0.88
	pyrene		solid surface	0.32
	halocarbon wax		solid surface	0.0006
Takami et al. (1998)[84]	water (pH = 5.6)	impinging flow	film	0.0042 ± 0.0028
Cooper & Abbatt (1996)[107]	water ice	coated-wall flow tube	solid surface	0.03 ± 0.02
	NH_4HSO_4		solid surface	<0.03
	$(NH_4)_2SO_4$		solid surface	<0.03
Hanson et al. (1992)[106]	pure water	coated-wall flow tube	film	0.0035
	28% w/w sulphuric acid		film	>0.08
Jech et al. (1982)[110]	malonic acid	aerosol flow tube	aerosol	0.17 ± 0.034
	$(NH_4)_2SO_4$		dry aerosol	0.0089 ± 0.0018

2.7 Summary

After considering the advantages and disadvantages of the various methods listed above it was determined that the best way to measure uptake coefficients of OH on aerosol particles was to use a flow tube approach. Despite their disadvantages - mainly the need for high radical concentrations - flow tubes allow for a more accurate determination of uptake coefficients than the other methods listed. The ability to directly measure OH during the experiments removes much of the uncertainty associated with chamber studies. Generating atmospherically relevant size distributions limit saturation effects and accounts for the Kelvin Effect, which allows for a more accurate determination of the uptake coefficient. Combined with a simple technique for the determination of aerosol size and composition, an aerosol flow tube system was also deemed to be the most feasible and cost efficient. The full details of the experimental setup are described in the following chapter.

Chapter 3
Experimental Approach

3.1 Flow Tube Conditions

3.1.1 Flow Conditions

Flow conditions are critical for flow tube studies, and are often the determining factor when considering design. A standard flow tube design is shown in Figure 3.1.[111] Flow tubes are usually made out of Pyrex tubing with an internal diameter of about 2.2 cm and can vary in length from a few tens of centimetres to a hundred centimetres. The typical operational idea behind the discharge flow technique is based on the relation between reaction time and reactant concentration. The reaction starts at point *a* and ends at the point of detection, point *b*. The time of reaction can be calculated if the velocity of gas mixture in the flow tube is known and can be varied by changing the distance between points *a* and *b*, via a moveable injector.

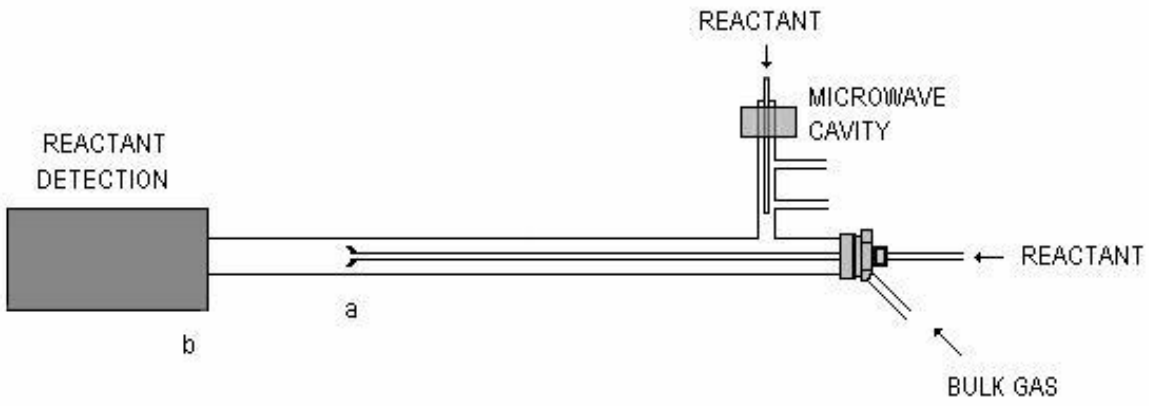

Figure 3.1: Schematic design of a typical flow tube system. *a* is the point at which reactants mix and reaction begins, and *b* is the end point for reaction, where reactants are detected.

Flow within the flow tube is described by the Reynolds number, Re, and is expressed by Eq3.1:

$$\mathrm{Re} = \frac{2a\rho\bar{v}}{\mu} \qquad \text{Eq3.1}$$

where a is the internal diameter of the flow tube (m), $\bar{v}$ is the average velocity of the carrier gas (m s^{-1}), ρ is the density of the carrier gas (kg m^{-3}) and μ is the viscosity of the carrier gas (kg m^{-1} s^{-1}). For low values of Re, the viscosity dissipation dominates creating laminar flow. For large Reynolds numbers, viscous forces are unable to overcome inertial forces and the largest scales of fluid motion are undamped, resulting in turbulent flow. Empirically it has been found that laminar flow is generally stable at Re < 2000 and that turbulent flow is stable at Re > 3000. In gas-phase kinetic experiments, turbulent flow is typically employed to ensure proper mixing of all reactants.[99;112;113] With aerosol studies, however, the size distribution of the aerosol must remain constant after characterization, which is difficult with turbulent flows due to coagulation and growth.

Flow rates in the system were kept such that the overall conditions fell within the laminar regime. Laminar flow is important for limiting coagulation and growth of the aerosols. Coagulation and growth would generate new surfaces for heterogeneous chemistry at rates that are faster than observed in the atmosphere. Coagulation of particles may bring fresh material to the surface of the particle on shorter time scales than simple internal mixing of a single particle. This would cause an upward bias in the calculation of the uptake coefficient. Deposition of aerosol material to the walls of the flow tube under turbulent flow conditions over the course of an experiment could act as a secondary reactive site enhancing uptake. Enhanced loss of the reactive species to the flow tube walls can also occur under turbulent flow. Both of these phenomena could result in an inconsistent loss of OH under similar experimental conditions; thereby make interpretation of the resulting data difficult. Turbulent flow could also cause recirculation into the optical cell or an uneven distribution of particles across the flow tube. This

would skew the detected surface area, resulting in an improper calculation of the uptake coefficient. Furthermore, detection of the aerosols (discussed below) assumes single scattering by the aerosol flow. Turbulent flow will mix the aerosols in a non-uniform fashion, increasing the likelihood of multiple scattering, thereby making it harder to accurately detect and quantify the aerosols.

While turbulent flow ensures proper mixing of all reactants, diffusion limitations can be present in laminar flow studies. Radial concentration gradients can develop between points *a* and *b* and represent the major limiting factor for the use of laminar flow systems, particularly for coated-wall flow techniques. This results in a needed correction for diffusion to the calculated uptake coefficient[108], as discussed in the previous chapter.

Computational Fluid Dynamics (CFD) modelling was carried out on various aspects of the system to ensure optimal design. The calculations were performed using the commercially available ANSYS CFX program (ANSYS, Inc). This modelling was conducted to ensure that all flows fell within the laminar region and that none of the inlets created turbulence within the system. The CFD simulations used for this purpose have been previously tested under more severe conditions than those of the present experiments[114;115] and the results were found to be accurate when compared with measurements of the simulated quantities.

3.1.2 Pressure

The experiments conducted in this project were carried out in a low pressure kinetic flow tube. Pumping of the flow tube was done with a mechanical rotary pump (E2M80; BOC Edwards), enhanced with a blower (EH-250; BOC Edwards), through a butterfly valve to maintain low pressures. Low pressure conditions (~35-40 Torr) were necessary for three reasons. The first, and the most important, reason was to prevent gas-phase diffusion from limiting the very fast OH uptake. By eliminating diffusion as a possible limiting step in the uptake of OH, the reaction

between OH and the surface of the aerosols can be more accurately studied. As can be seen from Eq2.7, the conductance of OH to the particle surface is proportional to the gas-phase diffusion coefficient, D_g, which in turn is inversely proportional to pressure. Therefore, as pressure decreases the ability of OH to conduct itself to the surface of the particle increases. This results in a lowered resistance, $1/\Gamma_{diff}$, as described by Eq2.7. Table 3.1 shows how the conductivity, and resistance, of OH diffusion in helium changes with pressure.

Table 3.1: Effect of pressure on diffusion of OH.

Pressure (Torr)	$D_{OH\text{-}He}$ **(m^2/s)**	Γ_{diff}	$1/\Gamma_{diff}$
1	0.0636	931.17	0.00107
4	0.0159	232.79	0.00430
10	0.00636	93.12	0.01074
40	0.00159	23.28	0.04296

As $1/\Gamma_{diff}$ decreases with decreasing pressure, its importance to the overall uptake process diminishes. Therefore, at low pressures, uptake was considered not to be limited by gas-phase diffusion, and only a small correction to the measured uptake, γ_{meas}, was needed.

Second, due to the reactive nature of OH, it is necessary to ensure that not all of the OH reacted before it could be detected. Therefore, under low pressure conditions the contact time of OH with the aerosols was on the order of milliseconds. This allowed for a detectable OH signal while still allowing enough time for reaction with the aerosol surface. Third, to maximize operating conditions for the mass spectrometer (used in detection of OH) pressures on the order of 10 Torr were required. At higher pressures in the flow tube, low pressures in the mass spectrometer could not be achieved resulting in poor detection limits. One important factor to keep in mind when selecting the operating pressure for the flow tube is that the vapour pressure of bulk liquid water is 23.8 Torr at a temperature of 298 K[116]; therefore, if aqueous aerosols are to

be studied, the operating pressure within the flow tube must be greater than 23.8 Torr to prevent evaporation of aerosol particles.

3.1.3 Temperature

Temperature within the flow tube is a critical parameter to measure and control. If the temperature within the tube is not that at which the reactions are assumed to take place then the calculated uptake will be incorrect. To this end, thermocouples were placed on the outside of the flow tube wall to measure the temperature of the laboratory at the flow tube wall. This provided a temperature measurement with an accuracy of 0.1°C. The temperature at the flow tube wall was approximately constant at 22 – 23°C. Thermal conductivity was assumed to be fast, even for these low pressures and relatively high flows. This was confirmed by placing a thermocouple in the midst of the gas flow and observing a temperature of 22 – 23°C. Therefore, all reactions were assumed to occur at room temperature (22.5°C).

3.2 Aerosol Composition

As mentioned in Chapter 1, a wide range of aerosols can be found consisting of organic molecules or coated with organic compounds.[14-20;22] Tor this reason, the focus of this project was to measure the uptake of OH radicals on the surface of pure aqueous and organic aerosols, and aqueous aerosols coated with organic monolayers. Oleic acid ($C_{18}H_{34}O_2$) was chosen as the organic of interest on the basis of its abundance within marine and continental aerosols.[15-18;22] The unsaturated character of oleic acid may provide the opportunity to study the location of the OH/organic reaction on the aerosol surface. Stearic acid ($C_{18}H_{36}O_2$) is also a common organic in aerosols[15-18;22] and comparison of uptake between stearic and oleic acid may provide further insight into the reactive nature of the double bond and the importance of OH addition or H abstraction in the uptake kinetics.

3.3 Aerosol Generation

3.3.1 Instrumentation

Three instruments were tested for the generation of aerosols to determine the optimal approach for creating aerosols at low pressure and the flow conditions required. The first instrument tested was an ultrasonic nebulizer (099HD, Ultra-Neb 99; DeVilbiss Co.). When a high frequency (1.63 MHz) electrical signal is applied to a piezoelectric transducer, located at the bottom of a reservoir bottle, it oscillates at the frequency of the applied voltage (Figure 3.2a). The resulting energy is transferred to the surrounding liquid, inducing cavitation in the surface layer (Figure 3.2b). The droplets formed above the solution surface are transferred to the flow tube in a stream of dry nitrogen that passes through the headspace of the reservoir bottle. Particles produced by the nebulizer typically fall in the 0.5 – 5 μm diameter range, while the number density output (# of particles cm^{-3}) of the aerosol can be adjusted by varying the amplitude of the applied signal.[117] This nebulizer was typically used with aqueous solutions for the generation of aqueous aerosols. The viscosities of the organics of interest, however, are much higher than that of water. As a result, the transfer of energy from the oscillating transducer to the organic liquid was insufficient to create cavitation at the liquid's surface. Therefore, this nebulizer was unable to generate pure organic aerosols.

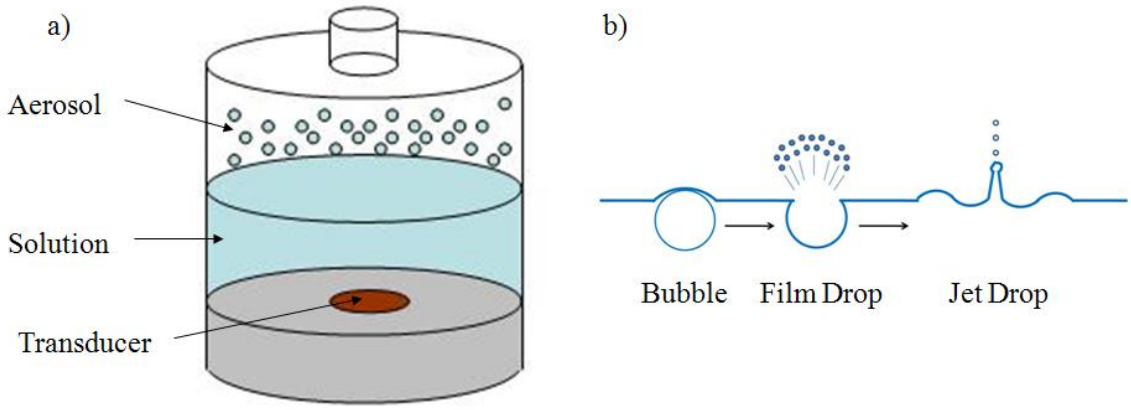

Figure 3.2: a) Schematic of Ultra-Neb nebulizer. b) Cavitation process at solution surface.

The second instrument tested for the generation of aerosols was a commercial constant output atomizer (TSI 3076; TSI Inc.). The atomizer was used as a conventional recirculation atomizer generating submicron aerosols from most solutions or suspensions. The number median diameter of the droplets generated by the atomizer is quoted as 0.3 μm for water, with a geometric standard deviation less than 2.0.[118] The generation of aerosols works on the principal of the Venturi Effect. Referencing Figure 3.3, compressed air is forced through a small orifice (340 μm), as it passes out the other side it expands and increases velocity. According to the Bernoulli principle, this produces a low pressure region immediately after the pinhole. The solution is drawn through a narrow passage into the atomizing section by the resulting pressure gradient formed between the region after the pinhole and the headspace above the liquid in an attached reservoir bottle. An aerosol is formed when the solution is atomized by the high velocity jet. Large droplets are removed by impaction on the wall opposite the jet and excess liquid is drained at the bottom of the atomizer back into the sample bottle. Smaller aqueous droplets will evaporate due to the increased saturation vapour pressure over a curved surface compared to that of a flat surface (the Kelvin Effect).[5;6] This effect is significant for small aqueous droplets in the sub-micrometre size range, but less important for organic particles with much lower vapour

pressures. This produces a fine spray exiting through the top of the atomizer. The air flow rate during operation is 3.0 – 3.5 STP L min^{-1} at 35 psig, resulting in a liquid flow rate of 20 cm^3 min^{-1}.[118] Aerosol production rate is quoted as $2x10^6$ particles cm^{-3} under nominal conditions.[118] When the pressure of the compressed gas flow is constant, the output of the atomizer is extremely stable.

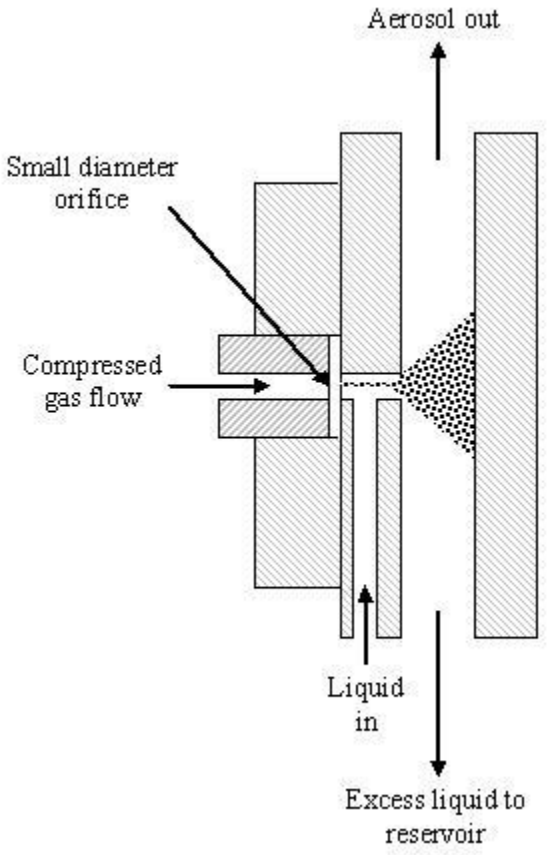

Figure 3.3: Schematic cross-section of constant output atomizer.

The final instrument available for the generation of aerosols was a commercial nebulizer (PEEK Mira Mist; Burgener Research Inc.). The nebulizer works on the basic principle that any body of liquid can be used to produce a fine mist with a gas stream, if they are in close proximity to each other. Gas streams in capillaries have velocity gradients across the diameter of the capillary, with the slowest gas moving at the edges of the capillary and the fastest at the center.

The central gas flow is three to ten times as fast as the gas flow at the edge of the stream. Liquid is introduced via a spout to the centre of the gas stream, where the gas can impact the liquid with much more energy (Figure 3.4[119]). Energy is related to the square of the velocity, so three to ten times the speed is 9 to 100 times the energy. With such an increase in energy transfer from the gas to the liquid, the liquid is broken up into much smaller droplets. This produces a mist with average droplet sizes much smaller than any other method for the same gas flow and pressures.[119] The Burgener Mira Mist nebulizers require 45 – 55 PSI for a 1 STP L min^{-1} flow of carrier gas.

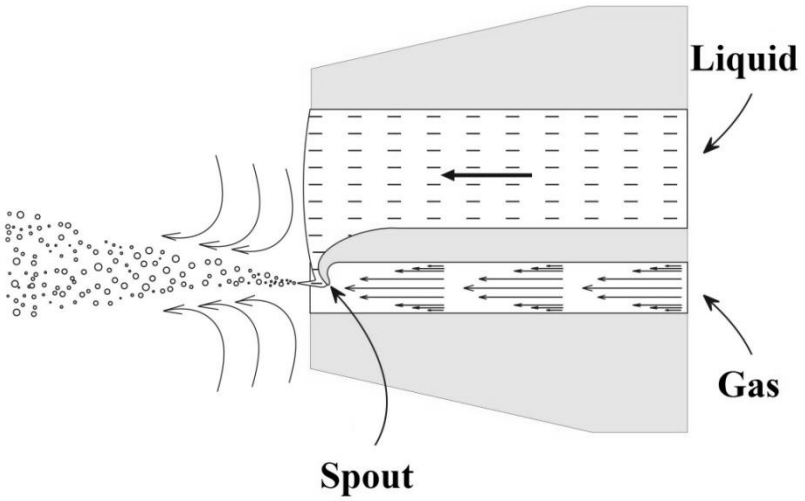

Figure 3.4: Schematic cross-section of Mira-Mist nebulizer.

Despite the presence of a fast flowing gas, the Mira Mist nebulizer does not take advantage of the Venturi effect to generate aerosols. Therefore, a pump was required to supply the sample solution to the gas stream. The pump speed and the quality of the pump tubing have a large effect on the stability of the nebulizer. The pump used to supply the Mira Mist nebulizer with solution was a peristaltic pump designed for low flow (P720; Instech Laboratoris, Inc). These pumps allowed for a range of low flow rates (0.0133 to 0.35 mL min^{-1}) to be used in introducing the sample solutions to the nebulizer. This provided a good system of control over

the aerosol number density produced by the nebulizer, and consequently allowed the operator to control the surface area used in the uptake kinetic experiments.

3.3.2 Multi-Component Aerosols

Tests were conducted using a second Mira Mist nebulizer (Mira Mist CE; Burgener Research Inc.), which has an added capillary that allowed for the introduction of two solutions into the gas stream. The capillary is located in the centre of the main solution channel, as indicated in Figure 3.5.[119] This allows a second solution to mix with the first solution just prior to atomization by the gas stream. Therefore, using two peristaltic pumps, aerosols can be created that are composed of two components. Aerosols consisting of an organic compound and water were generated in an attempt to create water particles coated with organic material. Water was introduced in the centre capillary (Solution 1), while the organic was introduced along the main solution channel (Solution 2). It was theorized that this would be the best approach to generating water particles with a coating of organic material. The multi-component nebulizer operates under the same principle, and flow conditions, as the nebulizer discussed in Section 3.3.1.

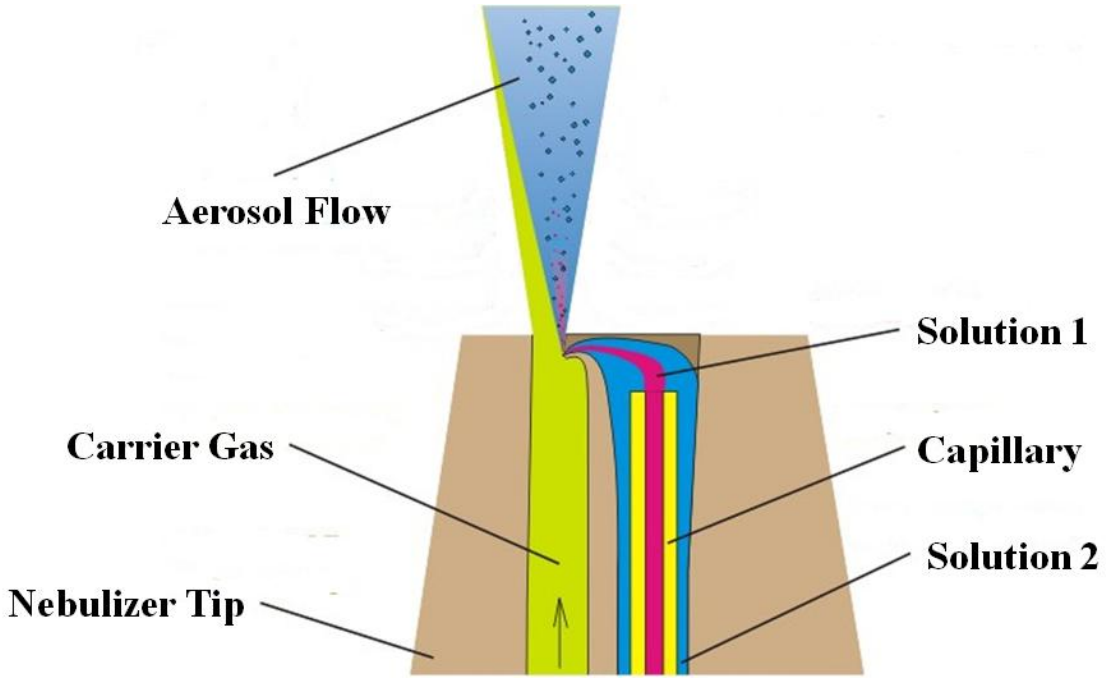

Figure 3.5: Schematic of Mira Mist CE nebulizer designed for multi-component flow.

3.3.3 Aerosol Detection

Aerosol quantification and properties are measured by Fourier Transform infrared spectroscopy (FTIR). Broadly speaking, infrared (IR) radiation is the part of the electromagnetic spectrum that lies between the visible and the microwave regions. Of greater practical purpose to organic chemists is the portion that lies between 4000 and 400 cm^{-1}. IR radiation in this range is absorbed and converted to vibrational energy by a molecule. These vibrational energies are characteristic for a given molecule, which allows for identification of the molecule from reference samples or libraries. FTIR spectroscopy is a powerful tool for determining structure and make-up of specific molecules. This capacity to differentiate between molecules is sometimes referred to as its fingerprinting ability.

An IR spectrum, between 750 – 5000 cm^{-1}, was obtained for a given aerosol sample travelling through the flow tube by an FTIR spectrometer (Tensor 37; Bruker Optics Inc.). The collimated IR beam from the spectrometer, modulated by a Michelson interferometer, intersected

the flowing aerosols in an optical cell. KRS-5 (thallium bromide-iodide) windows, which are invisible to IR wavelengths, were used to seal the optical cell. The windows were secured with o-rings to ensure vacuum was maintained inside the optical cell. The attenuated IR beam was then transferred to a nitrogen-purged aluminum detector box. The nitrogen purge ensured that the resulting spectra did not contain absorption features of ambient gases such as CO_2 and H_2O. The detector box was isolated from its surroundings by a foam base, which minimized electrical interference. In the detector box, the IR beam was focussed by an off-axis parabolic mirror onto the active area of a photoconductive mercury cadmium telluride (MCT) detector (FTIR-22-1.0; Infrared Associates, Inc.). During operation, the MCT detector was cooled with liquid nitrogen to reduce thermal noise. The detected interferogram was amplified and sent back to the spectrometer, where it was then digitized and converted into a spectrum.

Spectra were recorded on a PC, which was interfaced to the spectrometer using Ethernet cable, using the Bruker OPUS program. Each spectrum was an average of 40 scans, collected at 4 cm^{-1} resolution and 20 kHz metrology frequency. Background spectra were obtained prior to aerosol introduction for a given set of experimental conditions. Background samples were again taken after the uptake experiments to determine if any drift of the baseline occurred during sampling.

3.3.4 Aerosol Characterization

The extinction spectrum generated by the aerosol contained the absorption of gas-phase molecules and bulk-phase (aerosol) molecules, as well as the scattering due to the aerosols. Removal of gas-phase absorption revealed the extinction spectrum of the aerosol sample. This extinction spectrum was dependent on both the size of the aerosols and the chemical composition of the aerosols. Therefore, using Mie theory to calculate reference spectra of monodisperse aerosols[120] of known size and composition over a range of sizes of interest (0.05 to 18 μm), the

experimental spectrum was compared to the calculated spectra. Figure 3.6 illustrates a few sample spectra for different monodisperse aerosols of oleic acid, which were calculated using Mie theory. Optical constants used in the calculation of oleic acid reference spectra were obtained from McGinty et al. (2009).[121] Optical constants for stearic acid, however, are currently unavailable. Therefore, organic aerosol studies focused on oleic acid.

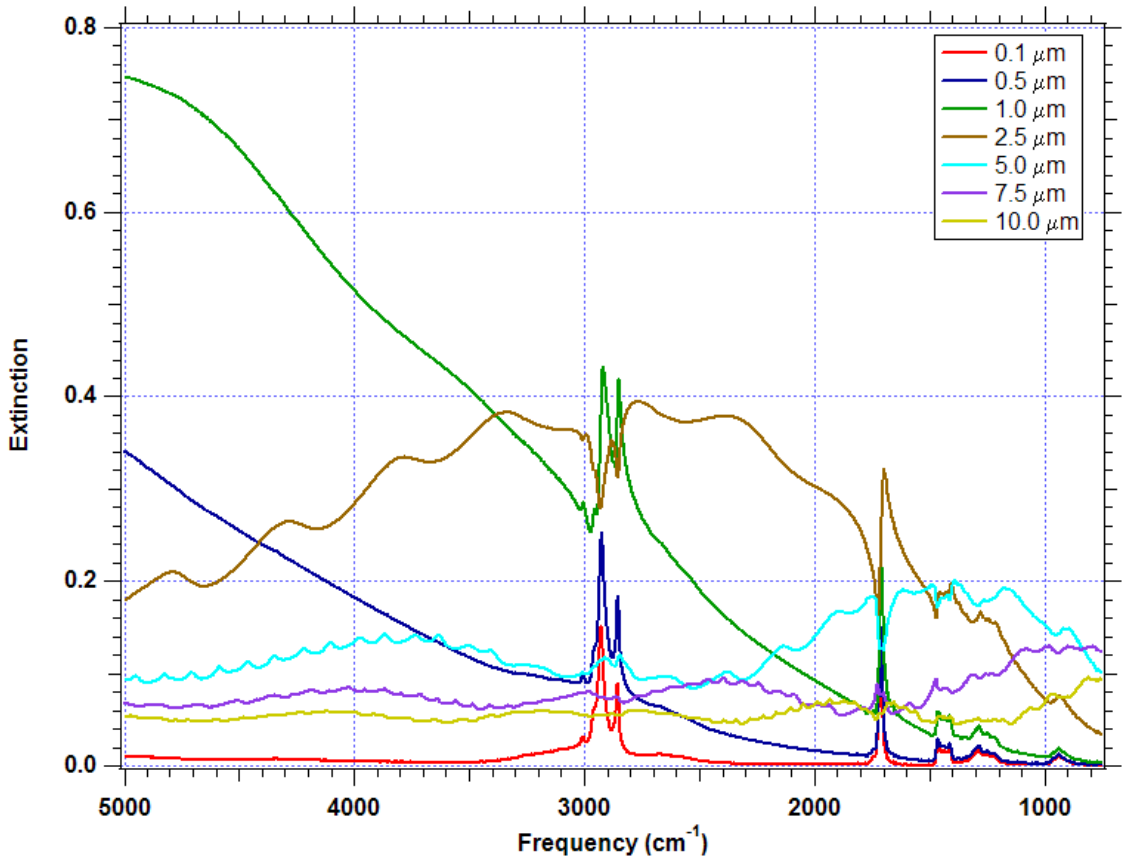

Figure 3.6: Sample of calculated Basis Set Spectra of Oleic Acid.

The aerosol extinction spectrum was analysed using methods developed by researchers at the Waterloo Centre for Atmospheric Sciences. These methods were successfully applied to satellite data for the determination of size distributions, particle number densities, phases, and composition of stratospheric aerosols.[122-124] This procedure uses a linear least-squares method to determine the contribution of each monodisperse reference spectrum that is required to reproduce

the experimental spectrum. The method is mathematically simple and involves basic matrix calculations. Spectra of monodisperse aerosols for a specific composition (k^c_i) are compared to the experimental extinction spectrum (M) via matrix multiplication (Figure 3.7). In the equation, $P_c(r)$ is an unknown vector that contains the contribution to M from each known spectrum (k^c_i). This vector $P_c(r)$ is then the size distribution (or volume distribution) of the experimental spectrum.

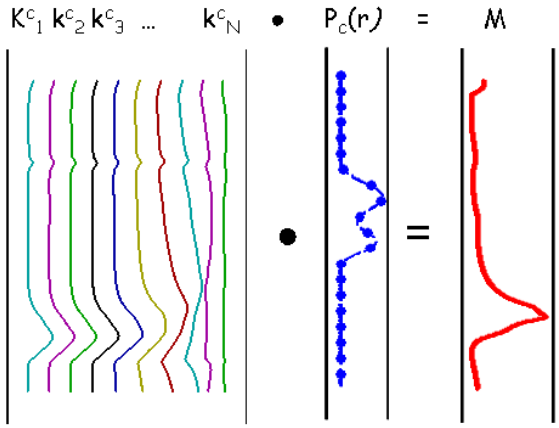

Figure 3.7: Matrix multiplication of sample spectrum.

Zasetsky et al. (2007)[124] also created a similar fitting procedure that assumes the particles are coated with a material that is optically different from the core particle. This version of the program uses basis set spectra that are generated for a range of core sizes that have varying coating thicknesses.[120] Zasetsky et al. tested the program with silica particles of known size that were coated with adsorbed water and were able to show that if an *a prior* estimate of the core size can be made then retrieval of the coating thickness is straightforward.

The procedure solves the following least-squares minimization problem[123]

$$\chi = min\{|\mathrm{k}\cdot \mathrm{P} - \mathrm{M} + \gamma \cdot S \cdot \mathrm{P}|^2\}^{1/2} \qquad \text{Eq3.2}$$

where k is the F x N matrix consisting of the basis set spectra, with F the number of frequencies for which extinction is calculated and N the number of radii (96). This is multiplied by the N x 1

solution vector, P, to give a calculated extinction spectrum. The procedure iteratively varies the value of P to minimize the sum of the squares of the differences between the calculated and experimental spectra ($k \cdot P - M$). The "goodness of fit" between the calculated and experimental spectra is indicated by the value of χ. The solution vector corresponding to the minimum value of χ is output.

The term $\gamma \cdot S \cdot P$ is a smoothing constraint introduced to ensure that the retrieved size distribution (P) does not have unphysical sharp features. Note that the parameter γ in Eq3.2 is not related to the uptake coefficient, γ, outlined in Chapter 2 but rather it is a smoothing parameter. If the experimental spectrum is noisy, it is possible for the retrieval to satisfy the goodness of fit criterion (*i.e.* find a local minimum) by assigning very high and very low weights to adjacent radii, producing an unphysical "jagged" size distribution in which nearly identical radii have very different populations. This unphysical result is prevented by the use of the matrix *S*, which minimizes the third differences of vector P and in turn its jaggedness. The extent of this minimization is controlled by the parameter γ.

In practice, it is found that the goodness of fit parameter, χ, remains low and relatively constant as γ ranges from zero (no smoothing) to some particular value, which depends on the noise in the experimental spectrum. As γ is increased beyond this particular value, χ begins to increase sharply (*i.e.* the goodness of fit deteriorates rapidly). Thus the point at which χ begins to rise is the most smoothing that can be applied without adversely affecting the agreement between the calculated and experimental spectra ($\chi_\gamma \approx \chi_{min}$). This brings up the question of the uniqueness of the solution vector, P. A criterion is required to select the best value of γ within the range from zero to the point where χ begins to increase. Zasetsky et al. (2004)[123] showed that the best value of γ can be selected by maximizing the configurational entropy of the ensemble of particles. (This approach assumes that the size distribution is in thermodynamic equilibrium.) They found

that the maximum in the configurational entropy coincides with the point where χ begins to rise sharply with increasing γ and concluded that this is the correct size distribution.

The top panel of Figure 3.8 shows that at $\gamma = 0.1$ the value of χ begins to increase dramatically. This increase in χ at a γ value of 0.1 was consistent for a variety of oleic acid distributions generated under different conditions. For the size distributions used in these experiments, the change in χ was less than 2 – 3% for a γ value of 0.1, and significantly larger for γ values larger than 0.1. The size distribution corresponding to $\gamma = 0.1$ was then used in the quantification of the total aerosol surface area. The bottom plot in Figure 3.8 demonstrates how a jagged distribution ($\gamma = 0$) of an experimental aerosol becomes significantly smoother as γ increases, even for γ values as small as 0.01. Figure 3.8 also shows that the essential information – the modal structure of the distribution – is not removed by constraining the smoothness of the fit even for moderately large values of γ.

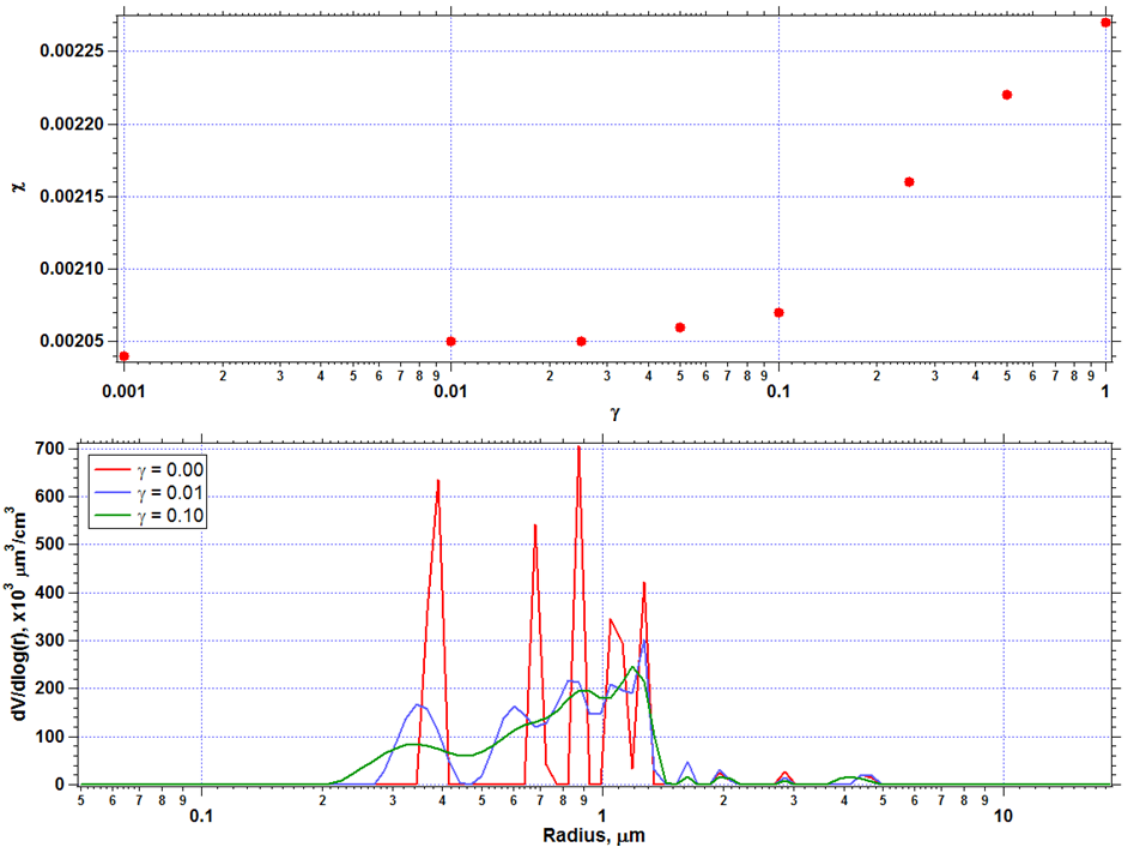

Figure 3.8: Top panel, χ as a function of γ. Bottom panel shows volume density distributions corresponding to increasing γ.

Since the analysis of the uptake experiments required the total surface area density, it was important to note how it changed with increasing values of γ. Figure 3.9 demonstrates how the total surface area density changed as γ increased for the γ values shown in Figure 3.8. It was seen that the point at which χ rose sharply also corresponded to a maximum deviation from the total surface area density calculated for the jagged distribution ($\gamma = 0$) and typically ranged between 2 – 5%. Therefore, the error associated with the total retrieved surface area density was assumed to be ±5%.

Other examples of the output from the aerosol quantification program are given in Figure 3.10 for pure water and pure oleic acid aerosols.

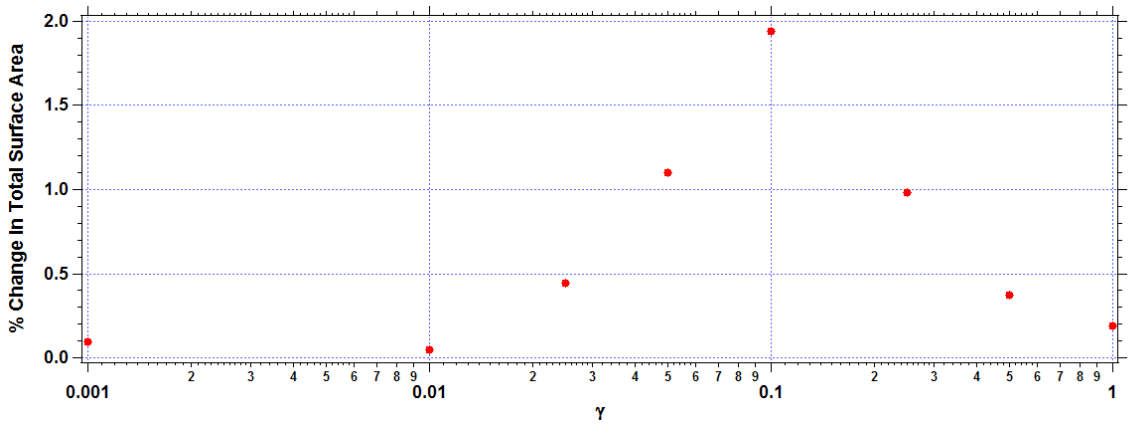

Figure 3.9: Effect of smoothing parameter γ on total surface area retrieved from fit.

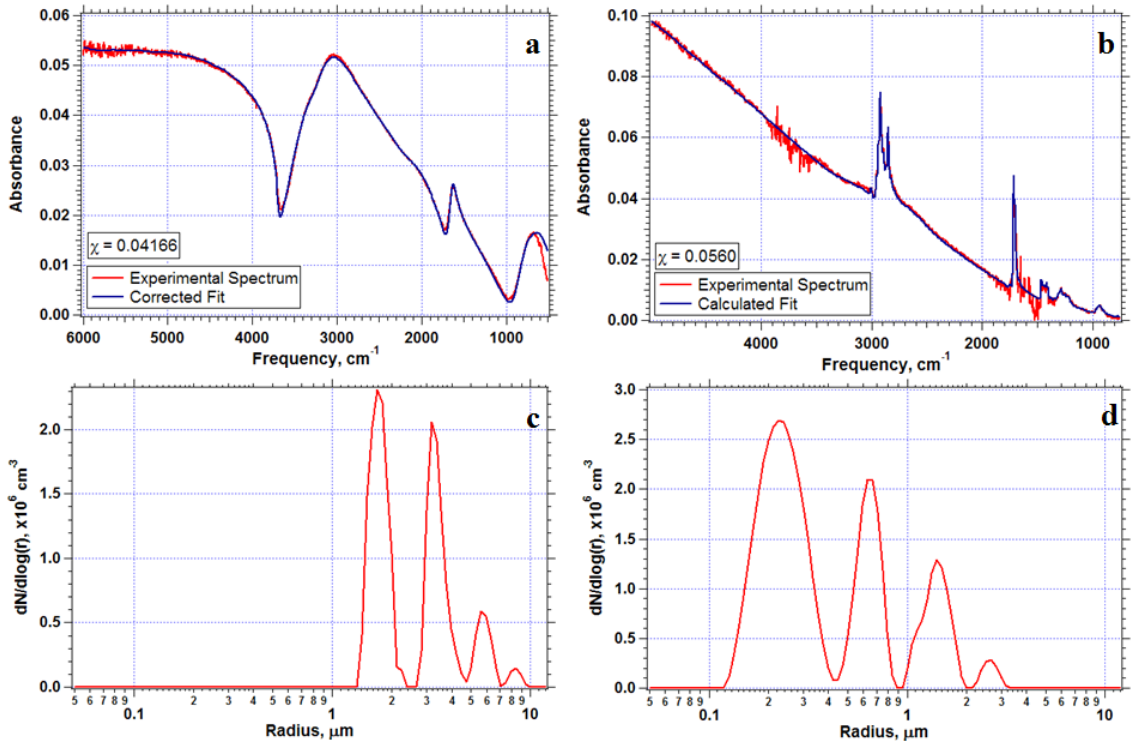

Figure 3.10: Spectra of single-component aerosols, corresponding calculated fits and volume density distributions: a) water, b) oleic acid, c) water number density distribution and d) oleic acid number density distribution.

The characterization of a multi-component aerosol is more complicated than for a single component system. This is due to the variety of ways in which a multi-component aerosol can be

generated. The simplest form of a multi-component aerosol is an externally mixed aerosol, which consists of individual particles composed of different material (e.g. an aerosol comprised of separate water and oleic acid particles).[5;6] However, an aerosol can also consist of internally mixed particles. These are particles that have the same composition corresponding to a mixture of multiple components (e.g. water particles with inclusions of oleic acid).[5;6] The composition of these internally mixed particles can become quite complex depending on the solubility of the various components. For example, organic components found in aqueous particles may not form a simple solution if the organics are very hydrophobic. Instead, these organics are expected to form an inverted micelle structure creating an organic coating on the surface of the aqueous particle.[17;28;125]

This made characterizing these particles difficult, since there was no *a priori* estimate of the expected structure of the mixed particles. When basis set spectra for multiple components that are miscible with each other are used in the fitting procedure described above it is assumed that an internal mixture is created. This is confirmed by the fact that in these cases the multiple components appear at similar sizes in the size distribution.[122] For immiscible solutions, however, no clear assumption of this manner can be made. Therefore, all possible mixtures must be assumed possible and the spectra must be fitted with all potential mixtures.

Take the multi-component mixture shown in Figure 3.11that consists of oleic acid and water. This aerosol was generated using the Mira Mist CE nebulizer. The extinction spectrum clearly shows the general shape associated with a water aerosol (Figure 3.10a); however, there are clear absorption features from oleic acid seen at 2800 – 2900 cm^{-1} and approximately 1700 cm^{-1}. It was evident then that this spectrum was generated by a multi-component aerosol. The difficulty then became determining which kind of aerosol mixture the spectrum represented.

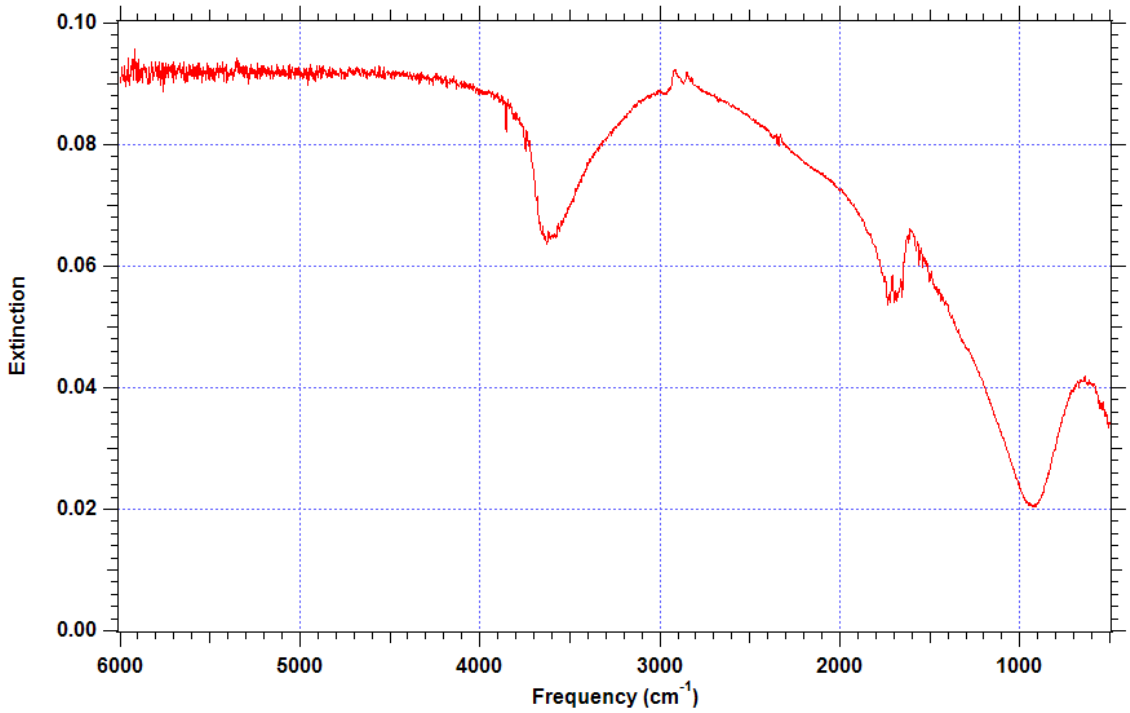

Figure 3.11: Extinction spectrum of multi-component aerosol consisting of oleic acid and water generated using the Mira Mist CE nebulizer.

Running the fitting procedure with both oleic acid and water optical constants resulted in a calculated fit to the experimental spectrum, as shown in Figure 3.12. Figure 3.13 shows the corresponding number density (Figure 3.13a) and volume density (Figure 3.13b) distributions. According to these distributions, the aerosol produced by the nebulizer could be an internal and external mixture of particles. It appears that the aerosol may consist of submicron sized organic particles with radii of approximately 0.15 and 0.8 μm, as well as micron sized aqueous particles consisting of inclusions of oleic acid.

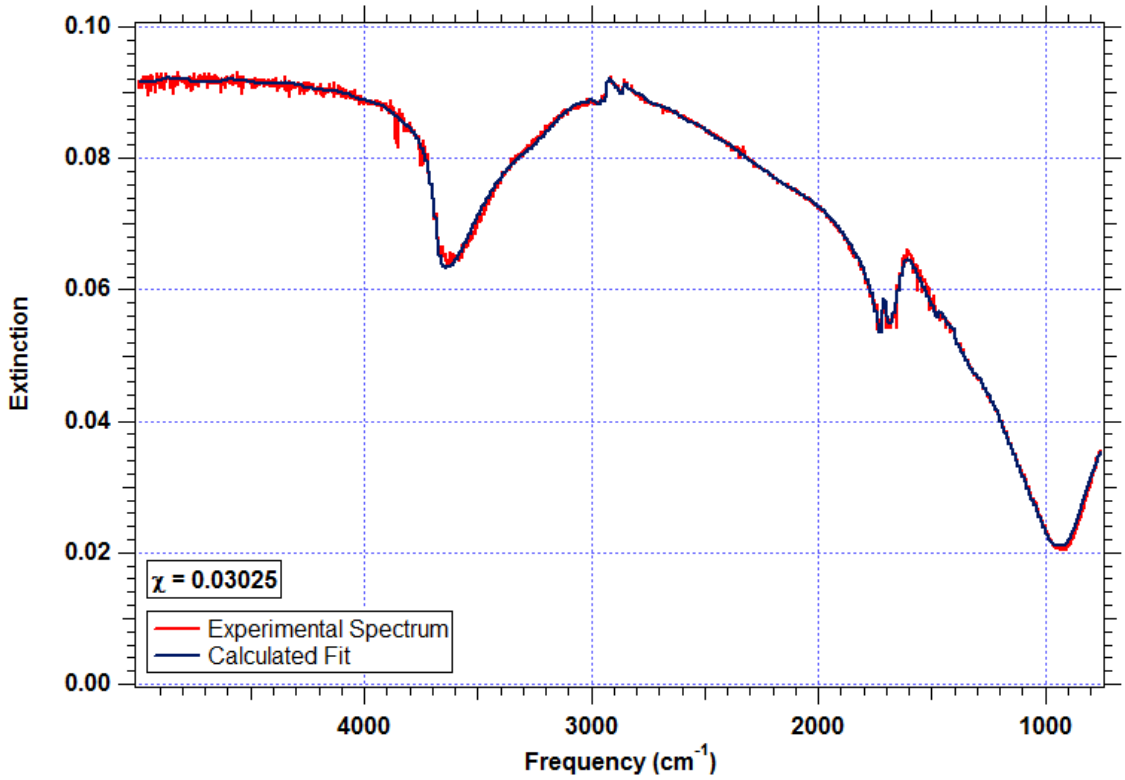

Figure 3.12: Mie fit of multi-component aerosol using basis set spectra for water and oleic acid.

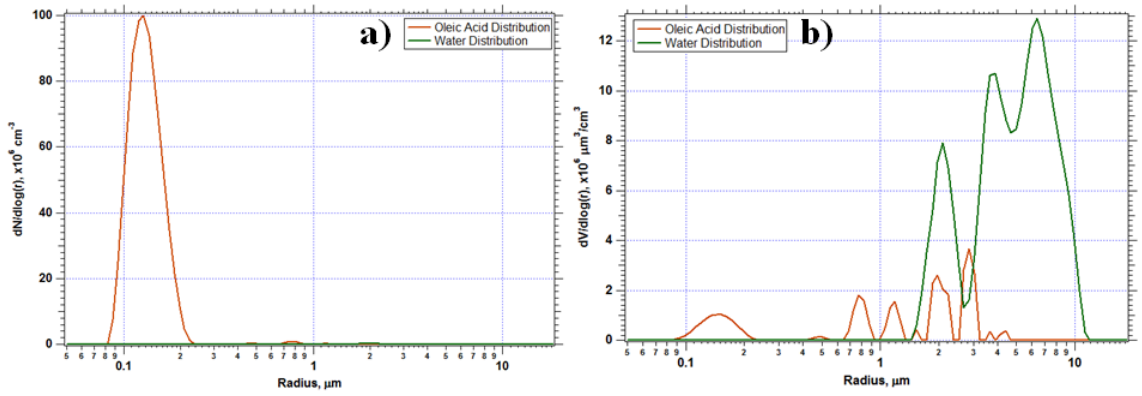

Figure 3.13: Corresponding (a) number density distribution and (b) volume density distribution from fit shown in Figure 3.12.

The fitting program was then run assuming that the particles were composed of a water core coated with oleic acid, and then again assuming the particles were composed of an oleic acid core coated with water. Figure 3.14 displays the same experimental spectrum as that shown in

Figure 3.12; however, this time the spectrum is fit using coated sphere basis set spectra. It is evident from the figure that assuming the particles were oleic acid coated with water produced a much poorer fit to the experimental spectrum. This was confirmed by the much larger χ value for the oleic acid core spectrum (χ = 0.1109) than for the water core spectrum (χ = 0.0296). In fact, the χ value for the oleic acid coated water particles was approximately the same as that for the fit shown in Figure 3.12. This called into question which calculated spectrum better represented the aerosol.

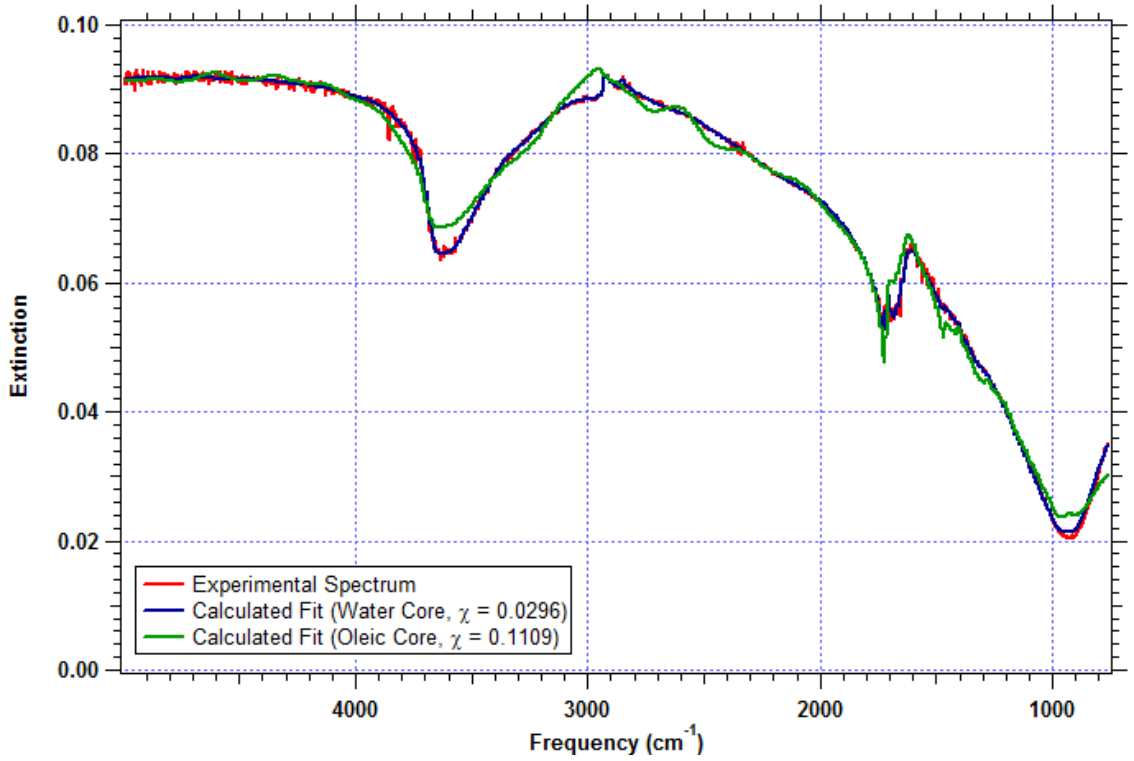

Figure 3.14: Sample spectrum of particles generated using Mira Mist CE nebulizer. Spectrum was fitted assuming the particles had a water core coated with oleic acid (blue fit) or an oleic acid core coated with water (green fit).

Comparing the volume density distributions may help determine the more probable distribution of the aerosol. Volume density distributions were used because they better highlight the presence of large particles than the number density distribution. The volume density

distribution for the water particles coated with oleic acid is given in Figure 3.15. This figure suggests that the aerosol consisted of water particles with a radius of 3 μm coated with a very thin film of oleic acid (~1 nm), and a mode of water particles approximately a micron in radius coated with a 275 nm coating of oleic acid. The distribution also suggests a number of other modes; however, these modes contributed very little to the overall volume when compared to the modes just listed. Deciding which distribution was more realistic, Figure 3.13b or Figure 3.15, was extremely difficult because no initial information was known about the aerosol. Therefore, quantifying multi-component aerosols was very arduous and if not done properly could introduce a large amount of error in the calculation of uptake coefficients.

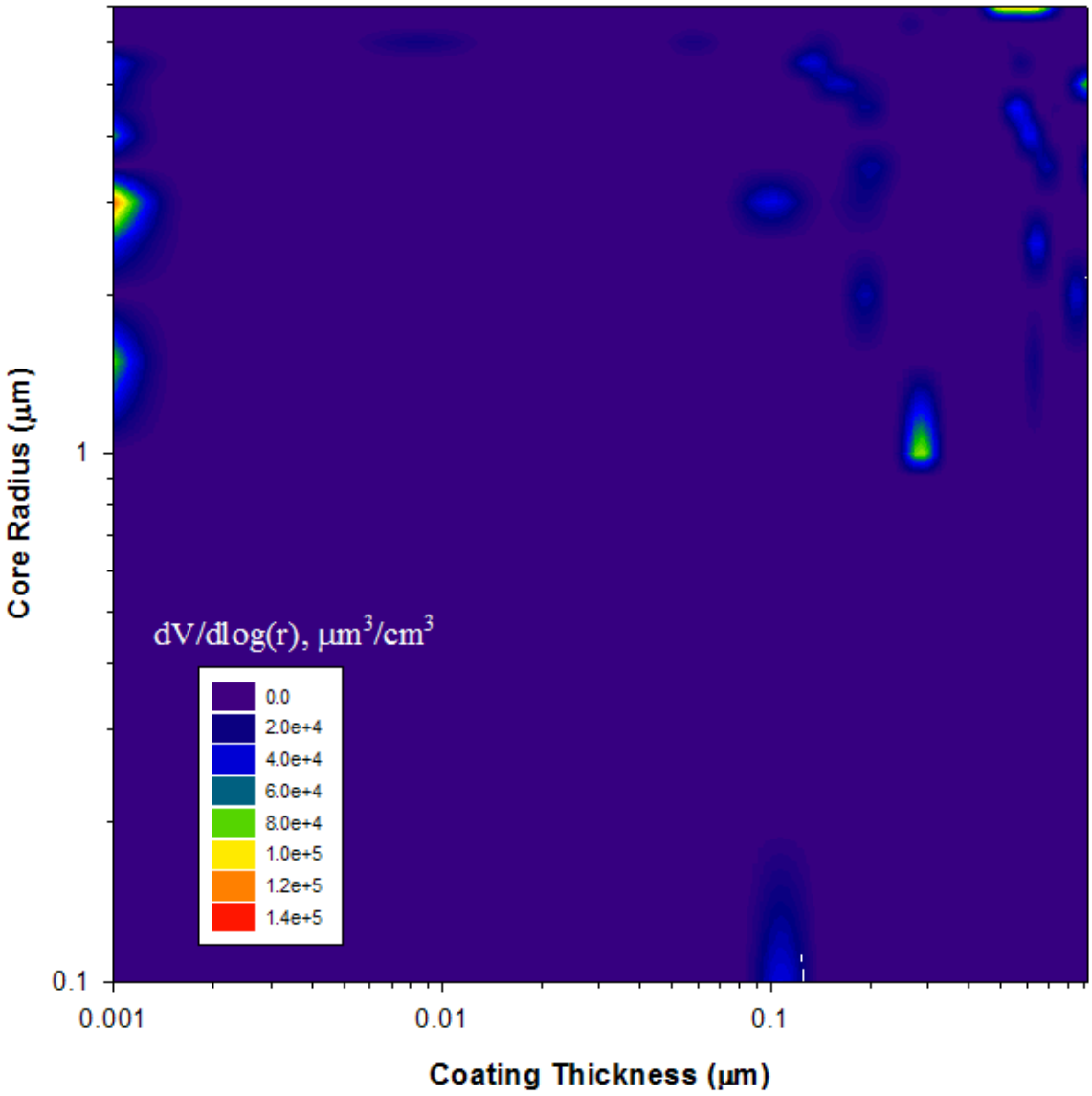

Figure 3.15: Volume density distribution for a multi-component aerosol consisting of water and oleic acid. Y-axis lists the radius of the water core of the particle. X-axis indicates thickness of oleic acid coating on water core. Inserted legend indicates volume density.

3.3.5 Aerosol Quantification and Pressure

During the course of testing both the TSI Atomizer and the Burgener Nebulizer, it was discovered that both instruments displayed a pressure dependence on the amount of aerosols produced.

Figure 3.16 shows four curves for the total surface area density (μm^2 of surface area per cm^3 of

air) produced by the TSI atomizer versus the operating pressure of atomizer. For all four curves the gas pressure into the atomizer was maintained at 45 PSI, and the flow of oleic acid into the atomizer was controlled by a needle valve (indicated as the number of turns on Figure 3.16).

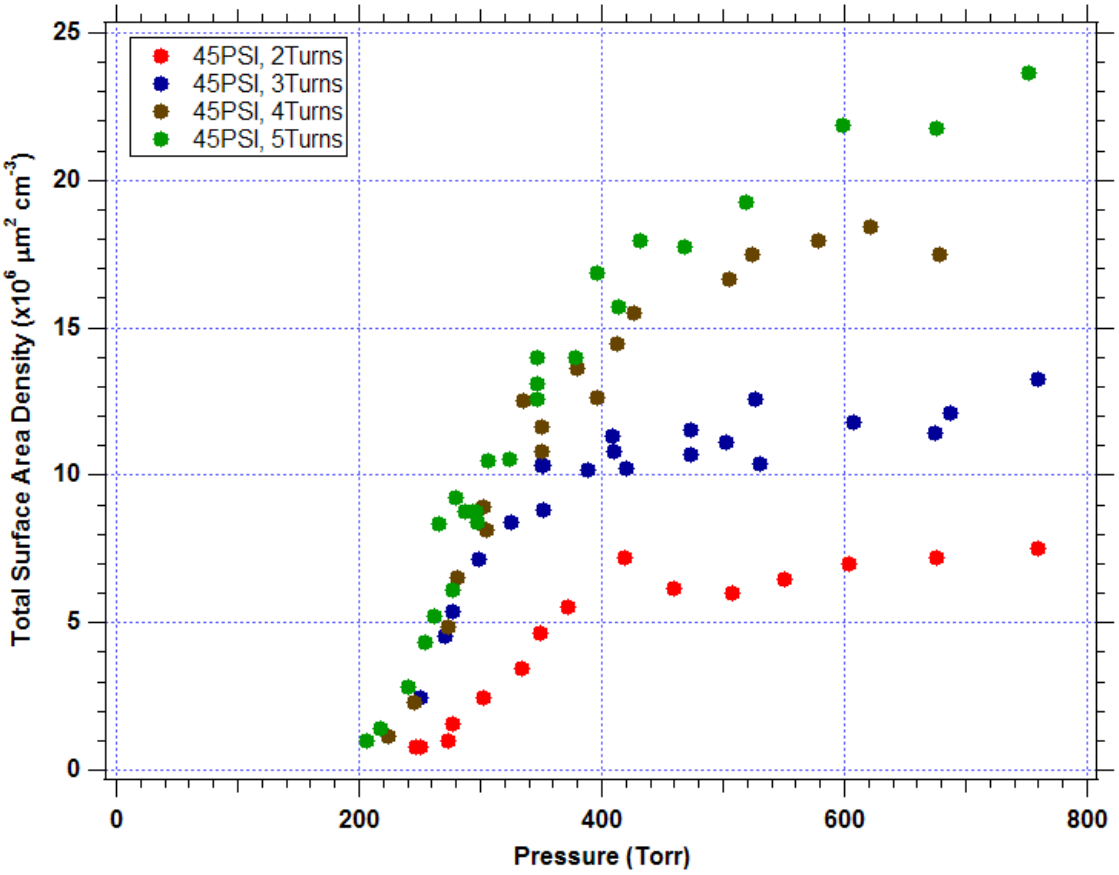

Figure 3.16: Total Surface Area Density of oleic acid aerosol produced by TSI Atomizer as a function of pressure.

It is clear from Figure 3.16 that the efficiency of the atomizer decreased with decreasing pressure to a point around 200 Torr where the concentration of aerosols seemed to fall below the detection limit of the FTIR. There appeared to be a plateau region in which the production of aerosols was relatively constant before dropping off sharply at lower pressures. One reason for this pressure dependence was the resulting decreased efficiency of the Venturi Effect at lower pressures.

A similar effect was seen with the Burgener nebulizer. Figure 3.17 shows spectra of water aerosols produced by the Burgener nebulizer at varying pressures within the system. As the pressure of the system was dropped, the signal from the FTIR was also lowered. One reason for the smaller signals resulted from a decreased efficiency of the nebulizer. At lower pressures, instead of the liquid flowing into the gas stream , via the spout (Figure 3.4), the liquid was physically pulled from the spout of the nebulizer, preventing it from flowing into the gas stream and thereby decreasing the production of aerosol particles.[119]

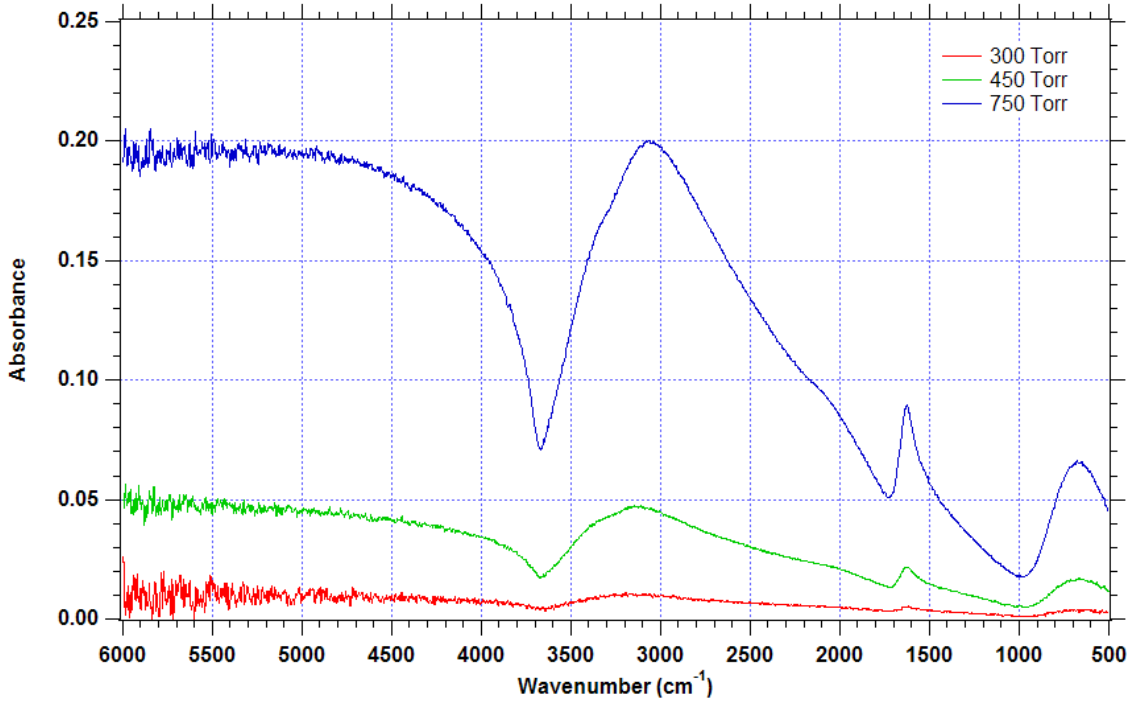

Figure 3.17: Spectra of water aerosols produce by the Burgener nebulizer at varying pressures.

To overcome this pressure dependency on the production of aerosols, a pinhole was placed in the flow tube to generate a high pressure region where the aerosols were produced. A variety of pinhole sizes were tested to determine which diameter would yield the optimal pressure for operating the various aerosol sources. For example, a 0.742 mm pinhole generated a pressure of approximately 600 Torr when the atomizer was operated with an input pressure of 45 PSI (3.7

STP L min^{-1} flow rate), while the same pinhole generated an operating pressure of 170 Torr with the Burgener Nebulizer (1.0 STP L min^{-1} flow rate). This allowed the flow tube to be operated at 40 Torr and yet still allowed the aerosol generators to operate at an optimal pressure.

Another explanation for the pressure dependency seen by both the TSI Atomizer and the Burgener Nebulizer was the pressure dependency of the FTIR to detect the aerosol particles. The detected intensity in the FTIR is proportional to the absorber concentration, according to Beer's Law

$$A = -\log\left(\frac{I}{I_o}\right) = \epsilon bc \qquad \text{Eq3.3}$$

where I is the signal intensity reaching the detector, I_o is the initial signal intensity, ϵ is the extinction coefficient, b is the path length and c is the concentration of the absorber. However, the concentration of the absorber is proportional to the flow velocity through the system, which is in turn dependent on pressure.

The velocity of the carrier gas in the flow tube is given by

$$v_{gas} = \frac{volumetric\ flow\ rate}{cross-sectional\ area\ of\ flow\ tube} \qquad \text{Eq3.4}$$

$$v_{gas} = \frac{volume/time}{cross-sectional\ area\ of\ flow\ tube} \qquad \text{Eq3.5}$$

Using the ideal gas law to obtain an equation for the volume of the gas, the velocity (m s^{-1}) can be mathematically written as,

$$v_{gas} = \frac{nR\,T/(P\,t)}{A} \qquad \text{Eq3.6}$$

and simplified to,

$$v_{gas} = \frac{nRT}{PtA} \qquad \text{Eq3.7}$$

where n is the number of moles of gas, R is the molar gas constant (J K^{-1} mol^{-1}), T is the temperature of the system (K), P is the pressure of the system (Pa), t is the time (s), and A is the cross-sectional area of the flow tube (m^2).

The flux of particles, assumed to be constant, in units of particles m^{-2} s^{-1}, exiting either the TSI Atomizer or the Burgener Nebulizer can be written as,

$$Flux = \frac{N_{particles}}{At} \qquad \text{Eq3.8}$$

The concentration of particles, in particles m^{-3}, can be written as,

$$Concentration = \frac{Flux}{v_p} \qquad \text{Eq3.9}$$

where v_p is the flow velocity of the particles (m s^{-1}). Substituting Eq3.8 into Eq3.9, and assuming $v_p = v_{gas}$, the concentration of aerosols can be described by,

$$Concentration = \frac{N_{particles}}{At} \cdot \frac{PtA}{nRT} \qquad \text{Eq3.10}$$

which simplifies to,

$$Concentration = \frac{P}{RT} \cdot \frac{N_{particles}}{n} \qquad \text{Eq3.11}$$

Therefore the concentration of aerosols, and hence the observable signal in the FTIR, is directly proportional to the pressure of the system. This implies that for low pressure applications, a large concentration of aerosols must be generated in order to be detectable. The Burgener Nebulizer was, therefore, chosen as the primary aerosol generator due to its lower flow. As derived above, the lower gas flow allowed for the production of a more concentrated aerosol and consequently a larger FTIR signal. To further help increase the FTIR signal, an expansion chamber was placed after the pinhole. Since its diameter was approximately five times larger

than that of the nebulizer tube, this chamber served the purpose of slowing the gas flow, which effectively concentrates the aerosol (Eq3.9).

According to Eq3.3, the observed signal in the FTIR is also proportional to the path length of the system. Therefore, a larger volume optical cell was installed in the flow tube. This helped maintain the velocity generated in the expansion chamber, while also increasing the path length. This further helped to improve the intensity of the observed FTIR signal.

3.3.6 Particle Size Control

One negative effect of the expansion chamber was that, despite the relatively low residence time within the chamber, the aerosols appeared to grow, resulting in multi-modal distributions and sizes of particles that were too large to be efficiently detected by the FTIR. Figure 3.18 shows some sample volume density distributions generated using the pinhole and expansion chamber configuration. Each distribution was generated using an input pressure of 45 PSI with the atomizer. The distributions shown are for two different flows of oleic acid into the atomizer controlled by a needle valve.

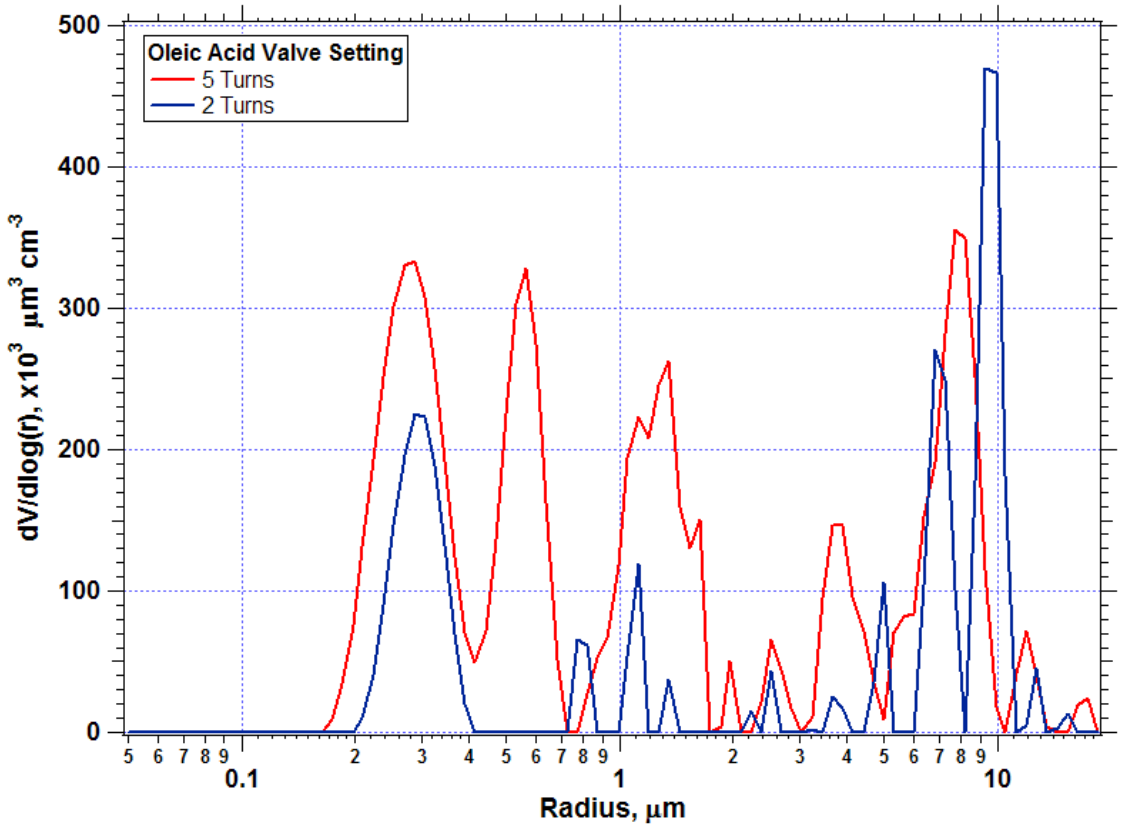

Figure 3.18: Sample volume density distributions of oleic acid generated using the TSI Atomizer.

To help control the size of the particles generated, an impactor was placed in the flow tube between the optical cell and the expansion chamber. The impactor was designed to remove any large particles above a specific, calculated size. From Figure 3.18, there appeared to be a distinct mode around a radius of 0.3 µm and another mode around 1 µm. Two impactors were then designed to isolate these modes and remove larger particles. The cutoff diameter, d_{50}, of an impactor is defined as the size at which particles of a larger size are removed from the flow, while particles less than that size pass through.[11] The first impactor was designed to remove particles with a radius larger than 0.75 µm (d_{50} = 1.5 µm), while the second impactor removed particles

larger than approximately 1.9 μm in radius (d_{50} = 3.8 μm). The resulting size distributions (Figure 3.19) had smooth lognormal-like shapes.

The impactor with a d_{50} of 1.5 μm was used for all uptake experiments. This impactor was chosen for two reasons. First, most organic particles found in the atmosphere are smaller than 1 μm in diameter.[13;126] Therefore, the impactor with a d_{50} of 1.5 μm generated size distributions more representative of ambient aerosols. Second, current literature is unclear on the effect that the size of the particle may have on uptake.[68] The removal of the larger mode ensured that the effect of particle size on uptake was minimized.

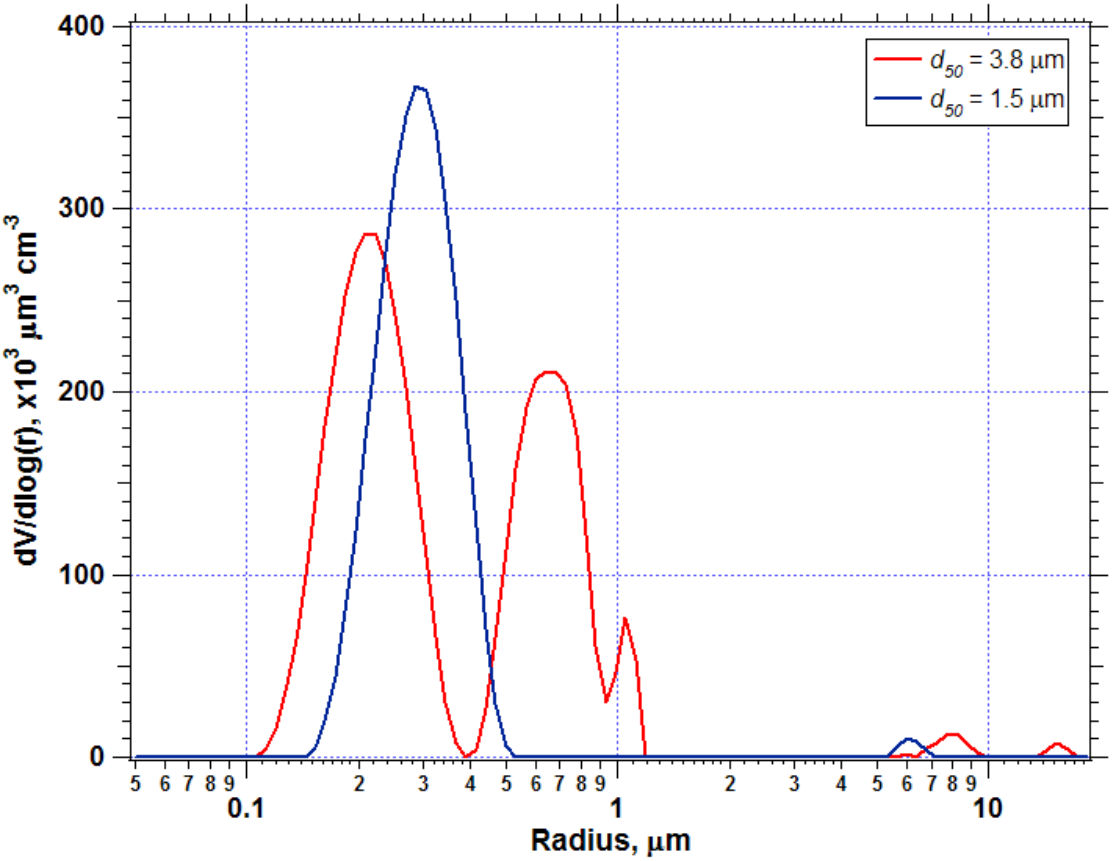

Figure 3.19: Resulting distributions of oleic acid aerosols generated by the TSI Atomizer using an impactor to remove large particles.

3.4 Aerosol Flow Tube Summary

After testing a variety of systems and designs, the final setup for the aerosol portion of the flow tube can be seen in Figure 3.20. Aerosols were generated with a Burgener nebulizer (a) at high pressure created by placing a pinhole at the front end of the expansion chamber (b). The impactor was located at the end of the expansion chamber, at the front end of the optical cell (d). The aerosol was detected in the optical cell by using an FTIR spectrometer (c) coupled to an external detector (e).

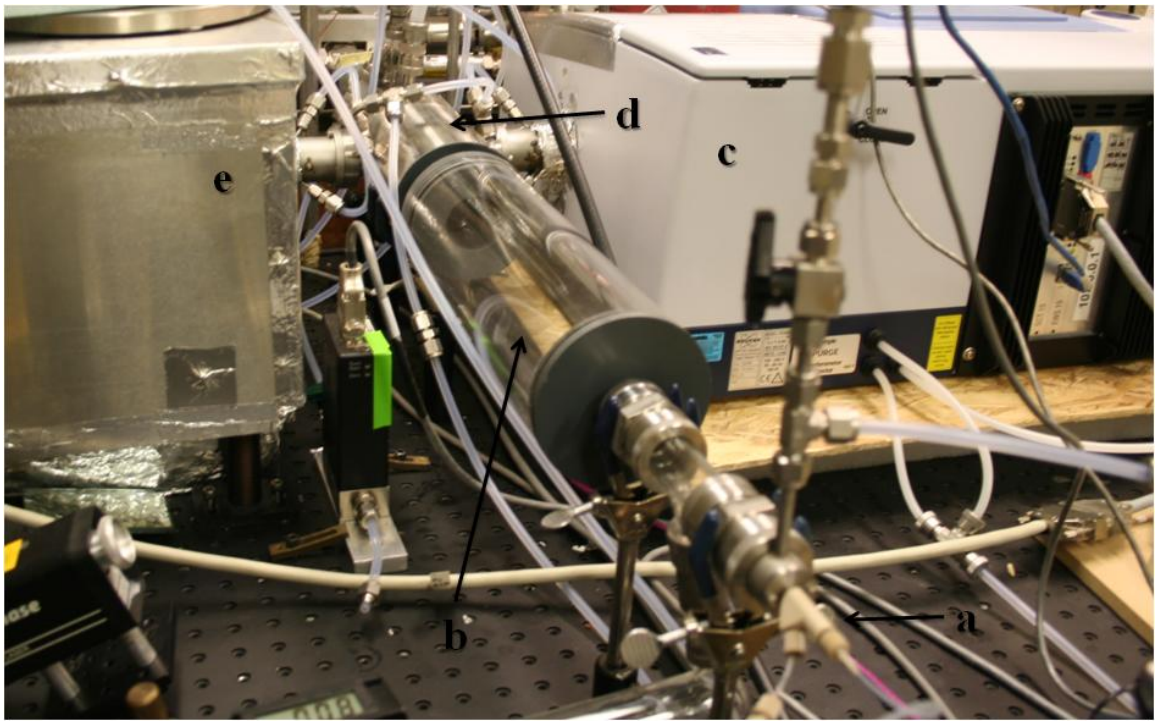

Figure 3.20: Aerosol portion of flow tube. (a) Burgener nebulizer. (b) Expansion chamber. (c) FTIR spectrometer. (d) Optical cell. (e) FTIR detector.

3.5 Isokinetic Sampling

It was observed that if excess aerosol flow was introduced into the reactive portion of the flow tube then the mass spectrometer signal of the ionizing agent was overly depleted (50 to 75%). Loss of intensity made it more difficult to observe other peaks in the mass spectra. Excess

surface area would also result in complete reaction between OH and the aerosol surface. This would result in loss of the OH signal in the mass spectrometer. Therefore, an isokinetic inlet was used to sample a small portion of the total aerosol flow into the reactive portion of the flow tube. The rest of the aerosol flow was pumped off by a mechanical rotary pump (Duo-Seal; Welch Scientific Company), enhanced with a blower (EH-250; BOC Edwards), through a ball valve to maintain low pressures. This allowed for a lower total surface area to be used in the uptake experiments.

The inlet was constructed of stainless steel surgical tubing with an inner diameter of 0.073" and a wall thickness of 0.010". The wall thickness of the inlet was extremely critical. The theory behind an isokinetic inlet assumes a uniform sampling of the bulk flow. This assumption can breakdown if the tubing wall is too thick.[11] Thick-walled tubing can generate turbulence at the sampling point, resulting in a breakdown of the uniform sampling assumptions.[127] To minimize loss of aerosol particles to the wall of the inlet, the inlet must also be as straight as possible.[11] Therefore, the use of thin-walled surgical tubing complied with both of these requirements for an optimal design of the isokinetic inlet. The sampling port of the inlet was placed within the optical cell as close to the FTIR beam as possible without obstructing the beam. This ensured that the aerosol sampled was the same aerosol detected by the FTIR system.

3.5.1 Isokinetic Inlet – CFD Simulations

To minimize aerosol loss in the isokinetic inlet it was initially designed to be as short as possible. Therefore, the inlet was designed to enter the reactive portion of the flow tube before the side arm inlet, where OH is generated and introduced into the flow tube. However, inconsistent uptake results suggested the presence of turbulence at the reactive gas inlet junction. This theory was confirmed when the inlet was modeled with CFD simulations (Figure 3.21a & b). Figure 3.21b clearly shows how the aerosol flow (green lines) was pushed to the outside of the flow tube when

it mixed with the He flow, which caused loss of the aerosol to the flow tube wall. The same system was then modeled by extending the isokinetic inlet 38 mm past the reactive inlet (Figure 3.21c & d). This resulted in no turbulent mixing as the gases continued along the flow tube.

Figure 3.21c & d also highlights the fact that an orthogonal inlet for the reactive species resulted in mixing of the reactants prior to the introduction of the aerosols. This indicated that the radial distribution of OH was well developed and inhomogeneities within the distribution had been removed. Therefore, no formal correction for radial concentration inhomogeneities was required.

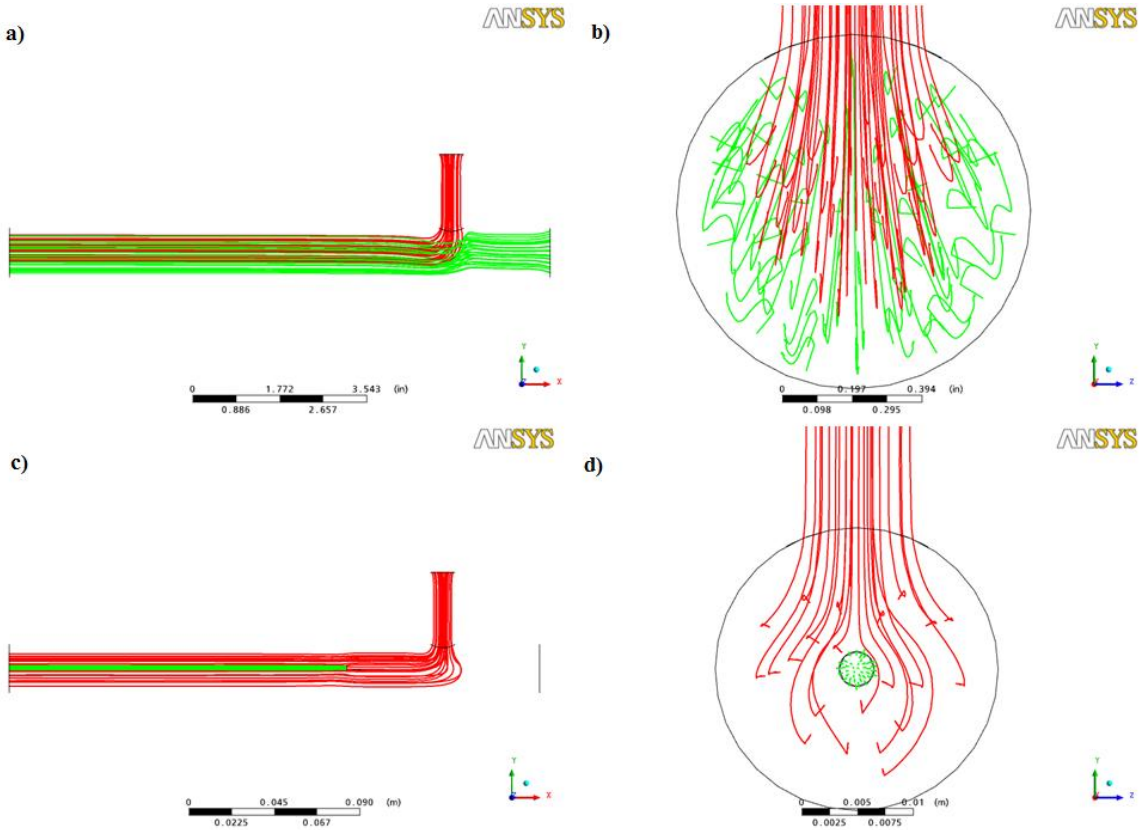

Figure 3.21: CFD results for reactive inlet without (a & b) and with (c & d) the isokinetic inlet. Red lines represent He flow from the reactive inlet. Green lines represent N_2 aerosol flow.

Figure 3.22 shows an image of the final isokinetic inlet design used during uptake experiments. The isokinetic inlet (c) exited the back of the optical cell (a) into the reactive portion of the flow tube (d). Note that the inlet extended past the side arm inlet (b), where OH was generated and introduced into the main flow tube.

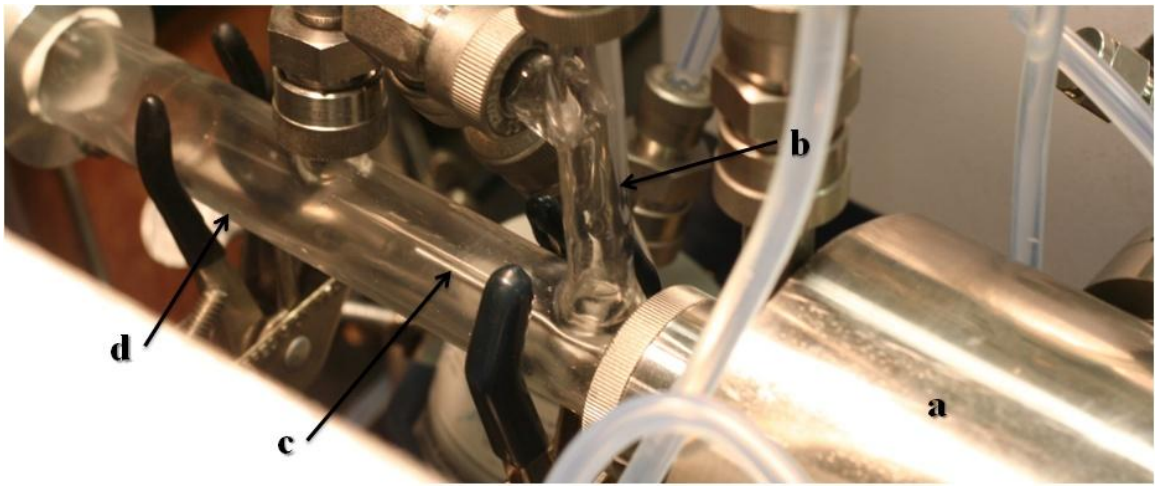

Figure 3.22: Image of final isokinetic inlet design highlighting the position of the inlet relative to the side arm inlet. (a) Optical cell. (b) Side arm inlet. (c) Isokinetic inlet. (d) Reactive portion of flow tube.

3.6 Mass Spectrometry

3.6.1 Radical Production

The hydroxyl radical was generated immediately downstream of the optical cell in a side arm via the reaction

$$H + NO_2 \rightarrow OH\cdot + NO \qquad \text{R3.1}$$

Hydrogen atoms were generated by the use of a microwave discharge produced by a Surfatron cavity (Sairem). The atoms were then injected into the side arm inlet via a moveable quartz inlet as shown in Figure 3.23. The side arm was constructed of 9.4 mm ID Pyrex and was 9 cm long. The side arm was constructed with one orthogonal inlet of 9.4 mm ID Pyrex for the introduction

of the NO_2 titrant. The specific conditions used to generate hydroxyl radicals will be described in detail in the following chapter.

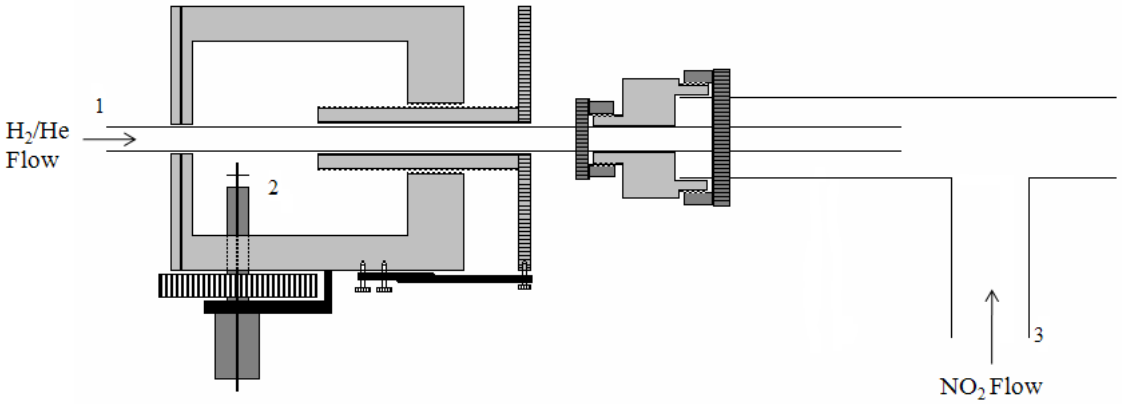

Figure 3.23: Schematic diagram of microwave cavity. (1) quartz inlet. (2) microwave cavity. (3) NO_2 inlet.

3.6.2 Chemical Ionization Mass Spectrometry

Hydroxyl radicals were monitored by chemical ionization mass spectrometry (CIMS), using sulphur hexafluoride (SF_6^-) as the ionizing agent. SF_6^- was generated by combining a 10 STP L min^{-1} flow of N_2 and a 10 STP cm^3 min^{-1} flow of SF_6. The SF_6/N_2 mixture passed through a radioactive polonium source (^{210}Po, Nuclecel In Line Ionizer, Model #: P-2031 2000; NRD LLC) that emits alpha particles. The alpha particle stripped the N_2 carrier gas of an electron, which was then picked up by SF_6, generating SF_6^-. Charge transfer then occurred between the OH radical and SF_6^-, generating OH^- by reaction R3.2.

$$SF_6^- + OH\cdot \rightarrow OH^- + SF_6 \qquad \text{R3.2}$$

which was detected by the mass spectrometer (*m/z* 17). The main advantage of CIMS is that it is a softer ionization process compared to more conventional mass spectrometers based on electron impact ionization, which commonly produces ion fragments. This results in cleaner mass spectra consisting of only the parent ion peak.

SF_6^- does not exclusively transfer its charge to OH. It will, in fact, transfer the charge to any molecule that has a higher electron affinity.[128] This resulted in the ability to monitor not only OH, but also NO_2 and any other secondary chemistry products. Table 3.2 lists some of the possible species that could be observed with the CIMS method using sulphur hexafluoride.

Table 3.2: Possible observable species with CIMS.

Compound	m/z Ratio	Observed as
OH	17.0	OH^-
NO_2	46.0	NO_2^-
HONO	47.0	$HONO^-$
O_3	48.0	O_3^-
NO_3	62.0	NO_3^-
HNO_3	82.0	NO_3HF^-
N_2O_4	92.0	$N_2O_4^-$
H_2O	124.1	OSF_4^-
HO_2	140.1	$SF_4O_2^-$
SF_6	146.0	SF_6^-

It was discovered that SF_6^- is highly reactive towards water vapour.[128;129] This was therefore seen to be a potential complication in the use of aqueous aerosols. To test this theory, the system was run with humidified nitrogen and no aerosols present. Even at very low relative humidities (< 10%) the depletion in the SF_6^- signal was virtually complete. Figure 3.24 displays the mass spectrum detected when dry nitrogen is used as the carrier gas (red line) and the mass spectrum detected when humidified nitrogen is used as the carrier gas (green line). Note that when humidified nitrogen was used the SF_6^- signal, at m/z 146, was reduced by more than 80% as it reacted with H_2O in the gas-phase.[129] The SF_6^- signal was replaced with a peak at m/z 124, corresponding to OSF_4^- as listed in Table 3.2. Other peaks present at lower masses were not identified. Due to this complication in the presence of water vapour, and the difficulty in

quantifying multi-component aerosols, it was determined that experiments should focus on the use of pure organic aerosols, utilizing dry nitrogen as the carrier gas.

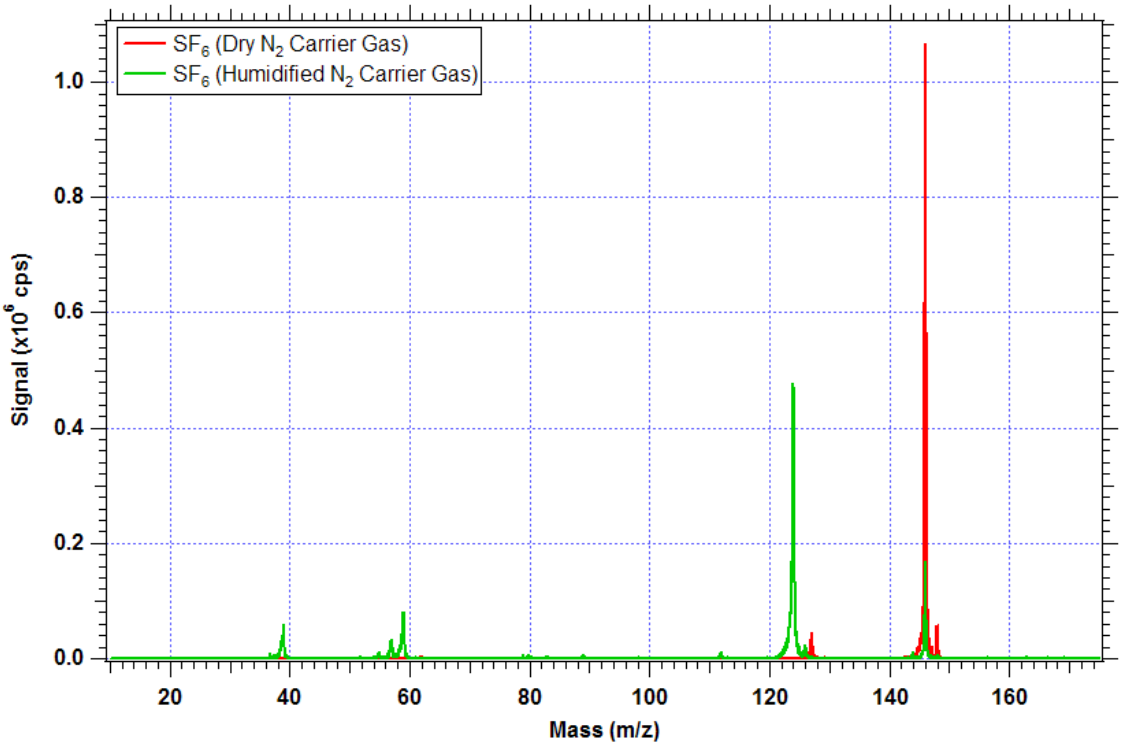

Figure 3.24: Influence of water vapour on mass spectrum. Spectrum observed with dry nitrogen carrier gas (red line) only shows peaks corresponding to SF_6^- and SF_5^-. Spectrum observed with humidified nitrogen carrier gas (green line) shows significant depletion of SF_6^- peak and the presence of the water-induced peak at m/z 124.

3.6.3 SF_6 Inlet – CFD Simulations

The initial design for the SF_6/N_2 mixture inlet was that of a single 9.4 mm ID Pyrex inlet orthogonal to the flow tube. Using standard flows for the system (10 STP L min^{-1} N_2, 1.5 STP L min^{-1} He from the side arm inlet) it was discovered that this design created a large amount of turbulence (Figure 3.25a). By redesigning the inlet to introduce the SF_6/N_2 mixture radially to the flow tube, a laminar flow was maintained (Figure 3.25b). Further CFD was performed to determine that the width of the inlet resulting in an optimal flow was 3.5 mm (Figure 3.26c).

Inlet widths smaller than 3.5 mm (Figure 3.26a & b) resulted in too much turbulence in the main flow of the system.

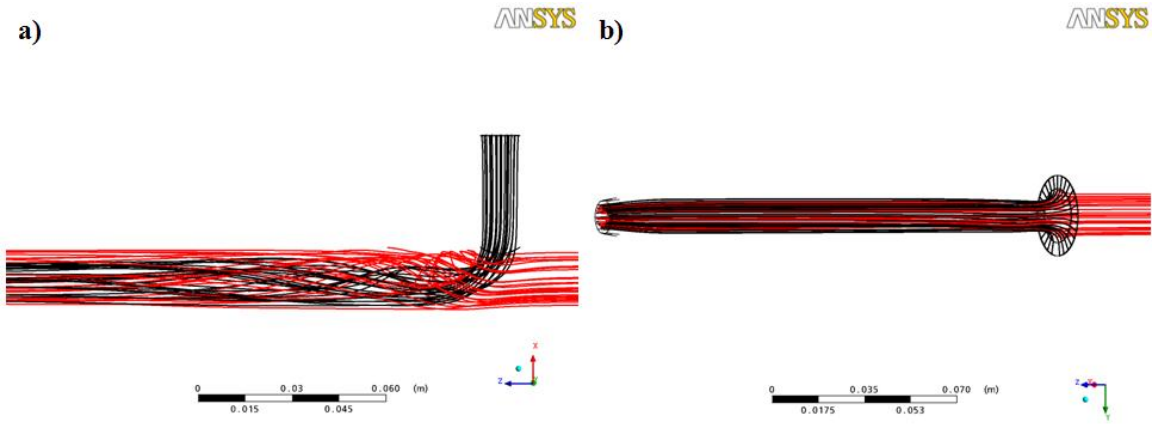

Figure 3.25: CFD results for SF_6/N_2 inlet designs. a) 90° degree inlet. b) Radial inlet. Red lines represent He flow, and black lines represent SF_6/N_2 flow.

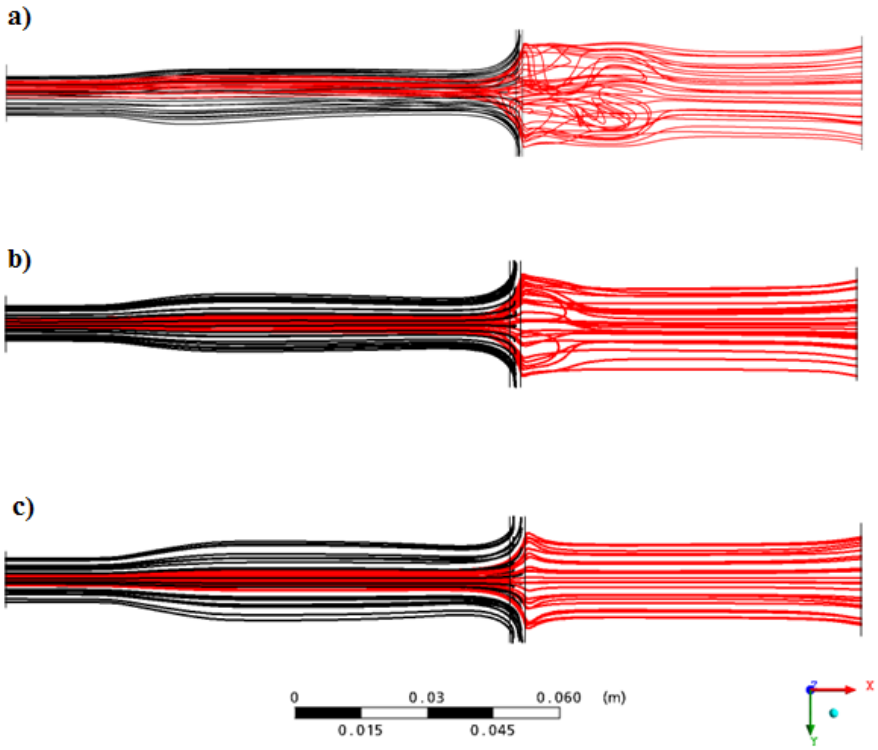

Figure 3.26: Influence of width of radial SF_6 inlet on flow dynamics. a) 1.5 mm inlet width. b) 2.5 mm inlet width. c) 3.5 mm inlet width. Red lines represent He flow, and black lines represent SF_6/N_2 flow.

3.6.4 Ion Detection

Ions generated by reaction with SF_6^- were detected with a quadrupole mass spectrometer in a three-stage differentially pumped vacuum chamber (Figure 3.27[111]). The initial design of the quadrupole system was based on the system outlined by Bacak (2004).[111]

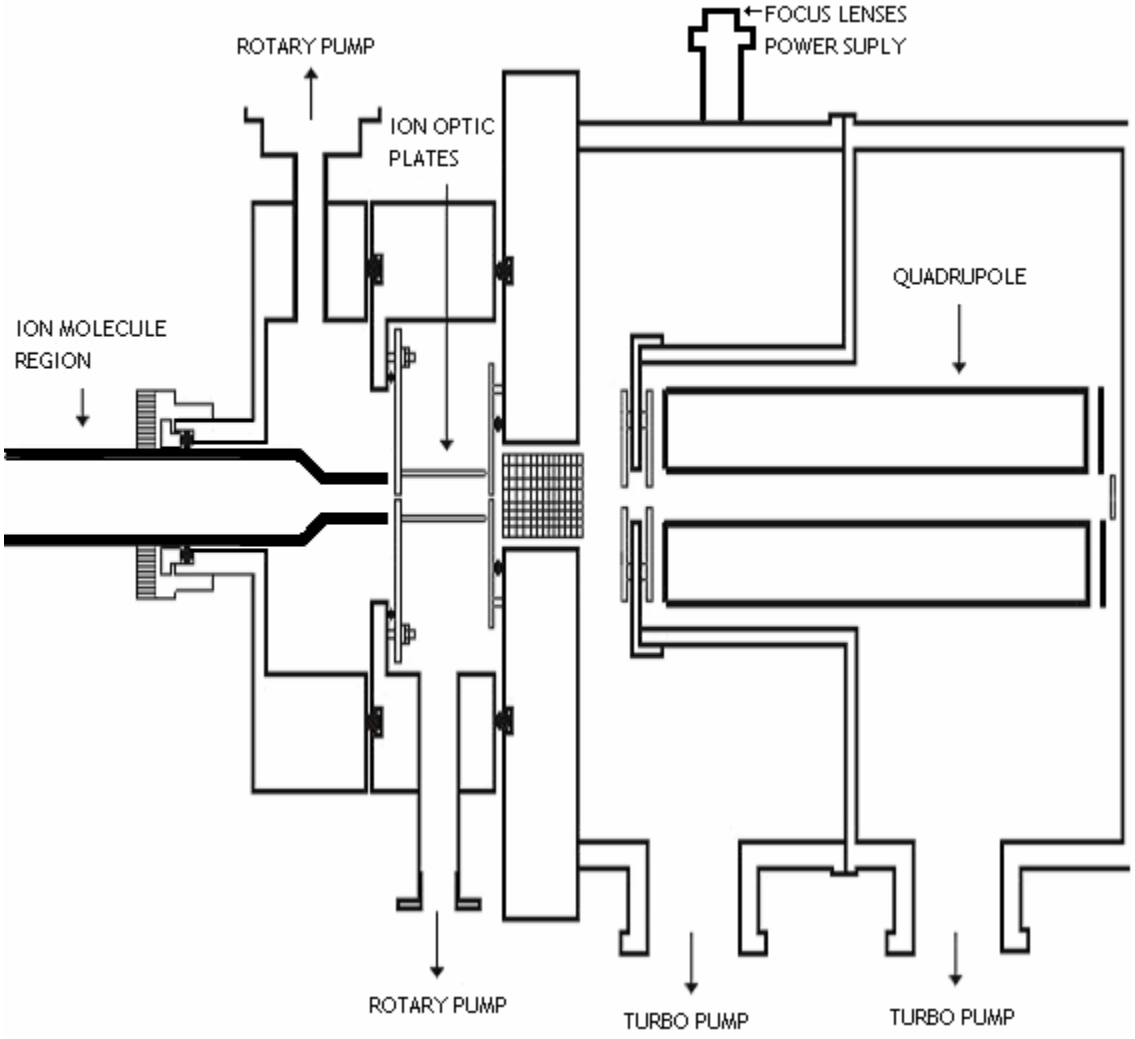

Figure 3.27: Schematic diagram of CIMS interface.

A sample of the bulk gas flow containing reactant ions was drawn into the front chamber of the mass spectrometer through an aperture, which was held at a negative potential to focus charged reactant molecules. The front vacuum chamber was pumped by a rotary pump (CD-300;

Varian, Inc) and held at 100 mTorr. The ions were further focused by a second aperture, which was also held at a negative voltage into a second chamber containing the ion optic lenses for the mass spectrometer. The ion optic lenses were used to further focus the ions and enhance detection. This second chamber was pumped by a turbomolecular pump (TMH 521; Pfieffer Vacuum, Inc) to an operating pressure of approximately 10^{-4} Torr. The quadrupole mass filter and rear detection chamber of the mass spectrometer (ABB; Extrel CMS, LLC.) holding the multiplier assembly was pumped by a second turbomolecular pump (Turbo V-70LP; Varian, Inc) to an operating pressure of approximately 10^{-6} Torr. Both turbomolecular pumps were backed by the same mechanical rotary pump (E2M80; BOC Edwards). Ions were detected with a channeltron via negative ion counting.

A number of experiments were conducted to determine the optimal size of the pinholes used to sample and focus the ions. Pinholes larger than 0.4mm on the first ion optics plate admitted too much gas into the quadrupole system and resulted in pressures higher than 10^{-6} Torr in the detector region. These higher pressures caused an increase in the noise level of the detector, making detection of ions more difficult. Conversely, if a pinhole smaller than 0.4 mm was used on the first ion optic plate, the amount of material entering the quadrupole system was too small and the detected signals dropped dramatically. Therefore, a pinhole of diameter 0.4 mm on the first ion optic plate was determined to optimize the signal in the mass spectrometer. For the second ion optic plate, a pinhole the same size as the first, or smaller, was required to maintain the operating pressures in the detection region of the mass spectrometer. Apertures of 0.4 and 0.2 mm diameters were tested. Using the 0.4 mm aperture created pressures higher than 10^{-6} Torr in the detector region. Therefore, the 0.2 mm aperture was used since it maintained an operating pressure of 10^{-6} Torr.

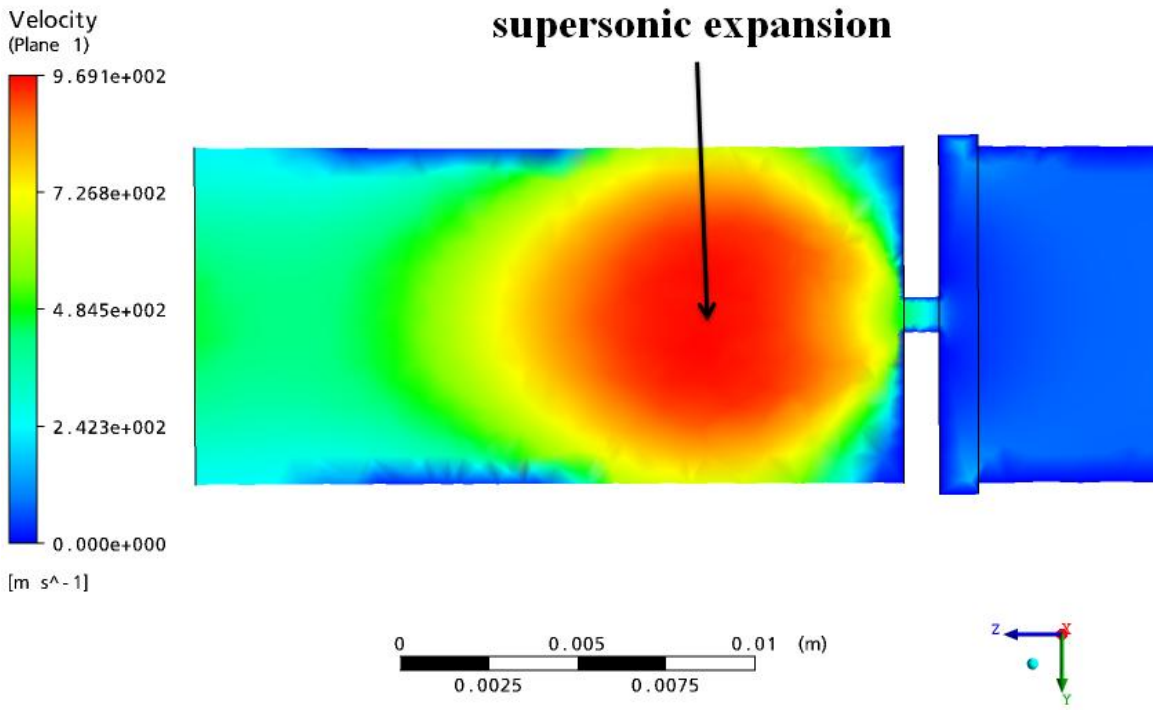

Figure 3.28: CFD output of supersonic expansion region generated after first pinhole in mass spectrometer.

CFD modeling of the first pinhole plate indicated a supersonic expansion region immediately after the pinhole (Figure 3.28). Since the mean free path of a molecule is much greater behind a shockwave (i.e. in the expansion region), it was theorized that if the ions could be sampled within this expansion region a higher signal would be detected due to lower loss of ions from collisions. The second pinhole plate was designed to hold a skimmer cone (Model 1, 0.2 mm orifice; Beam Dynamics, Inc.) that would extend into the expansion region and sample the ions from the flow tube. The cone was attached to the ion optic plate with electrically conductive silver epoxy (Part No: 8331-14G; MG Chemicals), and strengthened with Torr Seal epoxy to ensure a vacuum seal between the two chambers (Figure 3.29). Unfortunately, this

arrangement did not appear to improve the observed signal in the mass spectrometer compared to a simple pinhole design for the second ion optics plate. Therefore, in the current configuration, the cone design was abandoned for a simple pinhole on the second plate.

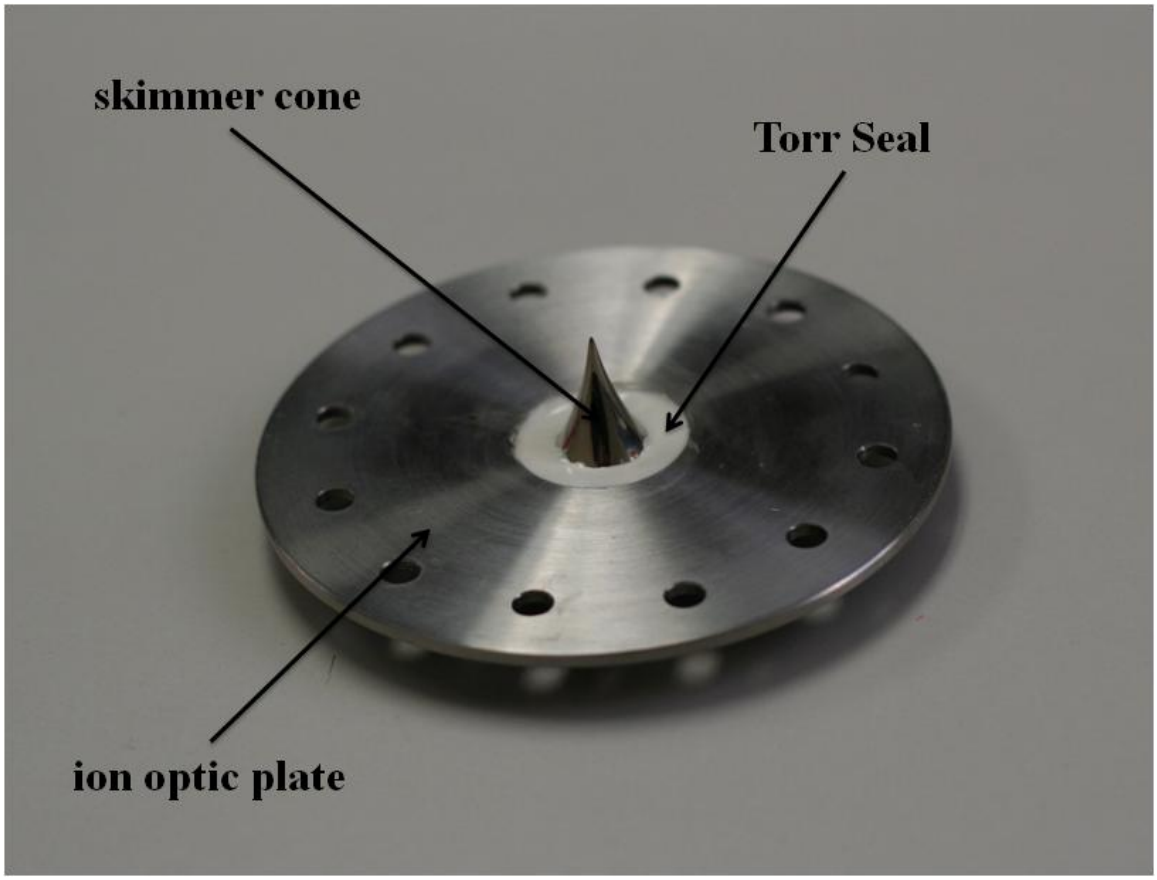

Figure 3.29: Skimmer cone affixed to second ion optic plate via electronically conductive epoxy. White substance surrounding cone is Torr Seal, which was used to ensure a vacuum seal between the two chambers of the mass spectrometer.

It should be noted, however, that to truly test this configuration, the skimmer cone should be affixed to a translational stage so that its position relative to the first pinhole can be adjusted. This would allow for the determination of the optimal position for sampling ions exiting the first pinhole. A complete re-configuration of the front end of the mass spectrometer would have been required to install a translational stage into the current design of the mass spectrometer.

However, since sufficient signal was achieved without the use of the cone (~ $1x10^6$ counts per second of SF_6, Figure 3.24) it was determined that this work was not necessary to improve the operation of the current mass spectrometer system.

The optimal voltages on the ion optic plates and the internal focusing lenses of the mass spectrometer were determined by iteratively and successively varying the voltages while monitoring key peaks in the mass spectrometer. Mass-to-charge ratios of 17 (OH^-), 46 (NO_2^-) and 146 (SF_6^-) were monitored in single ion mode to maximize the signals, while mass-to-charge ratio 50 was monitored to determine the background level in the mass spectrometer since no peaks were expected to appear at this mass. The voltages on the internal optic plates were controlled using the software supplied with the mass spectrometer (Merlin), while the first and second ion optic plates were controlled via an external power supply. A stainless steel wire mesh was attached to the back side of the first ion optic plate (Figure 3.30) to help focus the ions as they entered the first chamber of the mass spectrometer. The wire mesh was secured to the plate with electronically conductive silver epoxy. The wire mesh acted as a focusing tunnelling for the ions since it carried the same voltage as the pinhole and plate. It was observed that the signal in the mass spectrometer increased when the mesh was used compared to when the mesh was removed from the system.

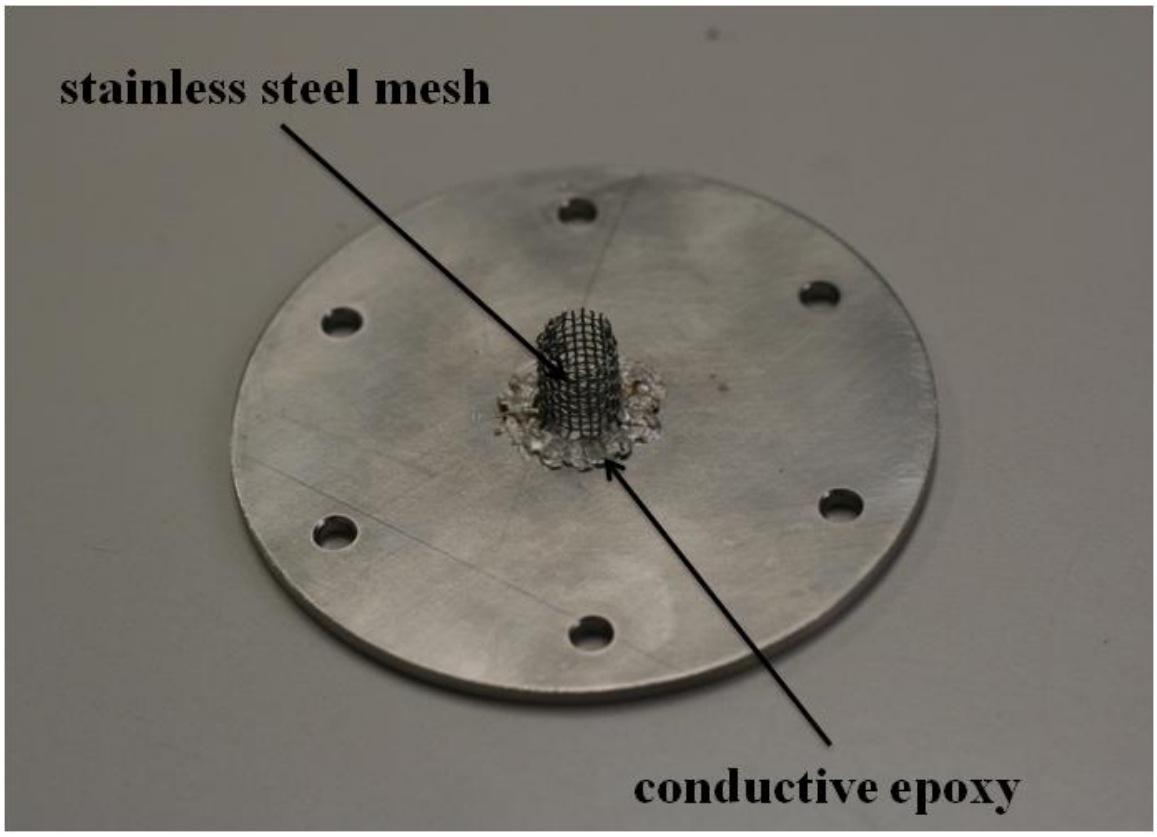

Figure 3.30: Stainless steel wire mesh attached to back side of first ion optic plate to guide ions towards second ion optic plate and pinhole.

3.7 Reactive Flow Tube Summary

The final configuration for the reactive portion of the flow tube is shown in Figure 3.31. The isokinetic inlet (e) exited the back of the optical cell (a) and extended past the side arm inlet (b,c, &d). The aerosols then entered the reactive portion of the flow tube where they underwent reaction with hydroxyl radicals produced by the reaction of hydrogen atoms with NO_2. The polonium sources (g) generated SF_6^-, which reacted with OH to produce OH^-. OH^- and all other negatively charged species were detected by the mass spectrometer (i).

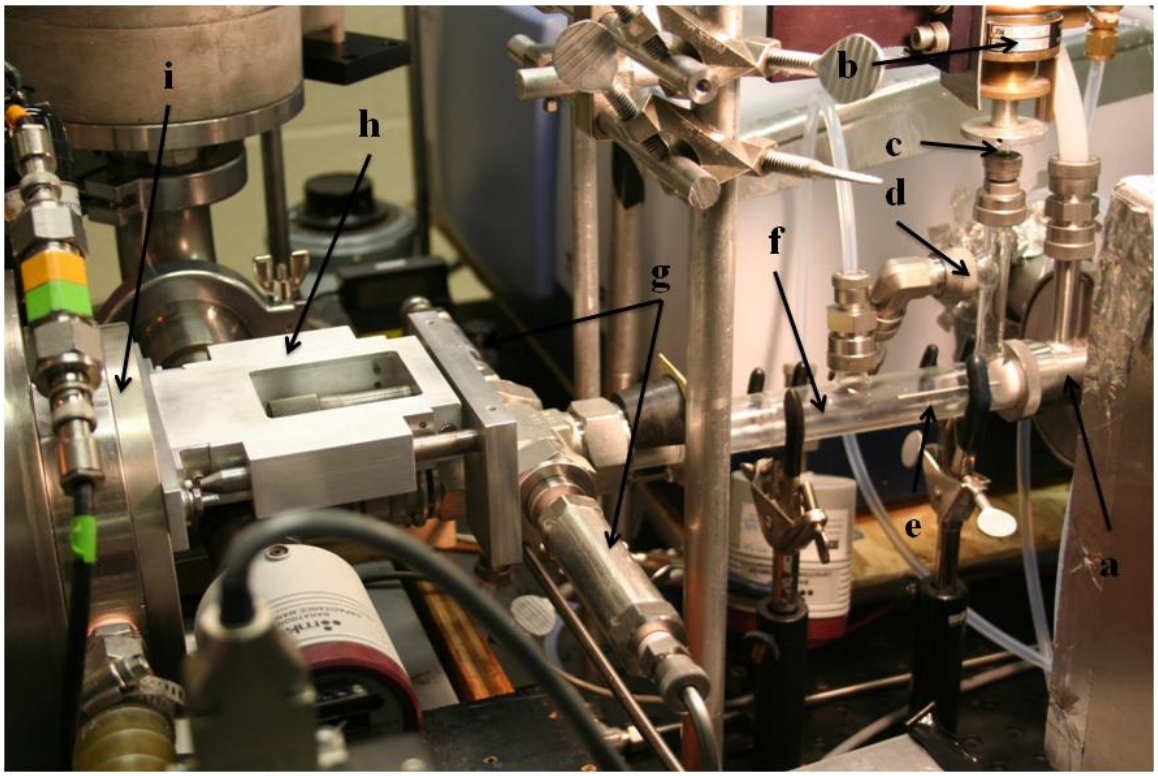

Figure 3.31: Image of reactive section of flow tube. a) Back end of optical cell. b) MW cavity. c) H atom inlet. d) NO2 inlet. e) Isokinetic inelt. f) Reaction region. g) Polonium sources. h) Flow tube space adjuster. i) Mass spectrometer.

3.8 Reaction Time

Simulations that track the time it takes for a particle to traverse the entire system were made using the same CFD model shown in Figure 3.21c & d. Monitoring the travel time for 100 particles, the particle time was plotted versus the particle position within the system (Figure 3.32). The position x = 0 indicates the point at which SF_6^- was introduced into the system and all reactions were assumed to be complete. The isokinetic inlet introduced the aerosols into the reactive portion of the flow tube approximately 0.18 m from the SF_6^- inlet. According to Figure 3.32 the particle residence time varied from 80 to 85 ms. Therefore, an average reaction time of 82.5 ± 2.5 ms was used in the calculation of the uptake coefficient.

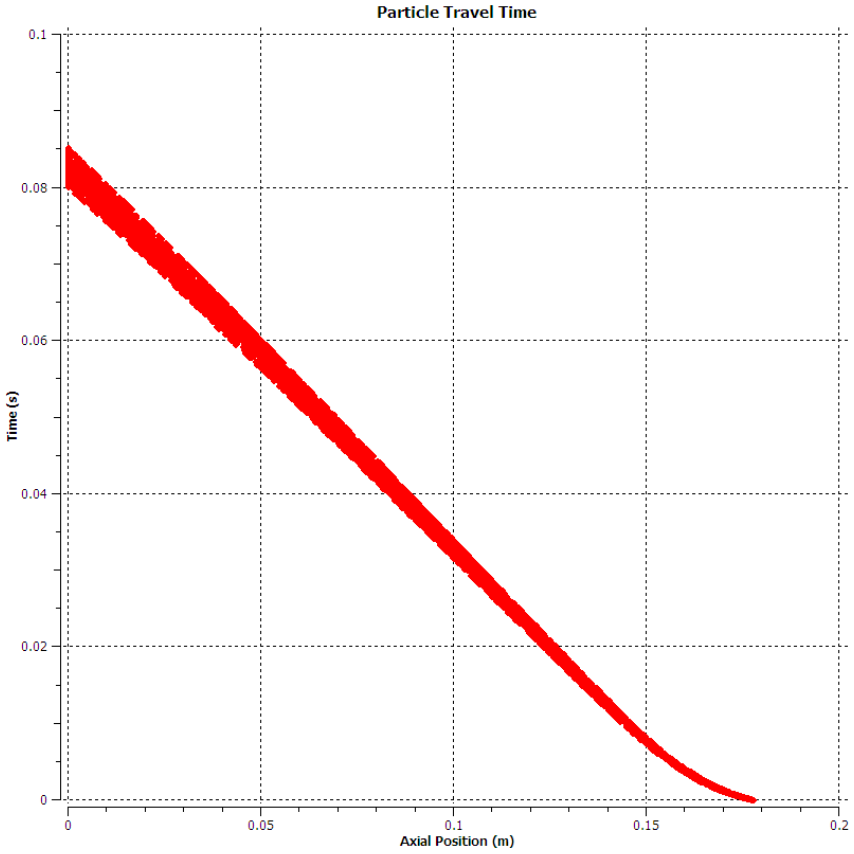

Figure 3.32: Residence time for oleic acid particles within system as calculated by CFD.

3.9 Summary

A low pressure aerosol flow tube (LP-AFT) was designed for the purposes of studying the heterogeneous reaction between the hydroxyl radical and organic aerosol particles. A schematic of the entire flow tube and instrumentation arrangement is shown in Figure 3.33.

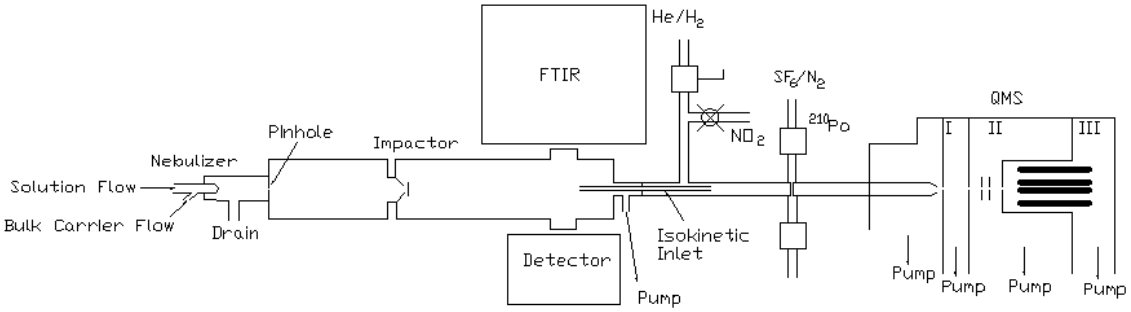

Figure 3.33: Schematic diagram of complete Aerosol Flow Tube Chemical Ionisation Mass Spectrometer.

A commercially available nebulizer was used to produce aerosols of varying composition and surface area density distributions. Aerosols were detected by FTIR spectroscopy and quantified by fitting the measured spectra with theoretically calculated spectra of monodisperse aerosols. A small volume of the aerosol was then sampled through an isokinetic inlet into the reactive portion of the flow tube. Hydroxyl radicals (OH) were generated by reacting hydrogen atoms (H) with nitrogen dioxide (NO_2). Hydroxyl radicals reacted with the aerosol particles for a given amount of time before they were detected by use of a chemical ionisation mass spectrometer. Hydroxyl radicals were converted to hydroxyl anions (OH^-) by reaction with sulphur hexafluoride anion (SF_6^-). All ions were detected with a quadrupole mass spectrometer in a three-stage differentially pumped vacuum chamber. All experiments were performed under dry conditions of 0% relative humidity.

Chapter 4
Experimental Results

4.1 Introduction

In the troposphere the primary source of OH is through the reactions[5]

$$O_3 + h\nu \rightarrow O(^1D) + O_2 \qquad \text{R4.1}$$

$$O(^1D) + H_2O \rightarrow OH\cdot + OH\cdot \qquad \text{R4.2}$$

Photolysis of ozone at wavelengths less than ~310 nm produces an excited singlet oxygen atom capable of reacting with atmospheric water to produce two hydroxyl radicals. The resulting hydroxyl radicals primarily react with hydrocarbons, such as methane (CH_4), and with carbon monoxide (CO).[3] In unpolluted environments, these reactions ultimately lead to the destruction of ozone via R4.1.[5] In polluted environments, however, the resulting chemistry increases local levels of ozone.[5;6]

While the gas-phase chemistry of OH is well understood and characterized[5], its heterogeneous chemistry is still poorly known. The influence of heterogeneous chemistry on the budget of OH may or may not be significant depending on the environment.[38;39;42;46;49;50] Furthermore, the oxidation of organic particles by OH could lead to significant changes in the composition of atmospheric aerosols. These changes could alter the influence of organic particles on cloud formation and lifetime, as well as the particles ability to scatter solar and terrestrial radiation. To begin to understand the importance of heterogeneous chemistry, it is important that scientists be able to efficiently and accurately study the uptake process.

4.2 Previous Experimental Studies

Previous work on the heterogeneous reaction of OH with organic surfaces was summarized in Table 2.3, highlighting the fact that there has been a variety of studies utilizing a wide range of

techniques. These experiments report a significantly large span of uptake coefficients, γ, ranging from 0.2 to values significantly greater than unity. The characterization of this reaction is important for tropospheric chemistry, and an order of magnitude difference in the uptake coefficient results in an order of magnitude difference in the rate coefficients of OH with organic surfaces. Therefore, there is still a significant amount of error involved in modeling this heterogeneous chemistry. This chapter reports on the results of a study of the kinetics of hydroxyl radical with organic aerosols carried out in a low pressure aerosol flow tube (LP-AFT) at standard temperature. These results improve our knowledge of this uptake coefficient.

4.3 Experimental Design

A schematic diagram of the apparatus was shown in the previous chapter (Figure 3.33). The flow tube was constructed from 22 mm ID Pyrex tubing, the walls of which were coated with Halocarbon wax (Halocarbon Products Inc.). The reactive section of the flow tube was pumped by a mechanical rotary pump (E2M80; BOC Edwards), enhanced with a blower (EH-250; BOC Edwards), through a butterfly valve to maintain low pressures. Pressure in this section of the flow tube was held at 37 to 39 Torr.

The aerosol section of the flow tube was pumped by a mechanical rotary pump (Duo-Seal; Welch Scientific Company), enhanced with a blower (EH-250; BOC Edwards), through a ball valve to maintain low pressures. Pressure in this portion of the flow tube was maintained at 39 to 41 Torr. Pressure in the aerosol section of the flow tube was kept at 1 – 2 Torr higher than the reaction section to ensure proper isokinetic sampling of the aerosols. All gas flows were monitored with calibrated mass flow controllers (Omega). The pressures in both sections of the flow tube were monitored using a 0 – 100 Torr capacitance manometer (MKS Baratron).

The average flow velocity in the reactor was 0.83 m s^{-1}, and the Reynolds number was less than 10, indicating laminar flow. The entrance length (the distance required to develop a

parabolic velocity profile) of the He carrier gas was 1 cm, and the mixing time (the time required for diffusion to reduce a radial concentration inhomogeneity to 5% of its initial value) was 0.015 s, which corresponds to a mixing distance of 1.2 cm. Since the aerosol was introduced into the bulk flow along the centre line of the flow tube at a distance of approximately 3.8 cm after the side arm inlet, these values indicate that the flow was well developed and that the OH radicals should have developed a uniform radial concentration at the starting point of reaction. This assumption is further justified by CFD simulations (Figure 3.21c & d) that indicated the use of a perpendicular helium inlet results in a fast mixing of the flow and, consequently, a uniform radial distribution of OH.

4.4 OH Generation

4.4.1 Procedure

OH was produced upstream of the flow tube via reaction R4.1

$$H + NO_2 \rightarrow OH\cdot + NO \qquad \text{R4.1}$$

Hydrogen atoms were produced by combining 1.5 STP L min^{-1} flow of He with a 1.0 – 2.0 STP cm^3 min^{-1} flow of 0.025% H_2 in He, which was then passed through a discharge, produced by a Surfatron microwave cavity (Sairem), operating at 75 W. To produce OH radicals, the H atoms were injected into a side arm of the flow tube located after the optical cell and mixed with a 2 – 2.5 STP cm^3 min^{-1} flow of 0.050% NO_2 in He. At the pressures and flow conditions used in this study, it is estimated that the H atoms have been completely titrated before entering the flow tube.

4.4.2 Materials

Nitrogen dioxide (99.5%; Linde Canada Ltd) was isolated and purified by freeze-pump-thaw cycles to remove any nitric oxide (NO) and nitrous oxide (N_2O) impurities. NO_2 mixtures were generated by mixing the purified NO_2 with helium (99.9999%; Praxair) to dilution a ratio of

1:2000, respectively, in a manifold. The total pressure of the mixture was kept around 2000 Torr. For the generation of H_2/He mixtures, H_2 (99.9999%; Praxair) and He (99.9999%; Praxair) were used as supplied. H_2 mixtures were generated by mixing H_2 and diluting with helium to a ratio of 1:4000, respectively. The total pressure of the mixture was kept around 4000 Torr.

Research grade helium (99.9999%; Praxair) was used as a continuous supply of gaseous helium. The helium was passed through a trap held at 77 K containing a molecular sieve (Type 4A; EMD Chemicals Inc.). Clean sieve was installed before every experiment and further cleaned by heating with a heating tape to a temperature of 150 – 160°C and left exposed to vacuum over night. Between experiments, the sieve was kept in an oven at a maintained temperature of 150°C to purify the sieve of any impurities. A liquid nitrogen tank (Praxair) was used to supply gaseous nitrogen as the carrier gas for sulphur hexafluoride (SF_6) and aerosol generation. The nitrogen gas was further purified by passing it through a GasClean Filter (Entegris). SF_6 (99.9%; Praxair) was used as supplied.

Oleic acid (Technical Grade; EMD Biosciences, Inc.) was used as supplied for the generation of oleic acid aerosols.

4.5 Experimental Procedure

4.5.1 Aerosol Detection Limit

The detection limit of the FTIR was estimated by minimizing the amount of aerosols in the flow tube until no discernable scattering signal could be seen in the spectra. Control of number densities was achieved by lowering the flow of solution through the nebulizer. Control of particle sizes was achieved by changing the size of the impactor. The fitting program was then used to calculate the number and size distributions of the aerosols generated. The FTIR was found to be sensitive to aerosol number densities above $1x10^4$ particles cm^{-3} for oleic acid aerosols log-

normally distributed at a radius of ~ 0.4 μm. Note that this sensitivity applies only for the specific experimental conditions at which it was tested (40 Torr, 1 STP L min^{-1} carrier through nebulizer). Sizes of particles smaller than 0.2 μm in diameter could not be accurately quantified because their size parameters fall outside the Mie range for the wavelength range of the FTIR.

A sample aerosol extinction spectrum for oleic acid taken during an uptake experiment can be seen in Figure 4.1. The extinction spectrum is representative of all aerosol samples studied and indicates the intensity relative to that of the FTIR background. The corresponding distributions for Figure 4.1 are shown in Figure 4.2. Figure 4.2a displays the number density distribution and lists the total number density, while Figure 4.2b presents the surface area density distribution with the total surface area density listed.

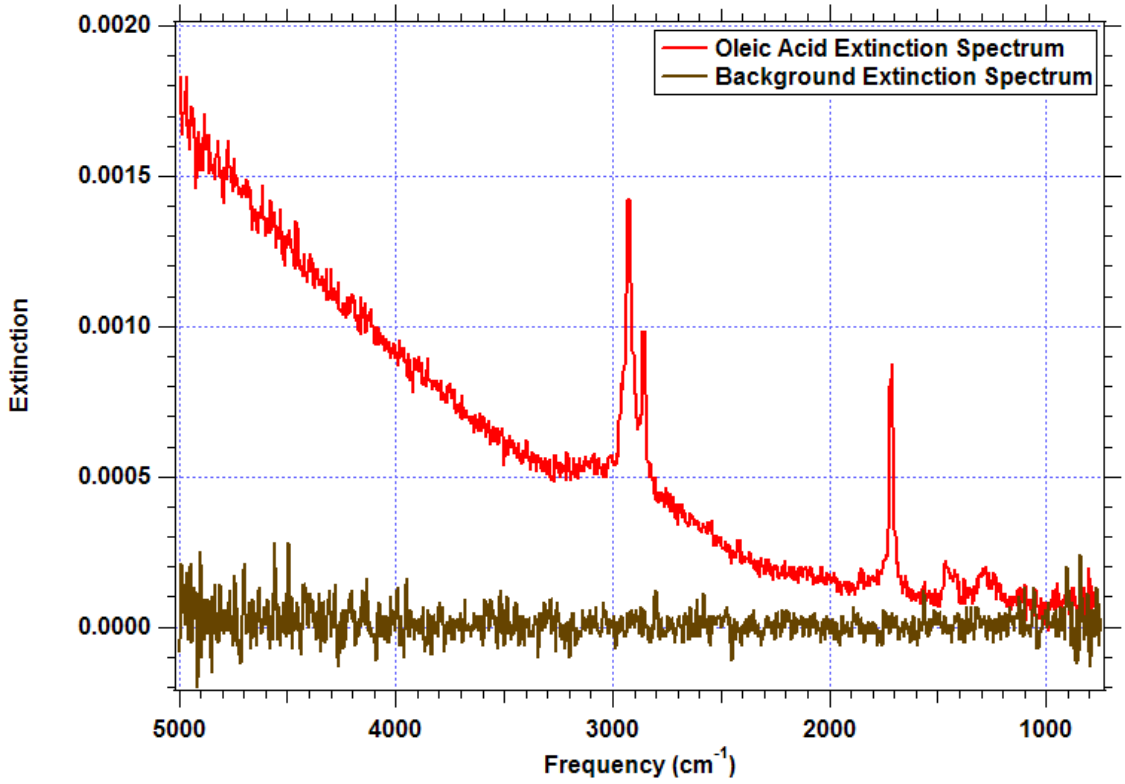

Figure 4.1: Sample spectrum of oleic acid aerosol taken during uptake experiment. Spectrum shows extinction intensity relative to background of FTIR.

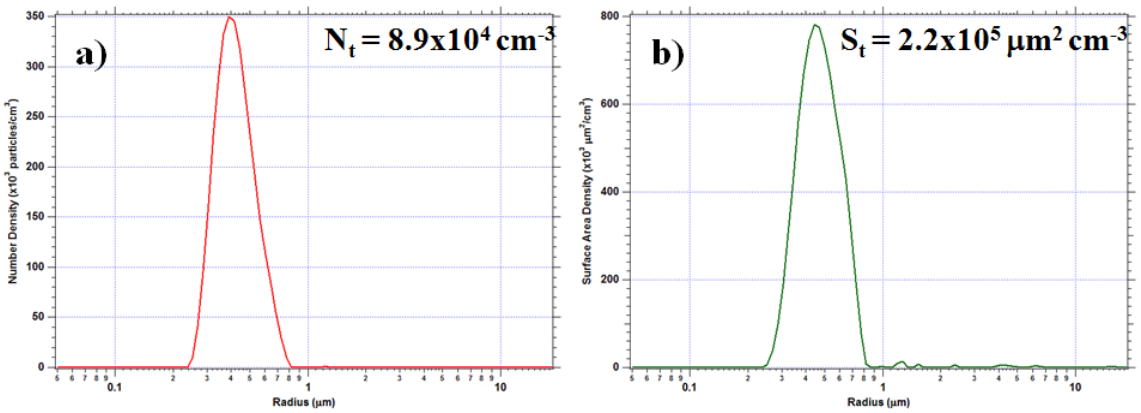

Figure 4.2: Retrieved distributions for extinction spectrum in Figure 4.1. a) Number density distribution. b) Surface area density distribution.

4.5.2 CIMS Detection Sensitivities

Dilute mixtures of NO_2 were injected into the flow tube with no other gases and no aerosols present and the NO_2^- signal was monitored. The sensitivity for NO_2 can be estimated from a linear plot of NO_2^- signal (monitored at m/z 46) vs. [NO_2], as shown in Figure 4.3. The estimated sensitivity for NO_2 was $1.0x10^8$ molecule cm^{-3}. Previous experiments studying OH gas-phase chemistry using CIMS found similar senstitivities.[111] Note that the background signal for m/z 46, measured in the absence of any NO_2, was approximately 2000 counts per second.

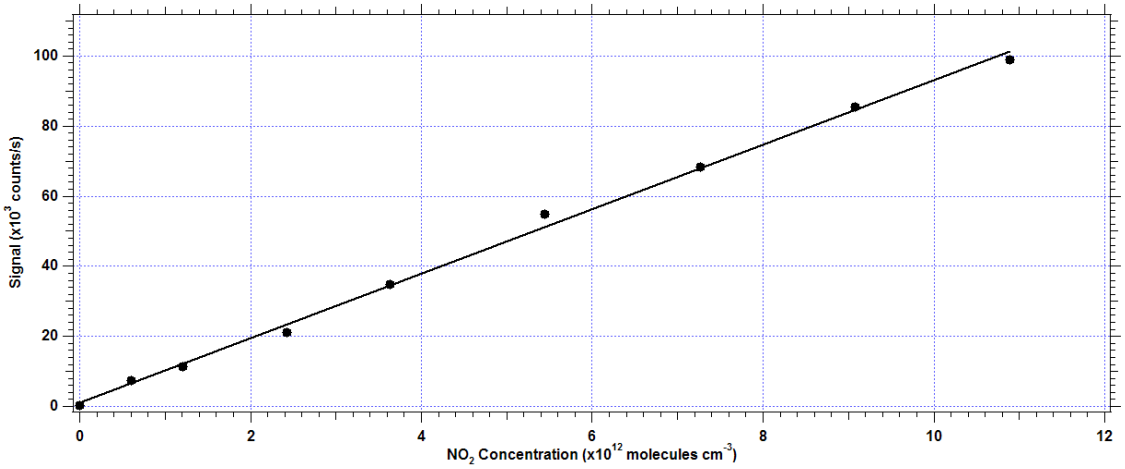

Figure 4.3: NO_2 sensitivity plot.

4.5.3 Hydroxyl Radical Calibration

Standard methods for calibrating a CIMS system for OH involve time as a variable.[130] However, since the current system has a fixed interaction time these methods could not be applied. The actual calibration of the system to OH was not necessary since the calculations involved relative values of the concentrations (see below). Therefore, the signal response could be used in its place. For reference, Canosa-Mas & Wayne (1990)[130] found a sensitivity of their CIMS system to be $5x10^9$ molecules cm^{-3} s^{-1}, while Bacak (2004)[111] generated an extremely sensitive system with a sensitivity of $1x10^7$ molecules cm^{-3} s^{-1}.

4.5.4 Hydroxyl Radical Signal-to-Noise

Figure 4.4 shows the peak intensity for m/z 17, corresponding to OH. From the graph, the peak intensity for OH was on the order of 12000 to 13000 counts per second under normal operating conditions for generating OH, as listed in Section 4.4.1. The root mean square of the background signal in this region of the mass spectrum was approximately 335 counts per second. Therefore, the signal-to-noise ratio for OH was on the order of 36 to 39, indicating that the OH peak is easily seen above the noise of the mass spectrometer system.

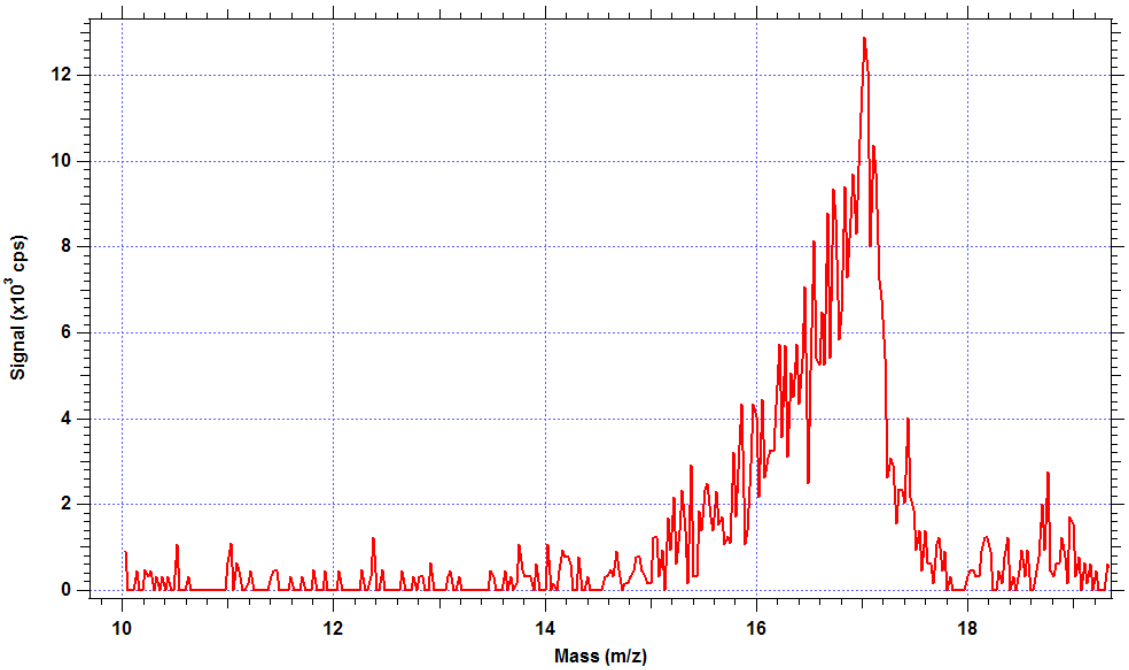

Figure 4.4: Mass spectrum peak intensity for m/z 17 (OH).

4.6 Uptake Coefficient Determination

As discussed in Chapter 3, most heterogeneous flow tube approaches calculate uptake coefficients by generating a plot of reactant concentration (C) versus reaction time (t). Assuming a first order reaction between the wall of the flow tube and the reactant of interest with rate coefficient k (s^{-1}), the rate of change of reactant concentration can be written as

$$\frac{dC}{dt} = -kC \qquad \text{Eq4.1}$$

Integrating this equation over the reaction time yields

$$\ln\left(\frac{C}{C_o}\right) = -kt \qquad \text{Eq4.2}$$

Therefore, a plot of $ln(C/C_o)$ versus t yields a slope equal to the first order rate coefficient. Due to radial concentration inhomogeneities at the leading end of the flow tube, a correction is often

applied to k to calculate the "true" rate coefficient, k_t. This formulation was given by Brown (1978)[108] and is commonly used in flow tube studies.

For a coated-wall flow tube experiment, the rate coefficient is related to the uptake coefficient by Eq4.3.

$$\gamma_{meas} = \frac{2rk}{u_{av}} \qquad \text{Eq4.3}$$

where r is the radius of the flow tube (m) and u_{av} is the mean thermal speed of the molecules (m s^{-1}). However, for an aerosol flow tube the uptake coefficient is calculated by using Eq4.4

$$\gamma_{meas} = \frac{4k}{Su_{av}} \qquad \text{Eq4.4}$$

where S is the surface area density of the aerosol (m^{-1}) and u_{av} is, again, the mean thermal speed of the molecules (m s^{-1}).

For the current study, the reaction time for all reactions was fixed based on flow and a static inlet position. The variable that was altered during experiments was the surface area density, such that the concentration of the reactant is measured as a function of surface area density of the reacting aerosol. This allowed the measured uptake coefficient, γ_{meas}, to be determined directly from a plot of the concentration versus the surface area density.

Due to the parabolic velocity profile of the bulk gas, the interaction time of OH with the wall was longer than the interaction time with the aerosol; therefore, three times were defined for the system. The initial time, t_0, corresponding to an initial OH concentration, C_0, entering the system. The time for reaction between OH and the aerosol can be defined as t_1, and is equal to 82.5 ms. Finally, the time for interaction between OH and the wall of the flow tube was defined as t_2, and was on the order of 300 ms. Let C_2 define the final concentration of OH after reaction for the total reaction time (t_2) for both systems (with and without aerosols present).

Considering only loss to the flow tube wall, the rate equation can be written and integrated as

$$\frac{dC}{dt} = -k_w C \qquad \text{Eq4.5}$$

$$\int_{C_0}^{C_2^{wall}} \frac{dC}{C} = -k_w \int_{t_0}^{t_2} dt \qquad \text{Eq4.6}$$

$$\ln\left(C_2^{wall}\right) - \ln(C_0) = -k_w(t_2 - t_0) \qquad \text{Eq4.7}$$

$$\ln\left(\frac{C_2^{wall}}{C_0}\right) = -k_w t_2 \qquad \text{Eq4.8}$$

where k_w is the reactive wall loss rate coefficient (s^{-1}). When reaction with the aerosol is present the rate equation can be written as

$$\frac{dC}{dt} = -k_a C - k_w C \qquad \text{Eq4.9}$$

$$\int_{C_0}^{C_2} \frac{dC}{C} = \int_{t_0}^{t_2} (-k_a - k_w) dt \qquad \text{Eq4.10}$$

where k_a is the rate coefficient (s^{-1}) for reaction with the aerosol surface. Splitting the integrals based on the times for reaction leads to

$$\int_{C_{t_0}}^{C_{t_1}} \frac{dC}{C} + \int_{C_{t_1}}^{C_{t_2}} \frac{dC}{C} = \int_{t_0}^{t_1} (-k_a - k_w) dt + \int_{t_1}^{t_2} (-k_a - k_w) dt \qquad \text{Eq4.11}$$

But k_a is zero during the time interval t_1 to t_2. Therefore, Eq4.11 simplifies to

$$\int_{C_{t_0}}^{C_{t_1}} \frac{dC}{C} + \int_{C_{t_1}}^{C_{t_2}} \frac{dC}{C} = \int_{t_0}^{t_1} (-k_a - k_w) dt + \int_{t_1}^{t_2} (-k_w) dt \qquad \text{Eq4.12}$$

$$\ln\frac{C_1}{C_0} + \ln\frac{C_2^{aerosol}}{C_1} = (-k_a - k_w)(t_1 - t_0) + (-k_w)(t_2 - t_1) \quad \text{Eq4.13}$$

Combining the left-hand side of Eq4.13, and substituting $t_0 = 0$, simplifies the expression to

$$\ln\left(\frac{C_2^{aerosol}}{C_0}\right) = (-k_a - k_w)(t_1) + (-k_w)(t_2 - t_1) \quad \text{Eq4.14}$$

Expanding the right-hand side yields

$$\ln\left(\frac{C_2^{aerosol}}{C_0}\right) = -k_a t_1 - k_w t_1 - k_w t_2 + k_w t_1 \quad \text{Eq4.15}$$

$$\ln\left(\frac{C_2^{aerosol}}{C_0}\right) = -k_a t_1 - k_w t_2 \quad \text{Eq4.16}$$

$$\ln\left(C_2^{aerosol}\right) = -k_a t_1 - k_w t_2 + \ln(C_0) \quad \text{Eq4.17}$$

Using Eq4.8, an expression for C_0 can be substituted into Eq4.17

$$\ln(C_0) = \ln\left(C_2^{wall}\right) + k_w t_2 \quad \text{Eq4.18}$$

$$\ln\left(C_2^{aerosol}\right) = -k_a t_1 - k_w t_2 + \ln\left(C_2^{wall}\right) + k_w t_2 \quad \text{Eq4.19}$$

Therefore,

$$\ln\left(\frac{C_2^{aerosol}}{C_2^{wall}}\right) = -k_a t_1 \quad \text{Eq4.20}$$

where $C_2^{aerosol}$ is the final OH concentration after reaction with both the wall and the aerosol surface (C_n determined from mass spectrometer signal), C_2^{wall} is the final OH concentration after reaction with only the flow tube wall (C_w determined from mass spectrometer signal), and t_1 is the time for reaction with the aerosol surface (82.5 ms). Eq4.20 can then be rewritten as

$$\ln\left(\frac{C_n}{C_w}\right) = -k_a t \quad \text{Eq4.21}$$

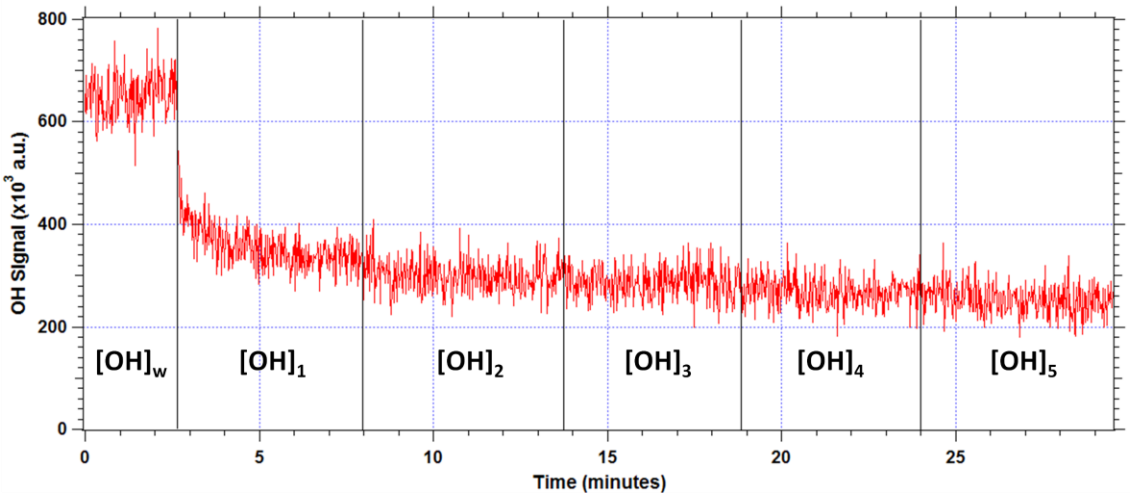

Figure 4.5: Response of OH signal during standard uptake experiment on oleic acid aerosols. Vertical lines correspond to increase in aerosol number density.

An expression for the heterogeneous rate coefficient, k_a (Eq4.22), can be substituted into Eq4.21.

$$k_a = \frac{\gamma u_{av} S}{4} \qquad \text{Eq4.22}$$

where γ is the uptake coefficient for OH on an oleic acid surface, u_{av} is the molecular velocity of OH (m s^{-1}), and S is the surface area density of the aerosol (m^{-1}). Therefore, Eq4.21 simplifies to

$$\ln\left(\frac{C_n}{C_w}\right) = -\frac{\gamma u_{av} t}{4} S \qquad \text{Eq4.23}$$

Graphing ln(C_n/C_w) versus S using Eq4.23 yields a graph whose slope is proportional to the uptake coefficient. This analysis assumed that the radial concentration of OH was uniform across the flow tube. This assumption was verified by the CFD simulations (Figure 3.21) that indicated a uniform injection of OH across the flow tube. Furthermore, since the walls of the flow tube were coated with halocarbon wax, reactive loss of OH to the walls of the flow tube was expected to be negligible over the course of the reaction timescale since the uptake coefficient of OH on the wax is very small.[63;131] Therefore, this uptake coefficient is the measured uptake coefficient and, unlike other flow tube studies, did not need to be corrected for diffusional

processes to yield the true uptake coefficient, γ_t. Suggesting that in the experiments outlined here, $\gamma_{meas} = \gamma_t$.

Figure 4.5 displays the typical response of the OH signal due to the presence of aerosols. At time t = 0, no aerosols were present and the initial OH signal was obtained. After some time, aerosols are introduced into the system (t = 2.5 minutes). The slow decay of the OH signal seen upon first introducing the aerosol to the system (t = 2.5 – 6 minutes in Figure 4.5) was due to the time required for the nebulizer to establish a constant flow of aerosol through the flow tube. When the OH signal was observed to be stable for approximately two minutes, the flow of oleic acid through the nebulizer was increased, indicated by vertical lines in Figure 4.5. This resulted in an increase in the aerosol number density (and surface area density) and a subsequent drop in the OH signal. The last two minutes of each time interval were averaged to determine the response of OH to the given surface area density, S_i. A time interval of two minutes was chosen to minimize the total time required for a given experiment. Given the flow rate and number density of the aerosol, a thin film of oleic acid was observed on the first pinhole plate of the mass spectrometer after experimental times of 30 to 45 minutes. This film could block the first pinhole and lower detection efficiencies. More importantly, however, this film could act as another surface for OH to react with obscuring the true uptake and loss of OH by the aerosol surface. Each response, as $ln([OH]_n/[OH]_w)$, was then plotted against the corresponding surface area density. A typical experiment would yield four to five data points of OH signal response versus total surface area.

Figure 4.6 shows a plot of $ln([OH]/[OH]_w)$ vs. the aerosol surface area density for all data obtained over four different experiments carried out on four different days. The agreement between the different experiments was extremely good and was an indication of the excellent stability of the system. The error associated with the x-axis corresponded to ±5% of the total

retrieved surface area density, as discussed in the previous chapter, while the error associated with the y-axis was due to the propagation of the errors in the averaging of the OH signal. Fitting all the data in Figure 4.6 to a straight line yields a measured uptake coefficient of 0.494 ± 0.083.

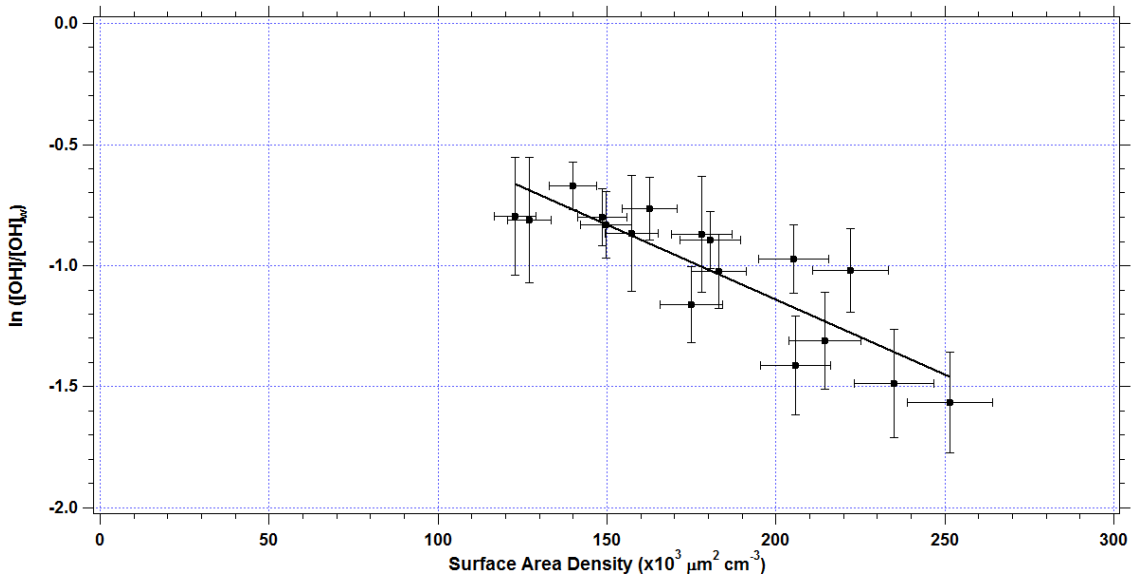

Figure 4.6: OH uptake data for all experiments conducted on oleic acid aerosols.

To ensure that the observed surface areas had no dependence on the size of the aerosol particles, the total surface area was plotted against total number density of the aerosol produced. If the total surface area density had any dependence on the size of the particles, then large surface area densities would be observed for small number densities. As seen in Figure 4.7, the total surface area was linearly dependent on the total number density of particles. This suggested that the increase in surface area was only due to the presence of a higher number of particles, and not due to the presence of larger particles.

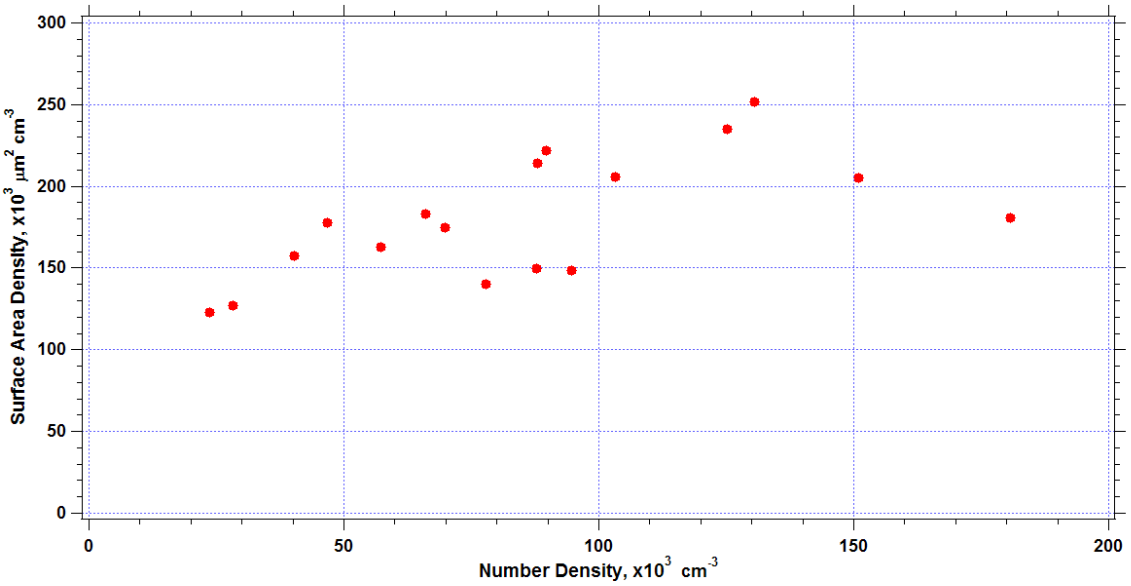

Figure 4.7: Dependence of total surface area density on the number density of oleic acid particles produced.

Table 4.1 summarizes the work done to date regarding uptake of OH on organic surfaces. The uptake coefficient of 0.494 ± 0.083 obtained in this work agrees quite well with many of the studies conducted to date. In fact, by comparing the structure of the different organics studied, it can be shown that a value of 0.5 is expected for oleic acid. Figure 4.8 shows the molecular structures for all compounds listed in Table 4.1 (excluding motor oil, diesel fuel and perfluorinated polyether (PFPE)).[132] It can be immediately seen that except for the presence of the double bond, the structure of oleic acid is very similar to stearic acid, which is the saturated analog of oleic acid. As stated in Chapter 1, alkenes can react with OH by hydrogen abstraction and that the importance of this reaction over that of addition to the double bond increases with increasing chain length.[5] For a C_{18} molecule with only one double bond, H-abstraction could be as important a reaction pathway for OH as addition to the double bond. Therefore, finding γ_{oleic} slightly larger than $\gamma_{stearic}$ is not an unreasonable result for C_{18} molecules.

Table 4.1: Summary of organic heterogeneous studies.

Authors	Surface	Technique	Surface Type	γ
Lambe et al. (2009)[71]	motor oil	smog chamber, relative rate approach	aerosol	3.5 ± 0.7
	diesel fuel/motor oil		aerosol	13 – 40
Che et al. (2009)[70]	squalene	continuous flow stirred tank reactor	aerosol	0.51 ± 0.1
Smith et al. (2009)[69]	squalene	aerosol flow tube	aerosol	0.3 ± 0.07
Bagot et al. (2008)[64]	squalene	vacuum chamber	liquid surface	0.49 ± 0.04
	PFPE		liquid surface	--
McNeill et al. (2008)[68]	palmitic acid	aerosol flow tube	pure aerosol	0.8 - 1
George et al. (2007)[66]	bis(2-ethylhexyl) sebacate	aerosol flow tube	aerosol	1.3 ± 0.4
Lambe et al. (2007)[67]	n-hexacosane	smog chamber, relative rate approach	aerosol	1.04 ± 0.21
Hearn & Smith (2006)[65]	methyl oleate	flow tube, relative rate approach	aerosol	1.12 ± 0.36
	bis(2-ethylhexyl) sebacate		aerosol	2
Molina et al. (2004)[33]	octadecyltrichlorosilane	coated-wall flow tube	film	>0.2
	paraffin wax		film	>0.2
	pyrene wax		film	>0.2
Bertram et al. (2001)[63]	paraffin wax	coated-wall flow tube	solid surface	0.34
	stearic-palmitic acid		solid surface	0.32
	soot		solid surface	0.88
	pyrene		solid surface	0.32
	halocarbon wax		solid surface	0.0006
Jech et al. (1982)[110]	malonic acid	aerosol flow tube	aerosol	0.17 ± 0.034

The same argument can be made for palmitic acid ($C_{16}H_{32}O_2$), such that γ_{oleic} would also be slightly larger than $\gamma_{palmitic}$. McNeill et al. (2008)[68] found a larger uptake coefficient for palmitic acid than the current study. The discrepancy in uptake values is most likely associated with the different techniques used in each study. McNeill et al. measured uptake coefficients by monitoring the loss of palmitic acid in the aerosol. This method does not take into account possible secondary chemistry occurring between palmitic acid molecules after the palmitic acid

has reacted with OH. The presence of this secondary chemistry would lead to an observed γ greater than the true uptake coefficient. This would suggest that $\gamma_{palmitic}$ is actually less than 0.8, in better agreement with the current study.

Similar comparisons can be made to the other molecules studied; however, since many of those studies involved relative rate approaches the calculated uptake values are greater than one. Therefore, a direct comparison of γ values cannot be done. A qualitative comparison between oleic acid and many of the other molecules finds that γ_{oleic} is expected to be smaller than γ for the other organic compounds based on structural reactivity. Compounds such as n-hexacosane ($C_{26}H_{54}$) and octadecyltrichlorosilane ($C_{18}H_{37}Cl_3Si$) having no double bonds can only react via H-abstraction and would be expected to be as reactive or only slightly more reactive than oleic acid due to the presence of more abstraction sites. For compounds like squalene ($C_{30}H_{50}$) and pyrene ($C_{16}H_{20}$) the presence of a large number of double bonds would lead to a higher reactivity towards OH than saturated organic molecules. It is possible that the reactivity of squalene and pyrene could be comparable to oleic acid due to the reactivity of the double bonds, as seen by $\gamma_{squalene}$ = 0.3 – 0.5. Methyl oleate ($C_{19}H_{36}O_2$) and bis(2-ethylhexyl) sebecate (BES, $C_{26}H_{50}O_4$) might be expected to have larger uptake coefficients due to the presence of electron withdrawing groups that can stabilize resulting carbon anions after loss of a H to OH.

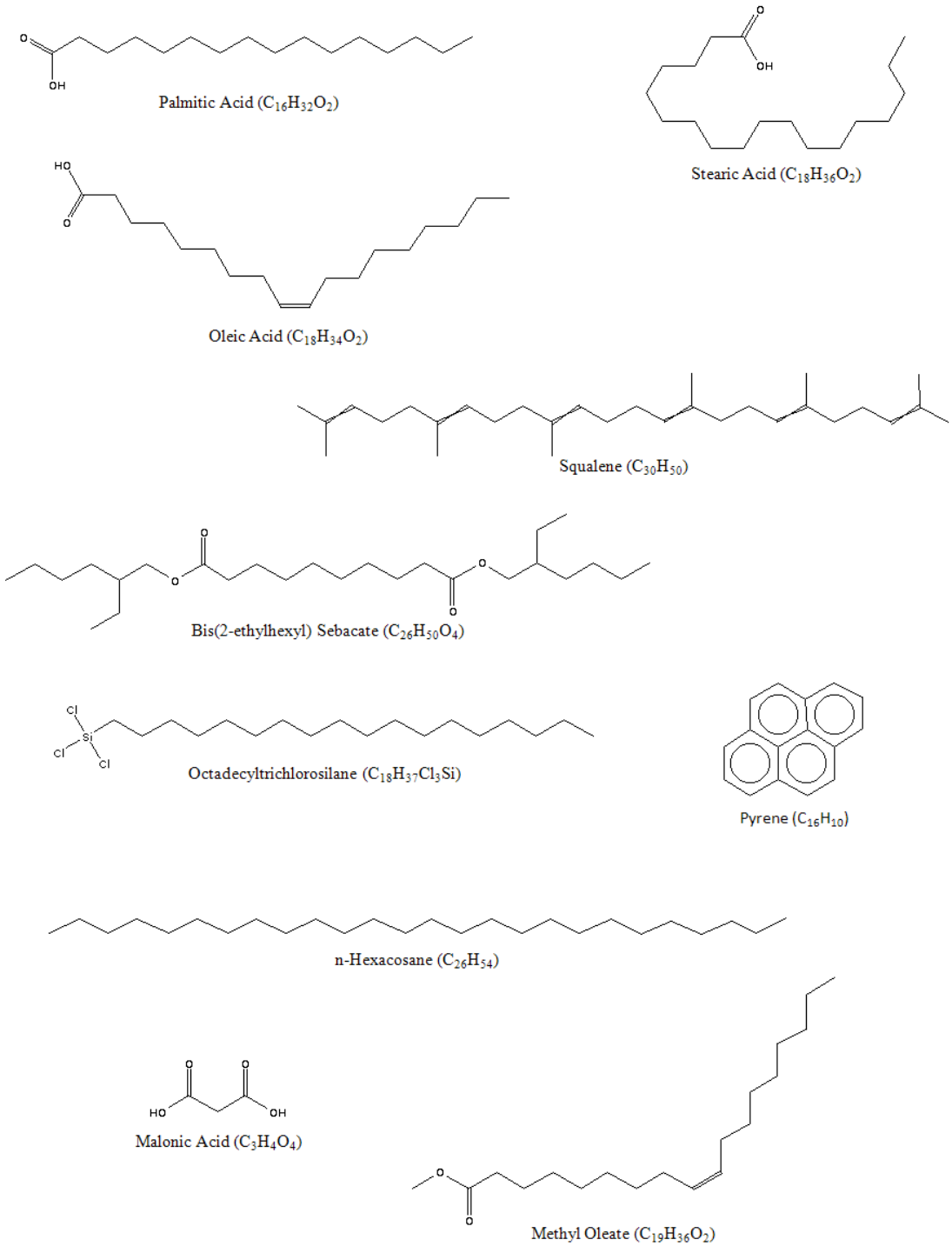

Figure 4.8: Structure of various organics used in heterogeneous uptake work.[132]

It is interesting to note, however, that Smith et al. (2009)[69] have suggested that if the data of George et al. (2007)[66] are fit to an exponential function the uptake coefficient of OH on BES particles is actually 0.23 and not 1.3 as initially reported. They also suggest that the uptake coefficient measured by McNeill et al. (2008)[68] for OH on palmitic acid particles should be lower than the reported 0.8 – 1 when the data are fit with an exponential, and should in fact fall between 0.28 – 0.39, again in reasonable agreement with the value reported here. Therefore, the raw data measured by George et al. and McNeill et al. are similar to what is reported here, and the differences in the uptake coefficients result in part from the fitting procedure used to compute the uptake coefficient.

In addition, Bagot et al. (2008)[64] recently reported OH to be 0.49 ± 0.04 for the reaction of superthermal OH on a squalane surface at low pressure. The slightly larger value for OH from this measurement is potentially due to the increased translational energy of the OH radicals resulting in a larger reaction probability. These arguments would suggest that the uptake coefficient for OH on any organic surface does not vary greatly regardless of molecular reactivity (i.e. $0.3 < \gamma_{organic} < 0.5$).

The good agreement between uptake coefficients for organics of different structure could suggest a common rate limiting step. Reaction between organics and OH in the gas-phase occurs quite quickly with bimolecular rate coefficients, k^{II}, on the order of 10^{-12} cm^3 $molecule^{-1}$ s^{-1}. If the bulk-phase chemistry is similar and also occurs quickly, these results could suggest that OH uptake on organic particles of any kind is limited by mass accommodation (see Section 2.3.2). This would then suggest that the value reported here, and in the literature, is more accurately the mass accommodation coefficient.

4.7 Phenomenological Interpretation

Using Eq2.37 & Eq2.38, the uptake process can be examined on a molecular level. Firstly, the measured uptake coefficient can be corrected for diffusion to the particle surface via Eq2.38. This correction yields the reactive uptake coefficient, γ_{react}. Using Eq2.4 to calculate $1/\Gamma_{diff}$ yields an extremely small correction to γ_{meas} such that $\gamma_{react} = 0.497$. The reactive uptake coefficient can then be analysed based on its surface and bulk processes using Eq2.37, shown again here for reference.

$$\frac{1}{\gamma_{react}} = \frac{1}{\alpha} + \frac{u_{av}}{4}\left[\frac{\beta k k_{ads}}{k_{des}} - HRT\sqrt{D_l}\left(\sqrt{k} + \sqrt{\frac{1}{\pi t}}\right)\right]^{-1} \qquad \text{Eq2.37}$$

This analysis requires known values for some or all of the variables listed in Table 4.2. Even if all the variables are not known, ranges of values can be used to suggest the importance of the different processes. To make matters easier Eq2.37 can be simplified with a few simple substitutions.

Table 4.2: Variables required for molecular-level description of uptake.

Variable	Description
α	mass accommodation coefficient
β	ratio of surface excess to bulk concentration
k	bulk-phase rate coefficient (s^{-1})
H	Henry's Law Coefficient (m^3 atm $molecule^{-1}$)
D_l	bulk-phase diffusion coefficient (m^2 s^{-1})

First, the Henry's Law constant ($H'=HRT$) has be shown to simplify to an expression involving the adsorption coefficient (k_{ads}), the desorption rate coefficient (k_{des}), the mass accommodation coefficient (α) and the interfacial thickness (δ).[80;82]

$$HRT = \frac{k_{ads}\,\alpha}{k_{des}\,\delta} \qquad \text{Eq4.24}$$

with k_{ads} in units of m s^{-1}, k_{des} in units of s^{-1} and δ in units of m. Substituting this into Eq2.37 yields

$$\frac{1}{\gamma_{react}} = \frac{1}{\alpha} + \frac{u_{av}}{4}\left[\frac{\beta k k_{ads}}{k_{des}} - \frac{k_{ads}\,\alpha}{k_{des}\,\delta}\sqrt{D_l}\left(\sqrt{k} + \sqrt{\frac{1}{\pi t}}\right)\right]^{-1} \qquad \text{Eq4.25}$$

Hanson (1997)[80] showed that $k_{ads} = Su_{av}/4$. Furthermore, since the particle of interest is a pure organic particle, the ratio of surface to bulk concentration (β) can be assumed to be unity. Gross et al. (2009)[133] suggested that the uptake of NO_3 (and N_2O_5) for various organic compounds was irreversible. This would imply that the sticking coefficient, *S*, for these molecules is unity and can be applied to OH. This is further validated by the findings of Vieceli et al. (2005)[134] and Roeselova et al. (2004)[135] who found that *S* approached unity for OH on a water surface. Incorporating these simplifications and rearranging the denominator in Eq4.25 yields

$$\frac{1}{\gamma_{react}} = \frac{1}{\alpha} + k_{des}\left[k - \frac{\alpha\sqrt{D_l}}{\delta}\left(\sqrt{k} + \sqrt{\frac{1}{\pi t}}\right)\right]^{-1} \qquad \text{Eq4.26}$$

Heijman et al. (1985)[136] found that the aqueous phase reaction between the linoleate ion ($C_{18}H_{31}O_2^-$) and OH had a bimolecular rate coefficient, k^{II}, of $1x10^{10}$ M^{-1} s^{-1}. Elliot and McCracken (1985)[137] found a rate coefficient for ethanol and OH in the bulk aqueous phase on the order of 10^9 M^{-1} s^{-1}. Therefore, assuming a rate coefficient of 10^{10} M^{-1} s^{-1}applies to pure oleic acid, the pseudo-first order rate coefficient, *k*, can be determined by multiplying k^{II} by the molar volume of oleic acid, yielding a rate coefficient of $3.15x10^{10}$ s^{-1}. The interfacial thickness, δ (m), for a gas-water interface is approximately 15 Å[138] and can be used as an approximate value for a

gas-organic interface. The diffusion coefficient of a species in a liquid is related to the viscosity through the Stokes-Einstein equation

$$D_l = \frac{k_B T}{6\pi\eta r} \qquad \text{Eq4.27}$$

where D_l is the diffusion coefficient ($m^2\ s^{-1}$), k_B is the Boltzmann constant ($m^2\ kg\ s^{-2}\ K^{-1}$), T is the temperature (K), η is the viscosity of the liquid ($kg\ m^{-1}\ s^{-1}$), and r is the radius of the diffusing species (m). The viscosity of oleic acid in the range of 293 – 298 K is 0.15 $kg\ m^{-1}\ s^{-1}$.[139] If the H-O bond length is used as an approximation for the diameter of OH, then the radius of OH is ~1 Å.[134] Using these values yields a diffusion coefficient of ~$10^{-10}\ m^2\ s^{-1}$.

The value of the uptake coefficient can now be evaluated over a range of desorption rate coefficients and mass accommodation coefficients via Eq4.26. Donaldson (1999)[140] calculated a desorption rate coefficient ranging from 10^9 to $10^{10}\ s^{-1}$ for ammonia on water. Donaldson and Anderson (1999)[141] predicted desorption rate coefficients of $10^6 – 10^8\ s^{-1}$ for C_1-C_4 organics on water. Estimated rate coefficients for desorption of OH on water are on the order of $10^8 – 10^{10}\ s^{-1}$.[135;142] Therefore, γ can be calculated for k_{des} values within this range ($10^5 – 10^{11}\ s^{-1}$) and α values between 0.5 and 1. Note that if α is less than 0.5, k_{des} would have to be negative for Eq4.12 to hold; therefore, 0.5 is the lower limit for α.

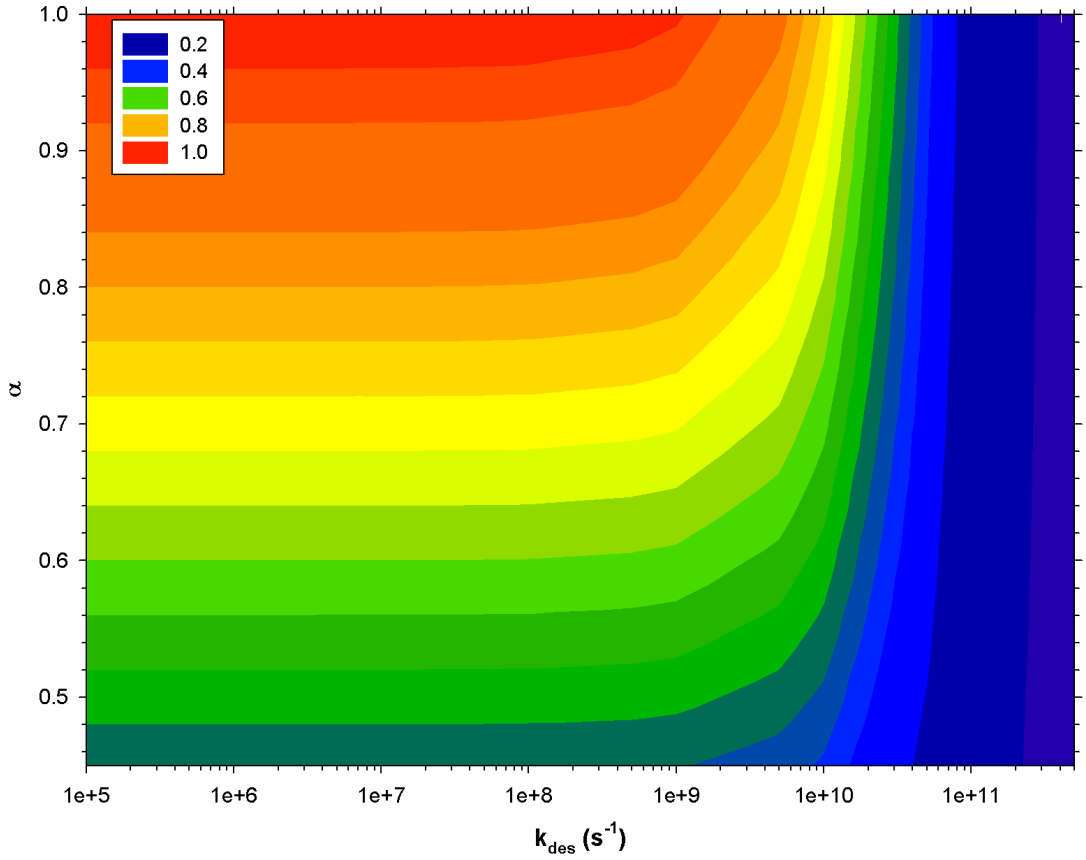

Figure 4.9: Determination of uptake coefficient by varying α and k_{des}. Legend indicates calculated value of γ.

Figure 4.9 shows the values of γ for the given ranges of α and k_{des} calculated using Eq4.26. From the graph it can be seen that for values of k_{des} less than 10^{10} s^{-1}, the mass accommodation coefficient must approach 0.5 for γ to equal 0.5. Only as k_{des} approaches 10^{10} s^{-1} can α approach unity. However, since most literature data suggests that k_{des} for OH would be less than 10^{10} s^{-1} estimating α as 0.5 seems more likely. This result is not entirely unexpected since it has already been stated that in the presence of fast reactions and/or fast bulk-phase diffusion $\gamma_{meas} \approx \alpha$. The results obtained in this study would then suggest that the mass accommodation coefficient of OH on an organic surface is ~0.49 ± 0.08. This would also agree with the

qualitative argument that all uptake on organic surfaces is limited by the same processes, presumably mass accommodation.

4.8 Atmospheric Implications

4.8.1 Atmospheric Chemistry

The influence of aerosols on the chemistry of the lower atmosphere depends on both the aerosol composition and make-up of the surrounding atmosphere.[38-40;43-50] Di Carlo et al. (2004)[41] measured OH reactivity in an unpolluted forested region at the University of Michigan Biological Station (UMBS) in northern Michigan and found that their calculated reactivity from OH observations was underestimated by a model that included only gas-phase chemistry. They determined that an average reactivity of $2.6 \pm 1.0\ s^{-1}$ was missing from their model. They inferred from their data that the missing reactivity was simply from unmeasured BVOCs not included in the gas-phase chemistry of their model. While measuring BVOC fluxes at UMBS, Ortega et al. (2007)[42] suggested that the inclusion of more reactive gas-phase chemistry had no physical basis since their measured levels of BVOCs did not match that required by the Di Carlo et al. measurements to account for the missing reactivity. Ortega et al. concluded that the inability of Di Carlo et al. to correctly model OH concentrations may imply the presence of important heterogeneous chemistry.

Using the value of the uptake coefficient found in the current study and size distributions common to the UMBS site, the contribution of heterogeneous chemistry to the missing reactivity can be estimated. Slade (2009)[143] made measurements of aerosol size distributions in the range of 0.015 to 0.750 μm, and estimated the presence of particles as large as 4 μm in diameter. Using these distributions as a starting point, estimates of rate coefficients for the reaction of OH and the particle surface can be made using Eq4.22. When considering only the size distributions between

0.015 to 0.750 μm, heterogeneous chemistry would account for less than 1% of the missing reactivity. However, heterogeneous reactivity could account for upwards of 5% or more of the missing reactivity if larger sized particles (diameter > 2 μm) are present as suggested by Slade. Particles as large as 10 μm were also found in a forest of similar vegetation (mixed coniferous/deciduous) in Hungary.[144] Since surface area is dependent on the square of the radius, micron-sized particles contribute a large fraction of the total surface area, meaning that only a small number of particles are needed for heterogeneous chemistry to become significant. This calculation assumes that the uptake coefficient will have a consistent value of 0.5 for all particle sizes. However, diffusion limitations ($1/\Gamma_{diff}$) of OH to the particle surface can be significant for particles in the micrometer size range according to Eq2.4, which can drastically lower the overall rate coefficient at ambient atmospheric conditions. Therefore, this data would suggest that heterogeneous chemistry on organic particles would only account for a few percent of the missing reactivity at the UMBS site.

Another approach for determining the potential importance of heterogeneous chemistry for the OH budget is to compare the rate coefficients for reaction of OH with aerosols and with carbon monoxide. Since reaction with CO is considered the main removal mechanism for OH[3] then comparing the magnitude of rate coefficients will give a measure of the importance of heterogeneous chemistry. Cooper et al. (2001)[145] classified the meteorology and composition of air masses at UMBS based on the source of the air masses. They determined that most flow reaching the UMBS forest originated either from the northwest or southwest. They also found that north-westerly flow, originating over the Canadian prairies, was typically characterized by low levels of CO (100 – 200 ppbv) and O_3 (20 – 40 ppbv), while south-westerly flow, originating around the Chicago area, was characterized by higher levels of CO (200 – 300 ppbv) and O_3 (40 – 100 ppbv). Baulch et al. (1992)[146] listed a bi-molecular rate coefficient for OH+CO of 1.25×10^{-13}

cm^3 $molecule^{-1}$ s^{-1}. Multiplying this rate coefficient by the range of CO values will yield pseudo-first order rate coefficients that can be compared to the calculated heterogeneous rate coefficients. Therefore, under north-westerly flow, the pseudo-first order rate coefficient for reaction between OH and CO would range from 0.308 – 0.615 s^{-1}, while the range under south-westerly flow would be 0.615 – 0.923 s^{-1}. According to the distributions from Slade (2009)[143], the heterogeneous rate coefficient for reaction between OH and organic aerosols would range from 0.003 – 0.01 s^{-1} when using an uptake coefficient of 0.5. These numbers suggest that under clean north-westerly flow reaction with the aerosol surface could contribute to the overall loss process for OH at the UMBS forest, albeit a small fraction of the overall loss. However, under south-westerly flow heterogeneous chemistry would likely not be important since the chemistry with CO would dominate.

These calculations do not provide conclusive evidence that heterogeneous chemistry could contribute to the budget of OH radicals; however, they do suggest that under the right conditions heterogeneous chemistry could be important. It is speculated that the importance of this chemistry will decrease in more polluted air masses where the gas-phase loss of OH is expected to dominate.[38-40] However, in relatively clean environments, like that at UMBS, the presence of organic particles could significantly enhance the loss of OH via heterogeneous reactions. Field measurements simultaneously measuring OH reactivity and aerosol size distributions up to 10 μm would be required to conduct more rigorous calculations and make any definitive conclusions.

4.8.2 Atmospheric Oxidation of Oleic Acid Particles

Due to the presence of the double bond, alkenes are susceptible to attack by O_3 and NO_3, in addition to reaction with OH radicals. In fact, gas-phase reactions of alkenes with ozone are competitive with the daytime oxidation by OH radicals.[5] Using the uptake coefficient determined

in the current study, the relative importance of oxidation of oleic acid particles by various oxidants can be determined. While in the atmosphere, these organic particles, and organic surfaces, can be modified by reactions with atmospheric oxidants such as O_3, NO_3, and OH.[147] These heterogeneous reactions are expected to change the hygroscopicity and toxicity of these organic particles and organic surfaces.[89;103;105]

To determine the relative importance of the various oxidants the variable γ x [*oxidant*] has been suggested as a more relevant parameter compared with just γ.[148] Gross et al. (2009)[133] found that γ_{NO3} for oleic acid was >0.07 and a number of studies[149-152] have found γ_{O3} to be on the order of 10^{-3}. Using average atmospheric concentrations of 50 pptv (~10^9 molecules cm^{-3}) for NO_3, 0.06 pptv (~10^6 molecules cm^{-3}) for OH, and 50 ppbv (~10^{12} molecules cm^{-3}) for O_3, γ x [*oxidant*] values can be tabulated.[6] Table 4.3 shows that for daytime chemistry the oxidation of oleic acid particles proceeds primarily by reaction with O_3. Even if γ_{OH} for oleic acid were unity, the ozone/oleic acid particle reaction would still be almost three orders of magnitude more reactive. It should be noted, however, that O_3 will only react with a particle if it contains molecules that contain a double bond, therefore possibly lowering its contribution to the oxidation of ambient organic particles.

Table 4.3 also highlights the potential importance of oxidation by NO_3 at night. At standard atmospheric concentrations the rate of reaction with NO_3 is only one order of magnitude lower than that with O_3 and three orders larger than with OH. This suggests that heterogeneous oxidation by NO_3 could potentially compete with O_3, and be more important than OH. These results agree with other studies suggesting the importance of NO_3 oxidation over that of OH.[148]

Table 4.3: Reactivity of oleic acid particles towards different oxidants.

Oxidant	Concentration (molecule cm^{-3})	γ	γ x [*oxidant*] (molecules cm^{-3})
OH	10^6	0.5	$5x10^5$
O_3	10^{12}	10^{-3}	$1x10^9$
NO_3	10^9	0.1	$1x10^8$

Another way to examine the importance of heterogeneous reactions is to calculate the lifetime of an aerosol for reaction with OH, O_3, and NO_3. This analysis is similar to that used by Robinson et al. (2006)[53] and Gross et al. (2009)[133] to determine the effect of heterogeneous reactions on aerosol composition in a regional context. This analysis gives an estimate for the time needed to oxidize all the molecules in a particle. Following Robinson et al., the oxidation lifetime of a particle can be calculated using the following equation

$$\tau_{\text{liquid}} = \frac{4N_A r\rho}{3M\gamma u_{av}[oxidant]} \qquad \text{Eq4.28}$$

where τ_{liquid} is the oxidation lifetime of a single-component liquid particle (s), r is the particle radius (m), ρ is the particle density (assumed to be the density of the pure liquid) (kg m^{-3}), N_A is Avogadro's number, M is the molecular weight of the organic molecule (kg mol^{-1}), γ is the reactive uptake coefficient, [*oxidant*] is the concentration of the gas-phase oxidant of interest (molecules m^{-3}), and u_{av} is the average velocity of the oxidant in the gas phase (m s^{-1}). The concentration of the oxidants employed in this calculation was the same as those used in the calculations of γ x [*oxidant*] listed in Table 4.3. Figure 4.10 displays the lifetime of oleic acid particles ranging in size from 0.01 to 10 μm. From this simple calculation, it is again seen that the oxidation of oleic acid particles will proceed primarily by O_3, with oxidation by NO_3 being more important than OH. These results confirm the results found in Table 4.3.

Global 3D models of ^{210}Po estimate aerosol residence times in the troposphere on the order of 5 – 15 days[153], indicated in Figure 4.10 by dashed lines. This residence time is significantly longer than the oxidation lifetimes by both O_3 and NO_3, indicating that oleic acid particles would be significantly oxidized over their atmospheric lifetime. However, oxidation by OH is significantly slower than removal by deposition for particles larger than 0.5 – 1.0 μm in radius. Particles below this range would experience oxidation on timescales of less than a few days.

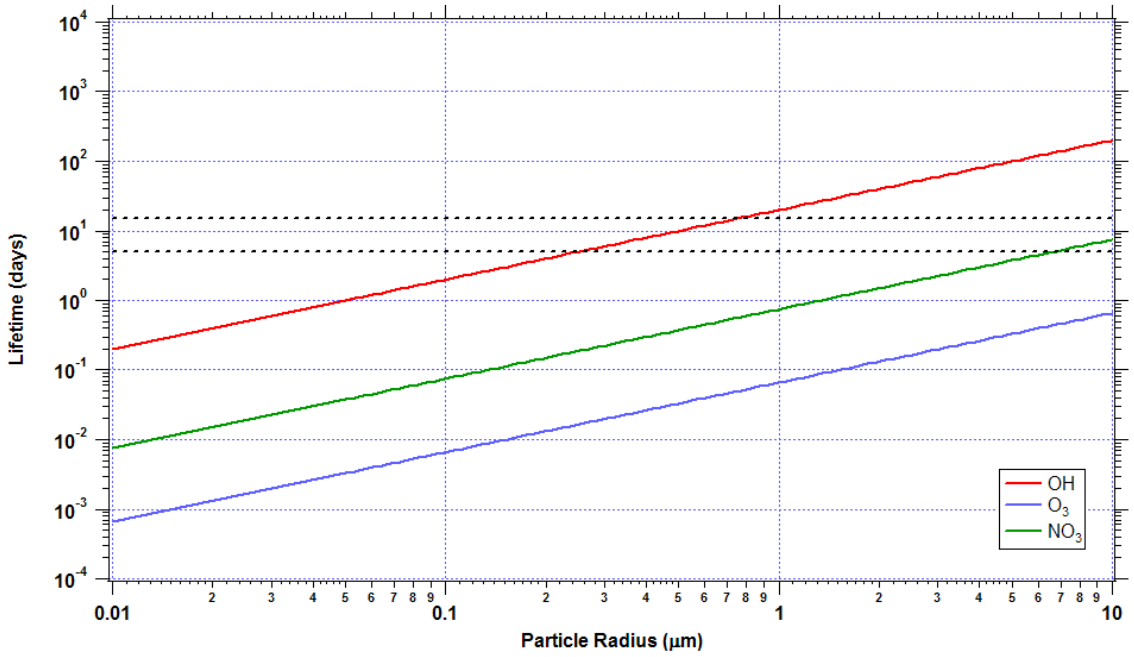

Figure 4.10: Atmospheric lifetimes of liquid oleic acid particles as a function of particle radius.

From the calculations above, oxidation of organic particles by O_3 and NO_3 is expected to be quick for all sizes of particles, while OH oxidation would only be important for particles less than 300 nm in radius. This would suggest that long-chain hydrocarbons, like oleic acid, initially found in aerosols would not be found in ambient aerosol data. However, several studies have found oleic acid in fairly high quantities in ambient aerosols[15;22;53;154], suggesting lifetimes of oleic acid on the order of days. One explanation for this discrepancy is that the presence of other

less reactive organic compounds slows the diffusion of fresh oleic acid to the surface of the particle where it is most likely to react. Several researchers have found that mixtures of liquid unsaturated oleic acid with solid saturated organic species, such as stearic acid, may slow the kinetics of chemical aging, particularly with regards to oxidation by ozone.[155-157] The effect can be considered to be two-fold. First, gas-phase oxidants will undergo slow diffusion in a solid organic matrix or in viscous liquids such as those that are super-cooled or structured.[155-157] Therefore, the reactive zone for oxidation may be confined to the particle surface or near-surface region[74;158] leading to differences in the transformation rates between the surface and bulk.[159] Second, trapping of oleic acid in or by the solid structure will limit renewal of oleic acid at the particle surface. This will limit the reactivity of oleic acid and increase the lifetime of particulate oleic acid. These results may explain the discrepancy in the short lifetime of oleic acid predicted by experimental data and the much longer lifetimes measured in ambient conditions. Unfortunately, this aspect of heterogeneous chemistry has not been thoroughly examined by laboratory studies.

4.9 Summary

The data presented in this chapter confirms the feasibility of using a low pressure aerosol flow tube (LP-AFT) for the study of heterogeneous OH reactions. The uptake coefficient obtained in this study agrees extremely well with current literature data. Furthermore the accuracy of this method is improved over that of the other laboratory measurements with a relative error of approximately 16%, compared to 20 – 35% for other experimental approaches. Using a LP-AFT method, an uptake coefficient of 0.49 ± 0.08 was found for OH on pure oleic acid particles. Using the molecular theory developed in Chapter 2, it is suggested that this value could be equivalent to the mass accommodation coefficient for OH on an organic particle.

For an uptake coefficient in this range, it is possible for heterogeneous chemistry to play a role in the overall tropospheric budget of OH under the right conditions. The value of the uptake coefficient suggests slow oxidation of particles greater than 1 μm in diameter, but particles with diameters less than 0.6 μm could experience significant oxidation by OH on timescales less than that of deposition.

Chapter 5
Conclusions and Future Work

5.1 Conclusions

The results presented in this work provide a new method for studying the kinetics of hydroxyl radical uptake on organic aerosols. Experiments were conducted to determine the most efficient approach to couple a low pressure aerosol flow tube (LP-AFT) to a chemical ionisation mass spectrometer (CIMS) (Figure 5.1). Through iterative experimentation the system was designed and used for the study of hydroxyl radical uptake on oleic acid particles.

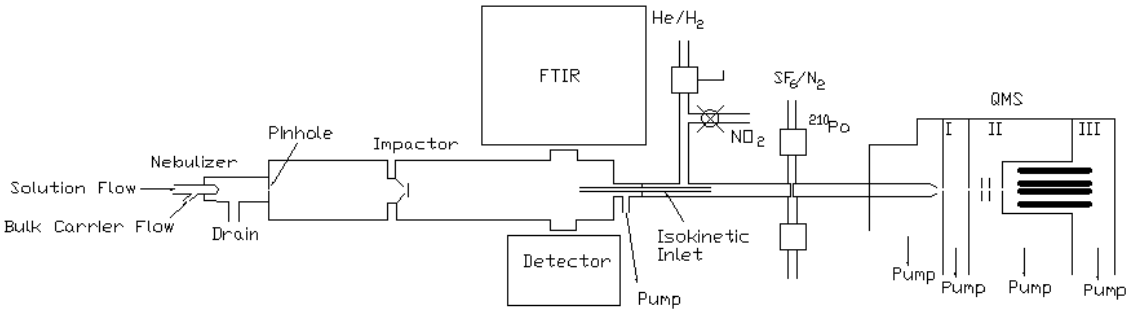

Figure 5.1: Schematic of design of LP-AFT coupled to CIMS system for the study of the kinetics of hydroxyl radical uptake.

At low pressures, the generation of the aerosol was hampered by a decrease in the efficacy of the aerosol source as well as the relatively fast flow of the carrier gas through the system. Therefore, a pinhole was used to generate a high pressure region of the flow tube where aerosols could be efficiently generated by a nebulizer. The nebulizer was operated at a pressure of 170 Torr with a gas flow rate of 1.0 SLPM. The relatively low flow of the nebulizer facilitated an increase in the aerosol concentration, which helped to improve the detection efficiency of the aerosol by increasing the observed signal in the FTIR. An optical cell with an internal diameter of 9.84 cm was employed for the detection of the aerosols. The large path length of the optical cell further increased the signal of the experimental spectrum. Particle sizes were controlled by

using an impactor designed to remove particles larger than 1.5 μm in diameter. The resulting size distributions had a smooth lognormal-like shape distributed around a radius of 400 nm.

Aerosol extinction spectra were determined using an FTIR system that sampled the experimental aerosol without disturbing the flow of the system. Aerosol size distributions were accurately retrieved by use of a characterization procedure that inverts an experimental spectrum into the corresponding aerosol size distribution. This method was extremely rigorous for single component particles, as well as internally mixed particles. The FTIR was found to be sensitive to aerosol number densities above $1x10^4$ particles cm^{-3} for oleic acid aerosols log-normally distributed at a radius of ~ 0.4 μm. The error for the total retrieved surface area for a given particle distribution was estimated to be less than 5%. The only limitation on the detection and quantification of aerosols is the knowledge of accurate optical constants. However, this is only a minor limitation since procedures exist for the simple determination of optical constants.[121;160-166]

A small portion of the bulk aerosol flow was sampled into the reactive section of the flow tube where the aerosol was exposed to hydroxyl radicals (OH). Radicals were generated by reacting hydrogen atoms (H), produced by passing H_2 through a microwave cavity, with nitrogen dioxide (NO_2). This reaction also produced nitric oxide (NO) as a by-product. Hydroxyl radicals interacted with the aerosol particles immediately after the particles entered this section of the flow tube. The heterogeneous reaction time was calculated to be 82.5 ± 2.5 ms.

Hydroxyl radicals were converted to hydroxyl anions (OH^-) by reaction with sulphur hexafluoride anion (SF_6^-) and detected with a quadrupole mass spectrometer in a three-stage differentially pumped vacuum chamber. A number of experiments were conducted to determine the design of the external ion optic plates that would result in the optimal signal-to-noise for the detected OH radicals. This involved investigating not only the appropriate size of the pinholes on the plates, but also testing the voltages applied to the plates. Further experiments determined that

a wire mesh attached to the back side of the first ion optic plate increased the detected signal of OH by acting as a guide for the ions into the mass spectrometer. Ions were detected with a multiplier assembly via negative ion counting. The signal-to-noise ratio for the OH peak in the mass spectrometer was calculated to be on the order of 36 – 39. All experiments are performed under dry conditions of 0% relative humidity.

The use of a low pressure aerosol flow tube to study the heterogeneous reaction between hydroxyl radicals and model atmospheric particles composed of oleic acid yielded an uptake coefficient of 0.49 ± 0.08. This result highlights the improved accuracy of the LP-AFT-CIMS system over other techniques currently in use for the study of hydroxyl radical heterogeneous chemistry. The overall error of the current study was calculated as 16%, while the studies highlighted in Table 4.1 have errors ranging from 20 to 35%. The combination of FTIR spectroscopy and chemical ionization mass spectrometry produces a powerful tool for the accurate determination of uptake coefficients on atmospherically relevant size distributions of model aerosols.

The uptake coefficient obtained in this study agrees extremely well with current literature data. A review of current literature data on the uptake of OH on organic surfaces suggests that the uptake coefficient for this process ranges from 0.3 to 0.5. Using the molecular theory developed in Chapter 2, it is estimated that the value of the mass accommodation coefficient approaches the measured uptake coefficient for atmospheric organic aerosols.

For an uptake coefficient in this range, it may be possible for heterogeneous chemistry to play a role in the overall tropospheric budget of OH under the right air quality conditions. The value of the uptake coefficient suggests slow oxidation of particles greater than 1 μm in diameter, but particles with diameters less than 0.6 μm could experience significant oxidation by OH on timescales less than that of deposition.

5.2 Future Work

The system designed and tested in this thesis provides the opportunity to investigate a wide variety of atmospheric heterogeneous issues. It has been suggested in the literature that the morphology of aerosols could influence the uptake of reactive trace species.[155-157] The experimental technique in this thesis provides the opportunity to study this aspect of heterogeneous chemistry. For example, stearic acid is a solid at room temperature; therefore the introduction of mixed oleic and stearic acid particles into the flow tube could probe the influence of particle phase on the uptake process. The only limitation to this procedure is that the optical constants for any material used to generate aerosols must be available. The optical constants of the different material must also be significantly different for the retrieval method to distinguish between the two substances. Studies of these mixed-phase systems could help explain discrepancies found between measured and estimated lifetimes of organics in atmospheric aerosols.

Furthermore, field observations have found that atmospheric organic aerosols become more oxidized with greater oxidant exposure and/or age and that oxidized species make up the majority of organic particulate matter.[23;24;53;167] Atmospheric particles have been found to consist of various mixtures of n-alkanoic acids, polycyclic aromatic hydrocarbons (PAHs), polycarboxylic acids and other oxygenated organics.[18;25;168-170] Since highly oxidized organics would have fewer sites for reaction with OH, it is possible that particles composed of these organics would exhibit a lower uptake of OH compared to more reactive organics, as exhibited in the study by Jech et al. (1982).[110] It would therefore be of interest to study aerosols composed of representative oxidized organics found in atmospheric aerosols. Future experiments with aerosols composed of mixtures of oxygenated and non-oxygenated organics would be more representative of atmospheric particles.

The uptake coefficients calculated from the data of McNeill et al. (2008)[68] seem to increase with decreasing particle diameter. The conclusion of the authors is that this trend is consistent with a gas-surface mechanism, since the surface area-to-volume ratio increases with decreasing particle size. The current design of the system also allows researchers to study the effect of particle size on uptake kinetics simply by changing the size of the impactor, and allowing larger particles to be sampled into the reactive portion of the flow tube. With the low operating pressures of the system, diffusion to the particle surface is fast even for particles as large as 10 μm in diameter. Therefore, these experiments could determine if uptake is influenced by particle diameter through a process other than diffusion.

References

1. R. P. Wayne, Chemistry of Atmospheres (Oxford University Press, Oxford; New York, ed. 3rd, 2000).

2. C. D. Ahrens, Meteorology Today: An Introduction to Weather, Climate, and the Environment (Thomson/Brooks/Cole, Pacific Grove, CA, ed. 7th, 2003).

3. J. M. Wallace and P. V. Hobbs, Atmospheric Science: An Introductory Survey (Elsevier Academic Press, Amsterdam, ed. 2nd, 2006).

4. R. G. Prinn, *Annual Review of Environment and Resources* 28, 29-57 (2003).

5. J. H. Seinfeld and S. N. Pandis, Atmospheric Chemistry and Physics: From Air Pollution to Climate Change (Wiley, New York, 1998).

6. B. J. Finlayson-Pitts and J. N. Pitts, Chemistry of the Upper and Lower Atmosphere: Theory, Experiments and Applications (Academic Press, San Diego, 2000).

7. W. L. Chameides, F. Fehsenfeld, M. O. Rodgers, C. Cardelino, J. Martinez, D. Parrish, W. Lonneman, D. R. Lawson, R. A. Rasmussen, P. Zimmerman, J. Greenberg, P. Middleton, T. Wang, *Journal of Geophysical Research-Atmospheres* 97, 6037-6055 (1992).

8. A. Guenther, C. N. Hewitt, D. Erickson, R. Fall, C. Geron, T. Graedel, P. Harley, L. Klinger, M. Lerdau, W. A. Mckay, T. Pierce, B. Scholes, R. Steinbrecher, R. Tallamraju, J. Taylor, P. Zimmerman, *Journal of Geophysical Research-Atmospheres* 100, 8873-8892 (1995).

9. R. Prinn, D. Cunnold, P. Simmonds, F. Alyea, R. Boldi, A. Crawford, P. Fraser, D. Gutzler, D. Hartley, R. Rosen, R. Rasmussen, *Journal of Geophysical Research-Atmospheres* 97, 2445-2461 (1992).

10. U. Poschl, *Angewandte Chemie-International Edition* 44, 7520-7540 (2005).

11. W. C. Hinds, Aerosol Technology: Properties, Behavior, and Measurement of Airborne Particles (Wiley, New York, ed. 2nd, 1999).

12. C. Anastasio and S. T. Martin, in *Nanoparticles and the Environment*, J. F. Banfield and A. Navrotsky, Eds. (Mineralogical Society of America, Blacksburg, Virginia, 2001), vol. 44, chap. 8.

13. M. Dal Maso, M. Kulmala, I. Riipinen, R. Wagner, T. Hussein, P. P. Aalto, K. E. J. Lehtinen, *Boreal Environment Research* 10, 323-336 (2005).

14. M. Mazurek, M. C. Masonjones, H. D. Masonjones, L. G. Salmon, G. R. Cass, K. A. Hallock, M. Leach, *Journal of Geophysical Research-Atmospheres* 102, 3779-3793 (1997).

15. W. F. Rogge, L. M. Hildemann, M. A. Mazurek, G. R. Cass, B. R. T. Simoneit, *Environmental Science & Technology* 27, 2700-2711 (1993).

16. C. Osterroht, *Fresenius Journal of Analytical Chemistry* 345, 773-779 (1993).

17. H. Tervahattu, J. Juhanoja, K. Kupiainen, *Journal of Geophysical Research-Atmospheres* 107, doi:10.1029/2001JD001403 (2002).

18. W. F. Rogge, M. A. Mazurek, L. M. Hildemann, G. R. Cass, B. R. T. Simoneit, *Atmospheric Environment* 27, 1309-1330 (1993).

19. L. M. Hildemann, G. R. Markowski, G. R. Cass, *Environmental Science & Technology* 25, 744-759 (1991).

20. J. De Gouw and J. L. Jimenez, *Environmental Science & Technology* 43, 7614-7618 (2009).

21. J. E. Cooper and E. E. Bray, *Geochimica et Cosmochimica Acta* 27, 1113-1127 (1963).

22. W. F. Rogge, L. M. Hildemann, M. A. Mazurek, G. R. Cass, B. R. T. Simoneit, *Environmental Science & Technology* 25, 1112-1125 (1991).

23. D. Grosjean and J. H. Seinfeld, *Atmospheric Environment* 23, 1733-1747 (1989).

24. D. Grosjean, *Atmospheric Environment* 26, 953-963 (1992).

25. W. F. Rogge, L. M. Hildemann, M. A. Mazurek, G. R. Cass, B. R. T. Simoneit, *Journal of Geophysical Research-Atmospheres* 101, 19379-19394 (1996).

26. J. C. Marty, A. Saliot, P. Buatmenard, R. Chesselet, K. A. Hunter, *Journal of Geophysical Research-Oceans and Atmospheres* 84, 5707-5716 (1979).

27. R. M. Gershey, *Limnology and Oceanography* 28, 309-319 (1983).

28. P. S. Gill, T. E. Graedel, C. J. Weschler, *Reviews of Geophysics* 21, 903-920 (1983).

29. J. E. Penner, D. Hegg, R. Leaitch, *Environmental Science & Technology* 35, 332A-340A (2001).

30. IPCC, 2007: Summary for Policymakers. In: *Climate Change 2007: The Physical Science Basis. Contribution of Working Group I to the Fourth Assessment Report of the Intergovernmental Panel on Climate Change* [Solomon, S., Qin, D, Manning, M., Chen, Z., Marquis, M, Averyt, K. B., Tignor, M, and Miller, H. L. (eds.)]. Cambridge University Press, Cambridge, United Kingdom and New York, NY, USA.

31. R. J. Charlson, S. E. Schwartz, J. M. Hales, R. D. Cess, J. A. Coakley, J. E. Hansen, D. J. Hofmann, *Science* 255, 423-430 (1992).

32. S. Twomey, *Journal of the Atmospheric Sciences* 34, 1149-1152 (1977).

33. M. J. Molina, A. V. Ivanov, S. Trakhtenberg, L. T. Molina, *Geophysical Research Letters* 31, doi:10.1029/2004GL020910 (2004).

34. K. C. Kaku, D. A. Hegg, D. S. Covert, J. L. Santarpia, H. Jonsson, G. Buzorius, D. R. Collins, *Atmospheric Chemistry and Physics* 6, 4101-4115 (2006).

35. G. O. Rubel and J. W. Gentry, *Journal of Aerosol Science* 16, 571-574 (1985).

36. B. Daumer, R. Niessner, D. Klockow, *Journal of Aerosol Science* 23, 315-325 (1992).

37. M. L. Shulman, R. J. Charlson, E. J. Davis, *Journal of Aerosol Science* 28, 737-752 (1997).

38. K. M. Emmerson, N. Carslaw, D. C. Carslaw, J. D. Lee, G. McFiggans, W. J. Bloss, T. Gravestock, D. E. Heard, J. Hopkins, T. Ingham, M. J. Pilling, S. C. Smith, M. Jacob, P. S. Monks, *Atmospheric Chemistry and Physics* 7, 167-181 (2007).

39. Y. Sadanaga, A. Yoshino, S. Kato, A. Yoshioka, K. Watanabe, Y. Miyakawa, I. Hayashi, M. Ichikawa, J. Matsumoto, A. Nishiyama, N. Akiyama, Y. Kanaya, Y. Kajii, *Geophysical Research Letters* 31, doi:10.1029/2004GL019661 (2004).

40. S. Dusanter, D. Vimal, P. S. Stevens, R. Volkamer, L. T. Molina, A. Baker, S. Meinardi, D. Blake, P. Sheehy, A. Merten, R. Zhang, J. Zheng, E. C. Fortner, W. Junkermann, M. Dubey, T. Rahn, B. Eichinger, P. Lewandowski, J. Prueger, H. Holder, *Atmospheric Chemistry and Physics* 9, 6655-6675 (2009).

41. P. Di Carlo, W. H. Brune, M. Martinez, H. Harder, R. Lesher, X. R. Ren, T. Thornberry, M. A. Carroll, V. Young, P. B. Shepson, D. Riemer, E. Apel, C. Campbell, *Science* 304, 722-725 (2004).

42. J. Ortega, D. Helmig, A. Guenther, P. Harley, S. Pressley, C. Vogel, *Atmospheric Environment* 41, 5479-5495 (2007).

43. G. H. Mount and F. L. Eisele, *Science* 256, 1187-1190 (1992).

44. F. L. Eisele, G. H. Mount, F. C. Fehsenfeld, J. Harder, E. Marovich, D. D. Parrish, J. Roberts, M. Trainer, *Journal of Geophysical Research-Atmospheres* 99, 18605-18626 (1994).

45. F. L. Eisele, D. J. Tanner, C. A. Cantrell, J. G. Calvert, *Journal of Geophysical Research-Atmospheres* 101, 14665-14679 (1996).

46. W. J. Bloss, J. D. Lee, D. E. Heard, R. A. Salmon, S. J. B. Bauguitte, H. K. Roscoe, A. E. Jones, *Atmospheric Chemistry and Physics* 7, 4171-4185 (2007).

47. V. Sinha, J. Williams, J. N. Crowley, J. Lelieveld, *Atmospheric Chemistry and Physics* 8, 2213-2227 (2008).

48. X. R. Ren, W. H. Brune, C. A. Cantrell, G. D. Edwards, T. Shirley, A. R. Metcalf, R. L. Lesher, *Journal of Atmospheric Chemistry* 52, 231-257 (2005).

49. X. R. Ren, W. H. Brune, A. Oliger, A. R. Metcalf, J. B. Simpas, T. Shirley, J. J. Schwab, C. H. Bai, U. Roychowdhury, Y. Q. Li, C. X. Cai, K. L. Demerjian, Y. He, X. L. Zhou, H. L. Gao, J. Hou, *Journal of Geophysical Research-Atmospheres* 111, (2006).

50. R. Sommariva, W. J. Bloss, N. Brough, N. Carslaw, M. Flynn, A. L. Haggerstone, D. E. Heard, J. R. Hopkins, J. D. Lee, A. C. Lewis, G. McFiggans, P. S. Monks, S. A. Penkett, M. J. Pilling, J. M. C. Plane, K. A. Read, A. Saiz-Lopez, A. R. Rickard, P. I. Williams, *Atmospheric Chemistry and Physics* 6, 1135-1153 (2006).

51. R. G. Remorov and M. W. Bardwell, *Journal of Physical Chemistry B* 109, 20036-20043 (2005).

52. J. J. Schauer, W. F. Rogge, L. M. Hildemann, M. A. Mazurek, G. R. Cass, *Atmospheric Environment* 30, 3837-3855 (1996).

53. A. L. Robinson, N. M. Donahue, W. F. Rogge, *Journal of Geophysical Research-Atmospheres* 111, doi:10.1029/2005JD006265 (2006).

54. J. M. Samet, F. Dominici, F. C. Curriero, I. Coursac, S. L. Zeger, *New England Journal of Medicine* 343, 1742-1749 (2000).

55. V. Ramanathan, P. J. Crutzen, J. T. Kiehl, D. Rosenfeld, *Science* 294, 2119-2124 (2001).

56. A. Marenco, H. Gouget, P. Nedelec, J. P. Pages, F. Karcher, *Journal of Geophysical Research-Atmospheres* 99, 16617-16632 (1994).

57. S. Sandroni, D. Anfossi, S. Viarengo, *Journal of Geophysical Research-Atmospheres* 97, 2535-2539 (1992).

58. E. A. Holland, B. H. Braswell, J. F. Lamarque, A. Townsend, J. Sulzman, J. F. Muller, F. Dentener, G. Brasseur, H. Levy, J. E. Penner, G. J. Roelofs, *Journal of Geophysical Research-Atmospheres* 102, 15849-15866 (1997).

59. P. M. Vitousek, J. D. Aber, R. W. Howarth, G. E. Likens, P. A. Matson, D. W. Schindler, W. H. Schlesinger, D. G. Tilman, *Ecological Applications* 7, 737-750 (1997).

60. E. A. Holland, F. J. Dentener, B. H. Braswell, J. M. Sulzman, *Biogeochemistry* 46, 7-43 (1999).

61. M. O. Andreae, *Science* 315, 50-51 (2007).

62. S. Madronich and C. Granier, *Geophysical Research Letters* 19, 465-467 (1992).

63. A. K. Bertram, A. V. Ivanov, M. Hunter, L. T. Molina, M. J. Molina, *Journal of Physical Chemistry A* 105, 9415-9421 (2001).

64. P. A. J. Bagot, C. Waring, M. L. Costen, K. G. McKendrick, *Journal of Physical Chemistry C* 112, 10868-10877 (2008).

65. J. D. Hearn and G. D. Smith, *Geophysical Research Letters* 33, (2006).

66. I. J. George, A. Vlasenko, J. G. Slowik, K. Broekhuizen, J. P. D. Abbatt, *Journal of Atmospheric Chemistry* 7, 4187-4201 (2007).

67. A. T. Lambe, J. Zhang, A. M. Sage, N. M. Donahue, *Environmental Science & Technology* 41, 2357-2363 (2007).

68. V. F. McNeill, R. L. N. Yatavelli, J. A. Thornton, C. B. Stipe, O. Landgrebe, *Atmospheric Chemistry and Physics* 8, 5465-5476 (2008).

69. J. D. Smith, J. H. Kroll, C. D. Cappa, D. L. Che, C. L. Liu, M. Ahmed, S. R. Leone, D. R. Worsnop, K. R. Wilson, *Atmospheric Chemistry and Physics* 9, 3209-3222 (2009).

70. D. L. Che, J. D. Smith, S. R. Leone, M. Ahmed, K. R. Wilson, *Physical Chemistry Chemical Physics* 11, 7885-7895 (2009).

71. A. T. Lambe, M. A. Miracolo, C. J. Hennigan, A. L. Robinson, N. M. Donahue, *Environmental Science & Technology* 43, 8794-8800 (2009).

72. P. Davidovits, C. E. Kolb, L. R. Williams, J. T. Jayne, D. R. Worsnop, *Chemical Reviews* 106, 1323-1354 (2002).

73. S. E. Schwartz, in *Chemistry of Multiphase Atmospheric Systems*, W. Jaeschke, Ed. (Heidelberg, Springer, 1986), vol. G6.

74. D. R. Worsnop, J. W. Morris, Q. Shi, P. Davidovits, C. E. Kolb, *Geophysical Research Letters* 29, doi:10.1029/2002GL015542 (2002).

75. N. A. Fuchs and A. G. Sutugin, Highly Dispersed Aerosols (Ann Arbor Science Publishers, Ann Arbor, 1970).

76. D. J. E. Harvie and D. F. Fletcher, *Journal of Heat Transfer-Transactions of the Asme* 123, 486-491 (2001).

77. P. V. Danckwerts, Gas-liquid reactions (McGraw-Hill, New York, 1970), p. 276.

78. D. R. Hanson and E. R. Lovejoy, *Science* 267, 1326-1328 (1995).

79. D. R. Hanson and A. R. Ravishankara, *Journal of Physical Chemistry* 98, 5728-5735 (1994).

80. D. R. Hanson, *Journal of Physical Chemistry B* 101, 4998-5001 (1997).

81. G. M. Nathanson, P. Davidovits, D. R. Worsnop, C. E. Kolb, *Journal of Physical Chemistry* 100, 13007-13020 (1996).

82. R. G. Remorov and C. George, *Physical Chemistry Chemical Physics* 8, 4897-4901 (2006).

83. F. F. Fenter, F. Caloz, M. J. Rossi, *Journal of Physical Chemistry* 98, 9801-9810 (1994).

84. A. Takami, S. Kato, A. Shimono, S. Koda, *Chemical Physics* 231, 215-227 (1998).

85. H. A. Al Abadleh and V. H. Grassian, *Journal of Physical Chemistry A* 104, 11926-11933 (2000).

86. C. R. Usher, A. E. Michel, D. Stec, V. H. Grassian, *Atmospheric Environment* 37, 5337-5347 (2003).

87. T. L. Eliason, J. B. Gilman, V. Vaida, *Atmospheric Environment* 38, 1367-1378 (2004).

88. N. M. Donahue, A. L. Robinson, K. E. H. Hartz, A. M. Sage, E. A. Weitkamp, *Geophysical Research Letters* 32, (2005).

89. I. J. George, J. Slowik, J. P. D. Abbatt, *Geophysical Research Letters* 35, (2008).

90. D. M. Golden, G. N. Spokes, S. W. Benson, *Angewandte Chemie-International Edition in English* 12, 534-546 (1973).

91. F. Caloz, F. F. Fenter, K. D. Tabor, M. J. Rossi, *Review of Scientific Instruments* 68, 3172-3179 (1997).

92. A. L. Goodman, P. Li, C. R. Usher, V. H. Grassian, *Journal of Physical Chemistry A* 105, 6109-6120 (2001).

93. P. Li, K. A. Perreau, E. Covington, C. H. Song, G. R. Carmichael, V. H. Grassian, *Journal of Geophysical Research-Atmospheres* 106, 5517-5529 (2001).

94. V. H. Grassian, *Journal of Physical Chemistry A* 106, 860-877 (2002).

95. A. P. Prince, J. L. Wade, V. H. Grassian, P. D. Kleiber, M. A. Young, *Atmospheric Environment* 36, 5729-5740 (2002).

96. T. Anttila and V. M. Kerminen, *Journal of Geophysical Research-Atmospheres* 108, (2003).

97. S. K. Meilinger and Th. Peter, *Atmospheric Chemistry and Physics* 5, 533-545 (2005).

98. S. K. Meilinger, B. Karcher, Th. Peter, *Atmospheric Chemistry and Physics* 2, 307-312 (2002).

99. A. Bacak, M. W. Bardwell, M. T. Raventos-Duran, C. J. Percival, P. D. Hamer, D. E. Shallcross, *Chemical Physics Letters* 419, 125-129 (2006).

100. M. W. Bardwell, A. Bacak, M. T. Raventos, C. J. Percival, G. Sanchez-Reyna, D. E. Shallcross, *International Journal of Chemical Kinetics* 37, 253-260 (2005).

101. Y. Rudich, N. M. Donahue, T. F. Mentel, *Annual Review of Physical Chemistry* 58, 321-352 (2007).

102. E. A. Weitkamp, A. T. Lambe, N. M. Donahue, A. L. Robinson, *Environmental Science & Technology* 42, 7950-7956 (2008).

103. J. H. Kroll, J. D. Smith, D. L. Che, S. H. Kessler, D. R. Worsnop, K. R. Wilson, *Physical Chemistry Chemical Physics* 11, 8005-8014 (2009).

104. W. U. Palm, M. Elend, H. U. Krueger, C. Zetzsch, *Environmental Science & Technology* 31, 3389-3396 (1997).

105. A. M. Sage, E. A. Weitkamp, A. L. Robinson, N. M. Donahue, *Atmospheric Chemistry and Physics* 8, 1139-1152 (2008).

106. D. R. Hanson, J. B. Burkholder, C. J. Howard, A. R. Ravishankara, *Journal of Physical Chemistry* 96, 4979-4985 (1992).

107. P. L. Cooper and J. P. D. Abbatt, *Journal of Physical Chemistry* 100, 2249-2254 (1996).

108. R. L. Brown, *Journal of Research of the National Bureau of Standards* 83, 1-8 (1978).

109. A. Laskin, H. Wang, W. H. Robertson, J. P. Cowin, M. J. Ezell, B. J. Finlayson-Pitts, *Journal of Physical Chemistry A* 110, 10619-10627 (2006).

110. D. D. Jech, P. G. Easley, B. B. Krieger, Kinetics of reactions between free radicals and surfaces (aerosols) applicable to atmospheric chemistry (American Geophysical Union, Washington, DC, 1982).

111. A. Bacak, *PhD Thesis*, Nottingham Trent University (2004).

112. A. Bacak, M. W. Bardwell, M. T. Raventos, C. J. Percival, G. Sanchez-Reyna, D. E. Shallcross, *Journal of Physical Chemistry A* 108, 10681-10687 (2004).

113. M. W. Bardwell, A. Bacak, M. T. Raventos, C. J. Percival, G. Sanchez-Reyna, D. E. Shallcross, *Physical Chemistry Chemical Physics* 5, 2381-2385 (2003).

114. A. F. Khalizov, M. E. Earle, W. J. W. Johnson, G. D. Stubley, J. J. Sloan, *Journal of Aerosol Science* 37, 1174-1187 (2006).

115. A. F. Khalizov, M. E. Earle, W. J. W. Johnson, G. D. Stubley, J. J. Sloan, *Review of Scientific Instruments* 77, (2006).

116. Vapor Pressure of Water, *http://genchem1.chem.okstate.edu/1515SP10/Default.html*, 22-4-2010.

117. DeVilbiss Ultra-Neb Large Volume Ultrasonic Nebulizer *099HC, 099HD, 200HS and 200HI*: Instruction Manual, Sunrise Medical, 1991

118. Model 3076 Constant Output Atomizer: Instruction Manual, TSI Incorporated, 2005

119. Burgener, J., Personal Communication

120. C. F. Bohren and D. R. Huffman, Absorption and scattering of light by small particles (Wiley, New York, 1983).

121. S. M. McGinty, M. K. Kapala, R. F. Niedziela, *Physical Chemistry Chemical Physics* 11, 7998-8004 (2009).

122. A. Y. Zasetsky, J. J. Sloan, R. Escribano, D. Fernandez, *Geophysical Research Letters* 29, 2071-2074 (2002).

123. A. Y. Zasetsky, A. F. Khalizov, J. J. Sloan, *Applied Optics* 43, 5503-5511 (2004).

124. A. Y. Zasetsky, M. E. Earle, B. Cosic, R. Schiwon, I. A. Grishin, R. McPhail, R. G. Pancescua, J. Najera, A. F. Khalizov, K. B. Cook, J. J. Sloan, *Journal of Quantitative Spectroscopy & Radiative Transfer* 107, 294-305 (2007).

125. G. B. Ellison, A. F. Tuck, V. Vaida, *Journal of Geophysical Research-Atmospheres* 104, 11633-11641 (1999).

126. M. Dal Maso, A. Hyvarinen, M. Komppula, P. Tunved, V. M. Kerminen, H. Lihavainen, Y. Viisanen, H. C. Hansson, M. Kulmala, *Tellus Series B-Chemical and Physical Meteorology* 60, 495-508 (2008).

127. J. H. Vincent, Aerosol sampling science and practice (Wiley, Chichester, 1989).

128. L. G. Huey, D. R. Hanson, C. J. Howard, *Journal of Physical Chemistry* 99, 5001-5008 (1995).

129. A. A. Viggiano, A. I. Fernandez, J. Troe, *Physical Chemistry Chemical Physics* 7, 1533-1539 (2005).

130. C. E. Canosa-Mas and R. P. Wayne, *International Journal of Chemical Kinetics* 22, 829-841 (1990).

131. D. L. Baulch, I. M. Campbell, S. M. Saunders, *Journal of the Chemical Society-Faraday Transactions I* 81, 259-263 (1985).

132. NIST Chemistry WebBook: NIST Standard Reference Database Number 69, *http://webbook.nist.gov/chemistry/,* 1-2-2010.

133. S. Gross, R. Iannone, S. Xiao, A. K. Bertram, *Physical Chemistry Chemical Physics* 11, 7792-7803 (2009).

134. J. Vieceli, M. Roeselova, N. Potter, L. X. Dang, B. C. Garrett, D. J. Tobias, *Journal of Physical Chemistry B* 109, 15876-15892 (2005).

135. M. Roeselova, J. Vieceli, L. X. Dang, B. C. Garrett, D. J. Tobias, *Journal of the American Chemical Society* 126, 16308-16309 (2004).

136. M. G. J. Heijman, A. J. P. Heitzman, H. Nauta, Y. K. Levine, *Radiation Physics and Chemistry* 26, 83-88 (1985).

137. A. J. Elliot and D. R. Mccracken, *Radiation Physics and Chemistry* 33, 69-74 (1989).

138. C. Girardet and C. Toubin, *Surface Science Reports* 44, 163-238 (2001).

139. M. T. Lopez-Lopez, J. de Vicente, F. Gonzalez-Caballero, J. D. G. Duran, *Colloids and Surfaces A - Physicochemical and Engineering Aspects* 264, 75-81 (2005).

140. D. J. Donaldson, *Journal of Physical Chemistry A* 103, 62-70 (1999).

141. D. J. Donaldson and D. Anderson, *Journal of Physical Chemistry A* 103, 871-876 (1999).

142. R. Vacha, P. Slavicek, M. Mucha, B. J. Finlayson-Pitts, P. Jungwirth, *Journal of Physical Chemistry A* 108, 11573-11579 (2004).

143. J. H. Slade, *MSc Thesis*, Purdue University (2010).

144. I. Kourtchev, L. Copolovici, M. Claeys, W. Maenhaut, *Environmental Science & Technology* 43, 4665-4671 (2009).

145. O. R. Cooper, J. L. Moody, T. D. Thornberry, M. S. Town, M. A. Carroll, *Journal of Geophysical Research-Atmospheres* 106, 24289-24299 (2001).

146. D. L. Baulch, C. J. Cobos, R. A. Cox, C. Esser, P. Frank, Th. Just, J. A. Kerr, M. J. Pilling, J. Troe, R. W. Walker, J. Warnatz, *Journal of Physical and Chemical Reference Data* 21, 411-429 (1992).

147. Y. Rudich, *Chemical Reviews* 103, 5097-5124 (2003).

148. D. A. Knopf, J. Mak, S. Gross, A. K. Bertram, *Geophysical Research Letters* 33, doi:10.1029/2006GL026884 (2006).

149. T. Moise and Y. Rudich, *Journal of Physical Chemistry A* 106, 6469-6476 (2002).

150. J. W. Morris, P. Davidovits, J. T. Jayne, J. L. Jimenez, Q. Shi, C. E. Kolb, D. R. Worsnop, W. S. Barney, G. Cass, *Geophysical Research Letters* 29, doi:10.1029/2002GL014692 (2002).

151. G. D. Smith, E. Woods, C. L. DeForest, T. Baer, R. E. Miller, *Journal of Physical Chemistry A* 106, 8085-8095 (2002).

152. T. Thornberry and J. P. D. Abbatt, *Physical Chemistry Chemical Physics* 6, 84-93 (2004).

153. Y. J. Balkanski, D. J. Jacob, G. M. Gardner, W. C. Graustein, K. K. Turekian, *Journal of Geophysical Research-Atmospheres* 98, 20573-20586 (1993).

154. G. R. Jamieson and E. H. Reid, *Phytochemistry* 11, 269-& (1972).

155. J. D. Hearn and G. D. Smith, *Physical Chemistry Chemical Physics* 7, 2549-2551 (2005).

156. Y. Katrib, G. Biskos, P. R. Buseck, P. Davidovits, J. T. Jayne, M. Mochida, M. E. Wise, D. R. Worsnop, S. T. Martin, *Journal of Physical Chemistry A* 109, 10910-10919 (2005).

157. D. A. Knopf, L. M. Anthony, A. K. Bertram, *Journal of Physical Chemistry A* 109, 5579-5589 (2005).

158. D. R. Hanson, A. R. Ravishankara, S. Solomon, *Journal of Geophysical Research-Atmospheres* 99, 3615-3629 (1994).

159. S. F. Maria, L. M. Russell, M. K. Gilles, S. C. B. Myneni, *Science* 306, 1921-1924 (2004).

160. R. F. Niedziela, M. L. Norman, R. E. Miller, D. R. Worsnop, *Geophysical Research Letters* 25, 4477-4480 (1998).

161. R. F. Niedziela, R. E. Miller, D. R. Worsnop, *Journal of Physical Chemistry A* 102, 6477-6484 (1998).

162. R. F. Niedziela, M. L. Norman, C. L. DeForest, R. E. Miller, D. R. Worsnop, *Journal of Physical Chemistry A* 103, 8030-8040 (1999).

163. M. T. Dohm and R. F. Niedziela, *Geophysical Research Letters* 31, (2004).

164. M. T. Dohm, A. M. Potscavage, R. F. Niedziela, *Journal of Physical Chemistry A* 108, 5365-5376 (2004).

165. A. Y. Zasetsky, A. F. Khalizov, M. E. Earle, J. J. Sloan, *Journal of Physical Chemistry A* 109, 2760-2764 (2005).

166. M. E. Earle, R. G. Pancescu, B. Cosic, A. Y. Zasetsky, J. J. Sloan, *Journal of Physical Chemistry A* 110, 13022-13028 (2006).

167. Q. Zhang, J. L. Jimenez, M. R. Canagaratna, J. D. Allan, H. Coe, I. Ulbrich, M. R. Alfarra, A. Takami, A. M. Middlebrook, Y. L. Sun, K. Dzepina, E. Dunlea, K. Docherty, P. F. DeCarlo, D. Salcedo, T. Onasch, J. T. Jayne, T. Miyoshi, A. Shimono, S. Hatakeyama, N. Takegawa, Y. Kondo, J. Schneider, F. Drewnick, S. Borrmann, S. Weimer, K. Demerjian, P. Williams, K. Bower, R. Bahreini, L. Cottrell, R. J. Griffin, J. Rautiainen, J. Y. Sun, Y. M. Zhang, D. R. Worsnop, *Geophysical Research Letters* 34, (2007).

168. K. Kawamura and I. R. Kaplan, *Environmental Science & Technology* 21, 105-110 (1987).

169. I. Kourtchev, J. Warnke, W. Maenhaut, T. Hoffmann, M. Claeys, *Chemosphere* 73, 1308-1314 (2008).

170. S. S. Park, M. S. Bae, J. J. Schauer, Y. J. Kim, S. Y. Cho, S. J. Kim, *Atmospheric Environment* 40, 4182-4198 (2006).